ENERGY LEVEL ALIGNMENT IN METAL/OXIDE/SEMICONDUCTOR AND ORGANIC DYE/OXIDE SYSTEMS

BY ERIC BERSCH

A dissertation submitted to the

Graduate School—New Brunswick

Rutgers, The State University of New Jersey

in partial fulfillment of the requirements

for the degree of

Doctor of Philosophy

Graduate Program in Physics and Astronomy

Written under the direction of

Dr. Robert A. Bartynski

and approved by

_____

_____

_____

_____

_____

New Brunswick, New Jersey

October, 2008

ABSTRACT OF THE DISSERTATION

Energy Level Alignment in Metal/Oxide/Semiconductor and Organic Dye/Oxide Systems

by Eric Bersch

Dissertation Director: Dr. Robert A. Bartynski

The alignment between the energy levels of the constituent materials of metal-oxide-semiconductor field effect transistors (MOSFET's) and dye sensitized solar cell (DSSC's) is a key property that is critical to the functions of these devices. We have measured the energy level alignment (band offsets) for metal/oxide/semiconductor (MOS) systems with high-κ gate oxides and metal gates, and for organic dye/oxide systems. The combination of UV photoemission spectroscopy (UPS) and inverse photoemission spectroscopy (IPS) in the same vacuum system was used to measure both the occupied and unoccupied density of states (DOS), respectively, of these materials systems. Additional soft X-ray photoemission spectroscopy (SXPS) measurements were made of both the valence bands and core levels of the high-κ systems. The combination of the UPS, IPS and SXPS measurements were used to determine the band offsets between the high-κ oxides and the Si substrates of thin film oxide/Si samples.

To find the metal-oxide band offsets, thin metal layers were sequentially deposited on the oxide surfaces, followed by spectroscopic measurements. These measurements, combined with the measurements from the clean oxide surfaces, were used to find the metal-oxide band offsets. Metal-oxide band offset values were also calculated by the Interface Gap State (IGS) model. We compared the experimental metal-oxide

conduction band offset (CBO) values with those calculated using the IGS model, and found that they tended to agree well for Ru/oxide and Ti/oxide systems, but not as well for Al/oxide systems. Through core level spectroscopy, we correlated observations of the composition of the metallic layers with the trends in agreement between the experimental and IGS CBO values, which led to the conclusion that the IGS model gives accurate values for the CBO for systems with chemically abrupt interfaces. Core level spectroscopy of the MOS systems also showed that Al and Ti overlayers reduced the interfacial SiO_2 layers of $HfO_2/SiO_2/Si$ and $Hf_{0.7}Si_{0.3}O_2/SiO_2/Si$ systems, while leaving the composition of high-κ layers essentially unchanged.

We also measured the energy level alignment for 3 organic dye/oxide systems, N3 dye on rutile $TiO_2(110)$, N3 dye on anatase TiO_2 nanoparticle, and N3 dye on epitaxial $ZnO(11\bar{2}0)$ film substrates. For the $N3/TiO_2(110)$ system, we found the the N3 highest occupied molecular orbital (HOMO) was 0.9 eV above the TiO_2 valence band maximum (VBM) and the N3 lowest unoccupied molecular orbital (LUMO) was 0.5 eV above the TiO_2 conduction band minimum (CBM). The energy level alignment for the $N3/TiO_2$ nanoparticle system was similar to that for $N3/TiO_2(110)$. The alignment between the N3 HOMO and oxide VBM for the N3/ZnO systems was found to be similar to those of the $N3/TiO_2$ systems, whereas the alignment between the N3 LUMO and oxide CBM alignment was found to differ markedly between the N3/ZnO and the respective $N3/TiO_2$ systems. The difference in the LUMO-CBM alignments is attributed to the different interactions between the N3 LUMO and the ZnO and TiO_2 conduction bands. In addition, we measure the energy level alignment for a prototype dye molecule, isonicotinic acid (INA), on $TiO_2(110)$ and ZnO substrates. These measurements showed that the LUMO of INA is similar to that of N3, and that the HOMO of INA is much different than that of N3, in keeping with expectations based on the compositions and theoretical electronic structures of these molecules.

Acknowledgements

There are many people I would like to thank for helping me complete this degree. The first person I want to thank is my advisor, Bob Bartynski. Bob has been an excellent advisor to me over my graduate career, providing me with challenging projects and guiding me along the way as I worked on them. I am most grateful to Bob for his persistence and enthusiasm on a project that had a number of setbacks and delays. Without his strong leadership, this project would not have had the positive outcome that it did. I have also learned much from Bob on a personal level. He is generous and insightful, and I have developed greatly as a scientist and a person with him as my advisor.

I also want to thank my labmates, who made daily life in the lab a rich and rewarding experience. I am grateful to Anthony Danese, who helped to recruit me to the group, and who was always a willing mentor on matters of the lab or graduate student life. Thanks, also, to Safak Sayan for training me on how to operate the UHV chamber and perform the IPS measurements, as well as his career advice in later years. I was fortunate to join the group around the same time as James Lallo and Hua Yao, who became my good friends and confidantes for years to come. I want to thank Sylvie Rangan for being a scientific mentor for me, as well as a friend. Our discussions over the years have had an impact on my ways of thinking. Working with Levan Tskipuri has been a great pleasure. His unique way of going about his life and work were a source of endless surprises. I am very glad that Jean Patrick Theisen joined our group this past year. He contributed greatly to the project that we worked on together, and his friendship was an unexpected joy in this last year of my graduate career. I would also like to thank Lyudmila Goncharova for the MEIS measurements and hosting the marvelous Friday evening dinner parties, and Dave Hill for being such a great companion in the lab for a number of years.

Another highlight of graduate school for me has been the friends I made in my first two years at Rutgers. Thanks to Jackie and Howard Bondell, Karen and Jeff Spaleta, Jessica and Aaron Warren, Neelima Sehgal and Rouven Essig, Matthew and Meredith Francis, and Jeremy Pronchik for being my friends for all of these years. Your support has been very important to me. I would also like to acknowledge the other professors with whom I worked at Rutgers. Rick Garfunkel has been a great second advisor to me, always willing to give scientific advice and able to raise the spirits in the room. I have been honored to have some interaction with Torgny Gustafsson and Ted Madey, two first rate scientists and very admirable men. Elio Vescovo played a major role in the work presented in this thesis by allowing us to use beamline U5 at the NSLS and guiding our work there with his Italian wit and wisdom. I would also like to thank Bill, Eric, Ernie and Arvid. Their work in the machine shop was indispensable to the maintenance and improvement of the UHV system, and it was always enjoyable to pay them a visit.

My time at Rutgers would not have been nearly as rich had it not been for my family. Thanks to Uncle Jack, Aunt Pat, Aunt Barbara and Uncle Anthony for letting me stay at your houses during my first year at Rutgers. The time I spent with you and Ryan, Molly, Tommy, Anna and Jacob during that year was a very special to me. I also want to thank my brothers and sister-in-law for remaining close to me during this time, though they were cheering me on from Wisconsin. Lastly, I would like to thank my Dad for his love and support. The perpetual encouragements to "keep up the good work" had their effect, and I drew strength from them. I am grateful for the love of learning that you and Mom instilled in me at an early age, and I hope to continue to make good use of it in the future.

Dedication

To my Dad and Mom

Table of Contents

Abstract ii

Acknowledgements iv

Dedication vi

List of Tables x

List of Figures xi

1. Introduction 1

1.1. Miniaturization of MOSFETs 1

1.2. MOSFET Band Diagram 4

1.3. Candidate High-κ Materials 7

1.4. MOSFET Function 9

1.5. Flatband Voltage 11

1.6. Band Alignment Models 14

1.7. Alternative Gate Electrode Materials 17

1.8. Importance of Band Offsets 19

1.9. Measurement of Band Offsets 21

1.10. Energy Level Alignment in Dye Sensitized Solar Cells 23

1.11. Outline of Thesis 25

2. Experimental 27

2.1. Introduction 27

2.2. Ultra High Vacuum 27

2.3. Photoemission Spectroscopy 29

2.4. Inverse Photoemission Spectroscopy 37

2.5. Auger Electron Spectroscopy 42
2.6. Low Energy Electron Diffraction 45
2.7. X-ray Absorption Spectroscopy 47

3. Oxide-Semiconductor Band Offsets 49
3.1. Introduction 49
3.2. Growth of High-κ films on Si 50
3.3. Interfacial SiO_2 Oxide Layer 51
3.4. Comment on Sample Preparation 52
3.5. Experimental Methods 54
3.6. Preliminary Considerations 54
3.7. HfO_2-Si Band Offsets 57
3.8. Predicted HfO_2-Si Band Offsets 62
3.9. $Hf_{0.7}Si_{0.3}O_2$-Si Band Offsets 64
3.10. ZrO_2-Si Band Offsets 65
3.11. Al_2O_3-Si and SiO_2-Si Band Offsets 67
3.12. Importance of Sample Preparation; Specific Cases 70
3.13. Si Band Bending 72
3.14. Conclusions 74

4. Metal Oxide Band Offsets 76
4.1. Introduction 76
4.2. Experimental Methods 78
4.3. Metal-Oxide Band Offsets for $Ru/HfO_2/Si$ 79
4.4. Metal-Oxide Band Offsets for $Al/HfO_2/Si$ and $Ti/HfO_2/Si$ 83
4.5. Energy shifts for Ru/, Al/, and $Ti/Hf_{0.7}Si_{0.3}O_2/Si$ 85
4.6. Energy shifts for Ru/, Al/, and $Ti/SiO_2/Si$ 87
4.7. Energy Shifts for Ru/, Al/ and Ti/Al_2O_3 90
4.8. Theoretical Metal-Oxide Band Offsets 93
4.9. Discussion of Experimental and Theoretical CBO Values 98

4.10. Effect of Metal Overlayers on the Composition of Oxide and Interfacial SiO_2 layers . . . 102
4.11. Discussion of IL Reduction in $Al/HfO_2/Si$ and $Ti/HfO_2/Si$ . . . 109
4.12. Metal-Oxide Band Offset Results from the Literature . . . 110
4.13. Conclusions . . . 113

5. Energy Level Alignment of Organic Dye/Oxide Systems . . . 115
5.1. Introduction: Solar Cells . . . 115
5.2. Introduction: Dye Sensitized Solar Cells . . . 116
5.3. Properties of the TiO_2 Film and Dye Molecule . . . 118
5.4. Improvement of DSSCs: Dye-TiO_2 Interface . . . 120
5.5. Measurement of Energy Level Alignment . . . 123
5.6. Experimental Details . . . 128
5.7. STM Imaging of N3/TiO_2(110) Surface Preparation . . . 130
5.8. Energy Level Alignment: N3/rutile TiO_2(110) . . . 131
5.9. Energy Level Alignment: N3/TiO_2 nanoparticle film . . . 136
5.10. Energy Level Alignment: N3/$ZnO_2(11\bar{2}0)$ epitaxial film . . . 139
5.11. Energy Level Alignment: INA/TiO_2 and INA/$ZnO(11\bar{2}0)$ . . . 142
5.12. Conclusions . . . 145

6. Summary . . . 146

7. Appendix . . . 152
7.1. List of Acronyms . . . 152

Vita . . . 162

List of Tables

1.1. International Technology Roadmap for Semiconductors (ITRS) values (2006) showing the oxide thickness at which gate leakage current becomes unacceptable. [1] 3

1.2. Dielectric constants and band gaps for candidate high-κ dielectrics. . . . 8

3.1. Measured values for HfO_2 band gap and HfO_2-Si VBO and CBO. 63

3.2. Measured values for ZrO_2 band gap and ZrO_2-Si VBO and CBO. 66

3.3. Measured values for Al_2O_3 band gap and Al_2O_3-Si VBO and CBO. . . . 69

3.4. Measured values for SiO_2 band gap and SiO_2-Si VBO and CBO. 70

4.1. The experimental values for the metal-oxide VBO and CBO are determined by adding the VBM and CBM of the oxide before metallization and the energy shift (E_s) upon metallization (and taking the absolute value for the VBO). Metal-oxide band offsets values determined with the IGS model are also shown for comparison. 97

4.2. Experimental and theoretical values for the metal-oxide CBO. 111

7.1. List of acronyms used in this thesis. 152

List of Figures

1.1. Basic MOSFET structure 2

1.2. Band diagram of an MOS stack. 5

1.3. MOSFET band diagram for (a)accumulation (b)depletion (c)inversion (d)strong inversion. 10

1.4. Band diagrams of an n-MOS stack (a)before and (b)after contact. . . . 12

1.5. Band diagrams of an MOS stack with (a)positive (b)negative charged defect states in the oxide layer. 13

1.6. The interface dipole shifts the CBO from the Schottky limit value toward the Bardeen limit value. 17

1.7. Schematic diagram of (a) Fowler Nordheim (b) direct (c) Poole Frenkel (d) Schottky emission tunneling mechanisms. 21

1.8. Schematic diagram of a dye sensitized solar cell. 24

1.9. Band diagram of a dye sensitized solar cell. 25

2.1. Schematic diagram of the photoemission process. 29

2.2. Schematic diagram of a CMA. 32

2.3. (a)Schematic diagram of a channeltron electron multiplier and the current to voltage conversion circuit. 33

2.4. Photoemission spectra from a (a)Ta and a (b)HfO_2/Si sample, displayed as Intensity vs. Kinetic Energy. The vertical line in (a)indicates the kinetic energy of electrons originating from the Fermi level. 35

2.5. Schematic diagram of the spectrum width measurement. 36

2.6. Schematic diagram of the inverse photoemission process. 37

2.7. Schematic diagram of the properties of a spherical mirror with vertical grooves. 39

2.8. Schematic diagram of grating spectrometer IPS system and UPS system. 40
2.9. 2D position sensitive photon detector. 41
2.10. Energy diagram for the the electron gun and the sample in inverse photoemission. 42
2.11. Schematic energy diagram of the Auger process. 43
2.12. AES spectrum of Si and Ru(15 Å)/Si. 45
2.13. LEED apparatus schematic 46
2.14. Schematic diagram of the x-ray absorption spectroscopy process. 47
3.1. Band diagram of a HfO_2/SiO_2/p-Si stack. 53
3.2. (a)AES spectrum of annealed HfO_2/Si. (b)SXPS spectra of as loaded and annealed HfO_2/Si. 55
3.3. UPS and IPS from HfO_2/Si, where the red spectra were taken on a spot that was exposed to the electron beam before annealing and the black spectra were taken on a spot that was annealed before being exposed to the electron beam. 56
3.4. UPS, SXPS and IPS spectra from HfO_2/Si, where E=0 is the midgap of the Si at the interface. The inset shows SXPS spectrum where the intensity scale is increased by a factor of 8, and E=0 corresponds to the Fermi level. 58
3.5. Electron Inelastic Mean Free Path (IMFP) vs. kinetic energy.[2] 59
3.6. SXPS spectra of the (a)valence band (b)Si $2p$ core level regions from SiO_2/Si. 60
3.7. Band diagram of HfO_2(15 Å)/Si showing how the Si VBM and CBM differ in the bulk and at the interface. 62
3.8. UPS, SXPS and IPS spectra from $Hf_{0.7}Si_{0.3}O_2$/Si. 64
3.9. UPS, SXPS and IPS spectra from ZrO_2/Si. 67
3.10. UPS, SXPS and IPS spectra from Al_2O_3/Si. 68
3.11. UPS, SXPS and IPS spectra of SiO_2/Si. 70

4.1. Band diagrams for an (a)n-MOS stack with a low work function metal and (b)p-MOS stack with a high work function metal. 77
4.2. (a)UPS and (b)IPS measurements of HfO_2/Si metallized with Ru. . . . 80
4.3. SXPS (a)valence band and (b)Hf $4f$ core level spectra from HfO_2/Si metallized with Ru. 82
4.4. (a) Band diagram of an oxide on a thin film oxide/Si sample, where the Fermi level is extrapolated into the oxide from the Si. (b) Adding the shift in oxide states upon metallization to the oxide VBM and CBM gives the metal-oxide VBO and CBO. 83
4.5. SXPS (a)valence band and (b)Hf $4f$ core level spectra from HfO_2/Si metallized with Al. 84
4.6. (a)UPS and (b) IPS measurements from HfO_2/Si metallized with Ti. . . 85
4.7. (a)UPS and (b)IPS measurements from $Hf_{0.7}Si_{0.3}O_2$/Si metallized with Ru. 86
4.8. (a)UPS and (b)IPS measurements from $Hf_{0.7}Si_{0.3}O_2$/Si metallized with Al. 86
4.9. SXPS measurements of the (a)valence band and (b)Hf $4f$ core levels from $Hf_{0.7}Si_{0.3}O_2$/Si metallized with Al. 87
4.10. SXPS measurements of the (a)valence band and (b)Hf $4f$ core level from $Hf_{0.7}Si_{0.3}O_2$/Si metallized with Ti. 87
4.11. (a)UPS and (b)IPS and measurements from SiO_2/Si metallized with Ru. 88
4.12. SXPS measurements of the (a)valence band and (b)Si $2p$ core level from SiO_2/Si metallized with Ru. 89
4.13. (a)UPS and (b)IPS $2p$ measurements from SiO_2/Si metallized with Al. . 89
4.14. SXPS measurements of the (a)valence band and (b)Si $2p$ core level from SiO_2/Si metallized with Al. 90
4.15. (a)UPS and (b)IPS measurements from SiO_2/Si metallized with Ti. . . 91
4.16. (a)UPS and (b)IPS measurements from Al_2O_3/Si metallized with Ru. . 92

4.17. SXPS measurements of the (a)valence band and (b)Al $2p$ core level from Al_2O_3/Si metallized with Ru. 93
4.18. (a)UPS and (b)IPS measurements from Al_2O_3/Si metallized with Al. . . 94
4.19. SXPS measurements of the (a)valence band and (c)Al $2p$ core level from Al_2O_3/Si metallized with Al. 94
4.20. (a)UPS and (b)IPS measurements from Al_2O_3/Si metallized with Ti. . . 95
4.21. Band diagram showing the quantities involved in the IGS model calculation of the metal-oxid CBO. 96
4.22. Spectrum width measurement of (a)Ru and (b)HfO_2. 97
4.23. SXPS measurement of Ru 4p level from (a)HfO_2/Si, (b)SiO_2/Si and (c)Al_2O_3/Si metallized with Ru. 99
4.24. SXPS measurement of the Al $2p$ core level from sequentially metallized (a)HfO_2/Si, (b)$Hf_{0.7}SiO_2$/Si and (c)/SiO_2/Si metallized with Al. 100
4.25. SXPS measurement of Al $2p$ level from Al/Al_2O_3/Si showing that beam exposure contributes to the oxidation of the Al overlayer, and that a new spot has the original ratio of metallic and oxidized Al. 101
4.26. SXPS measurement of Ti $3p$ level from (a)HfO_2/Si and (b)$Hf_{0.7}Si_{0.3}O_2$/Si metallized with Ti. 102
4.27. SXPS measurement of the (a)Hf $4f$ and (b)Si $2p$ levels from HfO_2/Si metallized with Ru, the (c)Si $2p$ level from SiO_2/Si metallized with Ru, and the (d)Al $2p$ level from Al_2O_3/Si metallized with Ru. 104
4.28. AES spectrum from Si and Al/Si. 105
4.29. SXPS measurement of the (a)Hf $4f$ and (b)Si $2p$ core levels from HfO_2/Si metallized with Al. SXPS measurement of the (c)Hf $4f$ and (d)Si $2p$ core levels from $Hf_{0.7}Si_{0.3}O_2$/Si metallized with Al. 106
4.30. SXPS measurement of (a)Hf $4f$ and (b)Si $2p$ core levels from HfO_2/Si metallized with Ti. SXPS measurement of (a)Hf $4f$ and (b)Si $2p$ core levels from $Hf_{0.7}Si_{0.3}O_2$/Si metallized with Ti. 108
5.1. Band diagram of Si pn junction solar cell. 115

5.2. Schematic diagram of a dye sensitized solar cell. 117
5.3. Band diagram of a dye sensitized solar cell. 118
5.4. (a)Model of the N3 molecule. (b)Bidentate bridging (c)bidentate chelating and (d) monodentate bonding of N3 ligand to TiO_2. 120
5.5. (a)Model and 20×20 nm STM image of TiO_2(110) surface. (c) Ball and stick model of pivalic acid mocule. (d)Model and (e)STM image of pivalate/TiO_2(110). (after Sasahara *et al.*[3]) 122
5.6. Calculated spatial distribution of the N3 (a)HOMO and (b)LUMO bonded to anatase TiO_2(101).[4] 123
5.7. (a)UPS spectrum of N3/TiO_2. (b)IPCE vs. photon energy for a DSSC with N3 and black dye. (c)Energy diagram showing minimum photon energy needed to induce current. [5] 126
5.8. (a)XPS and XAS measurements of INA/TiO_2(110). [6] 127
5.9. Scanning tunneling microscope images of (a)clean and (b)pivalate covered and (c)dye covered rutile TiO_2(110). 131
5.10. UPS and IPS spectra of the clean and N3 covered TiO_2(110) surfaces. . 132
5.11. UPS and IPS of clean and dye/TiO_2 surfaces, where the clean surface spectra have been shifted and scaled. The two difference spectra were obtained using different estimates to the contribution from the substrate. 134
5.12. Energy level alignment between the (a)peaks and (b)edges of the HOMO and LUMO and the rutile TiO_2(110) VBM and CBM. Energies are given in eV. 135
5.13. Comparison of UPS and IPS of clean TiO_2(110) and TiO_2(110) exposed to pivalic acid, acetonitrile, and atmosphere. 136
5.14. UPS and IPS of clean and N3/anatase TiO_2 nanoparticle surfaces, where the clean surface spectra have been shifted and scaled. 137
5.15. Energy level alignment between the (a)peaks and (b)edges of the HOMO and LUMO and the anatanse TiO_2 nanoparticle VBM and CBM. Energies are given in eV. 138

5.16. UPS and IPS of clean and dye/ZnO($11\bar{2}0$) surface. 140
5.17. Energy level alignment between the (a)center and (b)edges of the HOMO and LUMO and the ZnO VBM and CBM. Energies are given in eV. . . 142
5.18. (a)UPS and IPS of clean and INA/rutile TiO_2(110) surfaces. (b)IPS difference spectra of N3/TiO_2(110) and INA/TiO_2(110). 143
5.19. (a)UPS and IPS of clean ZnO, atmosphere exposed ZnO, and INA/ZnO surfaces. (b)IPS difference spectrum for N3/ZnO and INA/ZnO. 144
5.20. UPS and IPS from clean, atmosphere exposed, acetonitrile exposed and INA/ZnO surfaces. 144

Chapter 1

Introduction

1.1 Miniaturization of MOSFETs

Semiconductor devices such as the MOSFET (metal-oxide-semiconductor field effect transistor) have been made progressively smaller over the past 45 years with the aim of placing more of them on an integrated circuit chip. The MOSFET is the primary component in integrated circuits used for computer processors and semiconductor memory, and its continued improvement is largely responsible for the great success of the personal computer and other microelectronics-based industries. Moore's law is the observation that the number of transistors on a chip has doubled approximately every 24 months, and the prediction that this rate of miniaturization will continue.[7] The semiconductor industry has been successful in fulfilling Moore's Law to the present time, but that success will be challenged in the next few years.

The heart of a MOSFET is essentially a parallel plate capacitor. Fig. 1.1 shows a basic MOSFET structure with a metal layer, an oxide layer, and a doped semiconductor substrate. The metal and oxide layers are also known as the gate electrode and the gate dielectric, respectively. Current MOSFET's use highly doped polycrystalline Si (poly-Si) as the gate electrode, SiO_2 as the gate dielectric, and more lightly doped single crystal Si as the semiconductor substrate. The source and the drain electrodes are highly doped Si regions embedded in the Si substrate. The bottom of the substrate can also used as an electrode in this device, but in this thesis it is considered to be grounded. Throughout this work, the MOS tri-layer structure will be referred to as the stack.

In its most common applications, a MOSFET functions as a switching device. This is made possible by the fact that the density of charge carriers in the semiconductor near

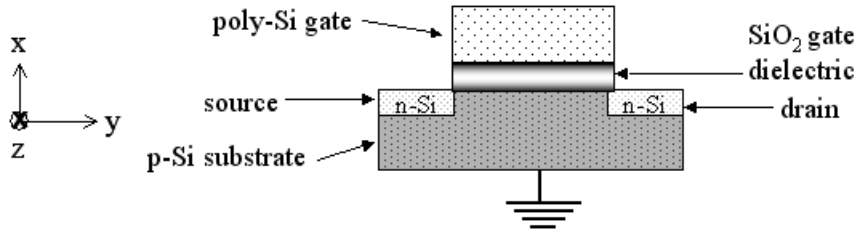

Figure 1.1: Basic MOSFET structure

the semiconductor-oxide interface can be controlled by a voltage applied to the gate. Applying an appropriate gate voltage will induce a high density of minority carriers (electrons in p-Si, holes in n-Si) between the source and drain electrodes, which results in a current between these two electrodes driven by a potential difference between them. While the current flows, the MOSFET is in the *on* state. By changing the gate voltage, the carrier density in the semiconductor can be reduced exponentially, and the device can be turned *off*.

A major part of improving the function of a MOSFET is increasing the capacitance per unit area of the device. In this way, more charge per unit area can be induced on both sides of the oxide for a given gate voltage, which produces a higher current between the source and the drain electrodes when the device is *on*. The capacitance per unit area across the oxide of a parallel plate structure (C_{ox}) (referred to from here on as capacitance unless otherwise noted) is given by equation 1.1, where t_{ox} is thickness of the oxide and ε_{ox} is the static permittivity of the oxide. This equation can also be written in terms of the the permittivity of free space (ε_o) and the relative permittivity of the oxide (κ_{ox}), the latter of which is commonly referred to as the dielectric constant. To increase the capacitance across the oxide of an MOS stack one can either reduce the oxide thickness or use a material with a higher dielectric constant. Throughout the history of the MOSFET, this has been done by making the oxide layer thinner.

$$C_{ox} = \frac{\varepsilon_{ox}}{t_{ox}} = \frac{\kappa_{ox}\varepsilon_o}{t_{ox}} \tag{1.1}$$

MOSFET's in production today have oxide layers as thin as 10 Å. [1] As the Si-O bond length is 1.6 Å, and the average O-O separation in SiO_2 is 2.4 Å, this layer only 3-7

atoms thick.[8] At this thickness, applying the threshold voltage (the voltage needed to turn the device on) across the stack results in significant, but not prohibitive, electron tunneling through the oxide. The current associated with this tunneling is called gate leakage current (I_{GL}), which results in high power loss in a device. Table 1.1 shows the Semiconductor Industry Association projected values of oxide thickness, leakage current and maximum allowed leakage current ($I_{GL,max}$) for the next 3 years, published in the International Technology Roadmap for Semiconductors.[1] For the period of 2008-2009, the oxide layer can be made thinner while the leakage current stays below the maximum allowed value. The target oxide thickness for 2010, however, will permit leakage current far above the maximum allowed value. Thus, as of 2009, the SiO_2 dielectric cannot be made thinner, and a high-κ material must be used as the gate dielectric to continue to increase the capacitance of the MOSFET.

year	oxide thickness(Å)	I_{GL}(nA/cm^2)	$I_{GL,max}$(nA/cm^2)
2008	10	300	1180
2009	9	1000	1100
2010	6.5	30000	1560

Table 1.1: International Technology Roadmap for Semiconductors (ITRS) values (2006) showing the oxide thickness at which gate leakage current becomes unacceptable. [1]

The use of a high-κ gate dielectric can, in principle, address two of the semiconductor industry's key issues. It can increase the capacitance due to the high-κ value, and decrease gate leakage current by being thicker than an SiO_2 gate dielectric. The capacitance of a high-κ layer can be compared to that of an SiO_2 layer via a parameter known as the effective oxide thickness (*eot*). The *eot* of a high-κ layer, given by equation 1.2, is the thickness that an SiO_2 layer would have to have order to yield the same capacitance. High-κ dielectrics have shown reduced gate leakage currents compared to an SiO_2 layer with the same *eot*.[8] However, there are other issues that challenge the widespread use of high-κ materials. These issues will be discussed throughout this chapter.

$$eot = (\frac{\kappa_{SiO_2}}{\kappa_{high-\kappa}})t_{high-\kappa} \tag{1.2}$$

1.2 MOSFET Band Diagram

The electronic structure of the materials in an MOS stack in the region ∼10 eV above and below the Fermi level is critical to their function in a MOSFET. The states in this region below the Fermi level make up the valence band, and those above the Fermi level make up the conduction band. In a metal, an infinitesimal energy is sufficient to excite an electron into an unoccupied state, but in a semiconductor and an insulator, there is an energy gap between the valence and conduction bands where no electronic states exist. The band diagram of the MOS stack is a summary of the electronic structure of each material in the stack, and how it aligns with the electronic structure of the other layers. In a band diagram, the highest occupied state of the valence band is referred to as the valence band maximum (VBM), and is represented by a line. The lowest unoccupied state of the conduction band, which is also represented by a line, is the conduction band minimum (CBM).

Fig. 1.2 shows the band diagram for an MOS stack where the highly doped Si gate electrode has been replaced with an actual metal electrode. In this band diagram, the VBM and CBM of the oxide ($E_{v,ox}$, $E_{c,ox}$) and those of the semiconductor ($E_{v,ox}$, $E_{c,ox}$) are labeled. If an electron at the bottom of the conduction band of the semiconductor were to move toward the oxide, it would, with a probability of 1 minus the tunneling probability, be reflected. This is because there are no electronic states in the oxide at this energy for it to occupy. Thus, the part of the oxide band gap above the Si CBM, which is equal to the difference between the oxide CBM and the semiconductor CBM, is the energy barrier to electrons in the semiconductor. This quantity is called the oxide-semiconductor conduction band offset (CBO), and is labeled $\Delta E_{c,os}$ in Fig. 1.2. Similarly, the difference between the oxide VBM and the Si VBM is the oxide-semiconductor valence band offset (VBO), which is labeled $\Delta E_{v,os}$ in Fig. 1.2. It is the barrier that blocks the movement of holes from the semiconductor to the metal.

In the same way, the movement of electrons from the metal to the semiconductor is blocked by the metal-oxide CBO ($\Delta E_{c,mo}$), which is the difference between the oxide CBM and the metal Fermi level ($E_{f,m}$). Finally, the metal-oxide VBO ($\Delta E_{c,mo}$), which

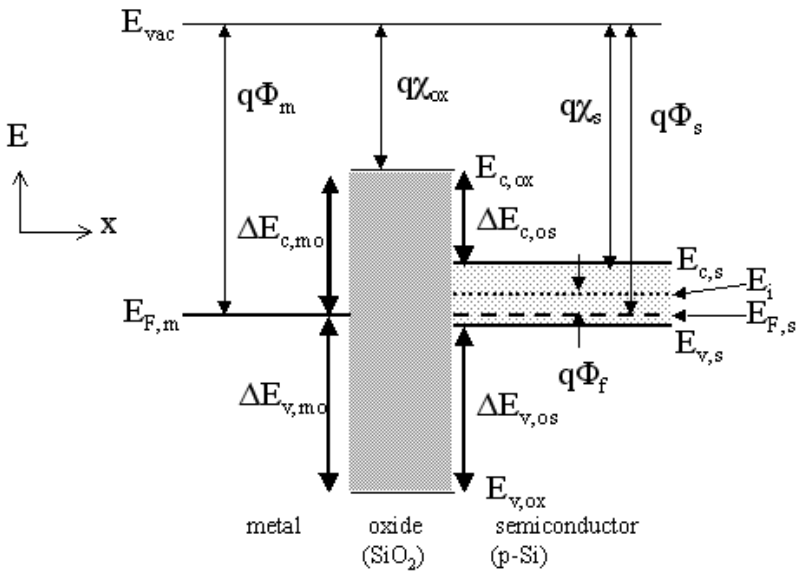

Figure 1.2: Band diagram of an MOS stack.

is the difference between the oxide VBM and the metal Fermi level, blocks the flow of holes in the metal to the semiconductor. As alluded to in the previous section, however, the probability for a charge carrier to tunnel through an energy barrier becomes non-trivial as the barrier is made very thin. The two factors on which the gate leakage current depends most strongly are the height of the energy barrier and the thickness of the barrier. The mechanisms of gate leakage current will be discussed later in this chapter.

Another key energy difference shown in Fig. 1.2 is the work function. One of the energy levels associated with the work function is the vacuum level (E_{vac}), which is the potential energy of an with electron in the vacuum, far from the material, where the potential is conventionally set to zero. The work function is the energy required to move an electron in a metal at the Fermi level into the zero potential region of the vacuum. Thus, the metal work function ($q\Phi_m$) is the energy difference between the vacuum level and the metal Fermi level ($E_{f,m}$). The semiconductor work function ($q\Phi_s$) is the energy difference between the vacuum level and the semiconductor Fermi level. The work function of a semiconductor is not as clearly defined as that of a metal because, in the absence of defect states, there are no states at the semiconductor Fermi level ($E_{f,s}$), which is in the band gap. The semiconductor Fermi level is an important

parameter, however, and will be discussed more below. The Fermi level of a wide band gap oxide (∼5-9 eV) is not a well-defined parameter. Thus, the work function of an oxide is also not well-defined.

Due to the relatively small band gap of a semiconductor (e.g., $E_{g,Si}$=1.1 eV), electrons can be thermally excited from the valence band to the conduction band at room temperature, creating an equal number of holes in the valence band in an un-doped semiconductor. The Fermi level of a semiconductor is determined based on the relative concentration of electrons in the conduction band (n) and holes in the valence band (p). For an un-doped semiconductor, the Fermi level is midway between the VBM and CBM. This is known as the intrinsic Fermi level (E_i) or the mid-gap level. The Fermi level can be altered by introducing dopants into semiconductor lattice sites. Introducing n-type dopants (donors) makes n larger than p and shifts the Fermi level toward the CBM. Conversely, introducing p-type dopants (acceptors) makes p larger than n and shifts the Fermi level toward the VBM. Equations 1.3 and 1.4 give the energy of the semiconductor Fermi level with respect to the intrinsic level for an n-doped and p-doped semiconductor, respectively, where N_d is the density of donors, N_a is the density of acceptors, n_i is the intrinsic concentration of electron-hole pairs, k is the Boltzmann constant and T is the temperature in Kelvin. These equations assume the full ionization of dopants. A quantity, denoted as $q\Phi_f$, is often used to represent the difference between the semiconductor Fermi level and the intrinsic Fermi level, as shown in Fig. 1.2. It is defined as $q\Phi_f$=$E_{f,s}$-E_i, where q=-e, and e is the fundamental unit of charge.

$$E_{f,s} - E_i = kT \ln(\frac{N_d}{n_i}) \tag{1.3}$$

$$E_i - E_{f,s} = kT \ln(\frac{N_a}{n_i}) \tag{1.4}$$

A final energy difference shown in Fig. 1.2 that must be noted is the electron affinity, which is the difference between the vacuum level and the CBM in a material with a band gap. The electron affinities for the both the oxide ($q\chi_{ox}$) and the semiconductor ($q\chi_s$)are displayed in Fig. 1.2.

In order to evaluate a material for use in MOSFET's, the band diagram of the MOS stack using this material must be well characterized. Our spectroscopic measurement techniques are well suited for this task. First, we measure the valence band and conduction band densities of states (DOS) of a thin high-κ oxide film on Si to find the VBM and CBM of the oxide. Due to the small thickness (15-25 Å) of the oxide films, we can also measure the valence band from the substrate Si, which allows us to determine the oxide-semiconductor VBO and CBO. Then we deposit a metal layers on top of the oxide layers in small increments, and measure the shift in the oxide states upon metallization. From these measurements, we can determine the metal-oxide VBO and CBO, as well.

1.3 Candidate High-κ Materials

High-κ materials have been under investigation since the late 1990's to identify those best suited to replace SiO_2 as the gate dielectric in MOSFETs. The primary criteria on which high-κ materials are evaluated are dielectric constant, thermal and chemical stability in contact with Si, and band offsets with Si. Clearly, the dielectric constant should be high as possible, but often a material with a high dielectric constant has a smaller band gap and, consequently, smaller band offsets. Table 1.2 shows the dielectric constant and band gap of a number of high-κ oxide candidate materials. $SrTiO_3$, TiO_2 and Ta_2O_3 are three of materials with the highest κ values, but also with the lowest band gaps. Each of these materials has been shown to have a small CBO with Si, and is not considered a strong candidate to replace SiO_2.[9, 10, 11] Thermal stability in contact with Si is a critical parameter because the preparation of a MOS device requires the annealing of the oxide/Si system to a high temperature (T>1000°C). This high temperature anneal has been shown to result in the intermixing of metal and Si in ZrO_2/Si and Al_2O_3/Si systems, which would severely compromise the function of the device.[12, 13]

One material that has withstood the high temperature anneal without intermixing with Si is HfO_2.[26] It also has a high dielectric constant and a relatively large band gap,

material	dielectric constant(Å)[14]	band gap (eV)
TiO_2	50-80	3.0[15]
Ta_2O_5	25-26	4.4[16]
Al_2O_3	9-11	6.7[17]
$SrTiO_3$	200	3.3[9]
ZrO_2	14-25	5.4[18]
$Zr_{0.5}Si_{0.5}O_2$	11	6.7[19]
HfO_2	15-26	5.7[20]
$Hf_{0.5}Si_{0.5}O_2$	12	6.2[21]
$Hf_{0.5}Al_{0.5}O_2$	12	5.9[22]
La_2O_3	21-30	5.5[23]
$LaAlO_3$	24	5.9[24]
Y_2O_3	12-18	6.0[25]

Table 1.2: Dielectric constants and band gaps for candidate high-κ dielectrics.

making it a strong candidate material. One issue associated with HfO_2 is that it undergoes a phase transition from amorphous to crystalline when annealed to 300-500°C, though the degree of crystallization is less for thinner films.[27] At these temperatures, HfO_2 films crystallize in the monoclinic phase, which has phonon modes that scatter charge carriers in the Si. The crystallization of HfO_2 has also been shown to result in the formation of charged defect states in the oxide that shift the threshold voltage.[8] In an effort to increase the crystallization temperature of HfO_2 while preserving its high dielectric constant, hafnium silicate films on Si have been investigated. $Hf_{0.7}Si_{0.3}O_2$ films have been shown to undergo a 1000°C anneal for 5 s and remain amorphous.[27]

Due to their promising characteristics, we have investigated HfO_2 and $Hf_{0.7}Si_{0.3}O_2$ films on Si. These materials both have band gaps which are approximately 3 eV smaller than that of SiO_2, so it is important to measure their band offsets with Si to determine if they are large enough for these oxides to be used in devices. The ITRS states that the band offsets between a high-κ oxide and Si must be at least 1.0 eV to inhibit gate leakage current.[28] We have also investigated ZrO_2, Al_2O_3 and SiO_2 films on Si. Studying a variety of oxide/Si systems has enabled us to collect a larger set of results to compare with results from the literature, thereby helping us evaluate our measurement technique in light of other techniques.

1.4 MOSFET Function

As discussed earlier, the density of charge carriers in the semiconductor at interface between the semiconductor and the oxide (this region will be referred to as the surface) can be manipulated by applying a potential difference across the MOS stack. Fig. 1.3 shows the band diagrams of an MOS stack where a different voltage is applied across the stack in each case. These band diagrams are useful for explaining the MOS stack properties and the function of the MOSFET in more detail. For the following discussion, consider a MOS stack with a p-Si substrate where the Si bands are flat in the absence of an applied voltage, as shown in Fig. 1.2. For this flat band condition to apply, the metal and semiconductor work functions must be equal, and the oxide must be free of a net charge due to defect states. Recall that the bulk of the Si substrate is considered to be grounded.

Applying a negative voltage to the gate electrode will draw positively charged holes, the majority carriers in p-Si, to the surface. The extra negative charge in the gate due to the externally applied voltage gives rise to an electric field which penetrates the oxide and the surface region of the semiconductor, but is screened from the bulk of the semiconductor by the positive charge at the semiconductor surface. The condition where majority carriers are drawn to the surface is called accumulation. The band diagram for accumulation is shown in Fig. 1.3(a), where the bands in the Si are bent upward, indicating increased hole density at the surface. The amount of band bending is the energy difference between the intrinsic Fermi level at the surface ($x = 0$) and in the bulk. It is expressed in a quantity called the surface potential (Φ_s), which is given by equation 1.5. The total potential difference across the stack is due to the gate voltage (V_g), which is equal to the potential drop across the oxide (Φ_{ox}) plus that across the semiconductor, as given in equation 1.6.

$$q\Phi_s = E_i(0) - E_i \tag{1.5}$$

$$V_g = \Phi_{ox} + \Phi_s \tag{1.6}$$

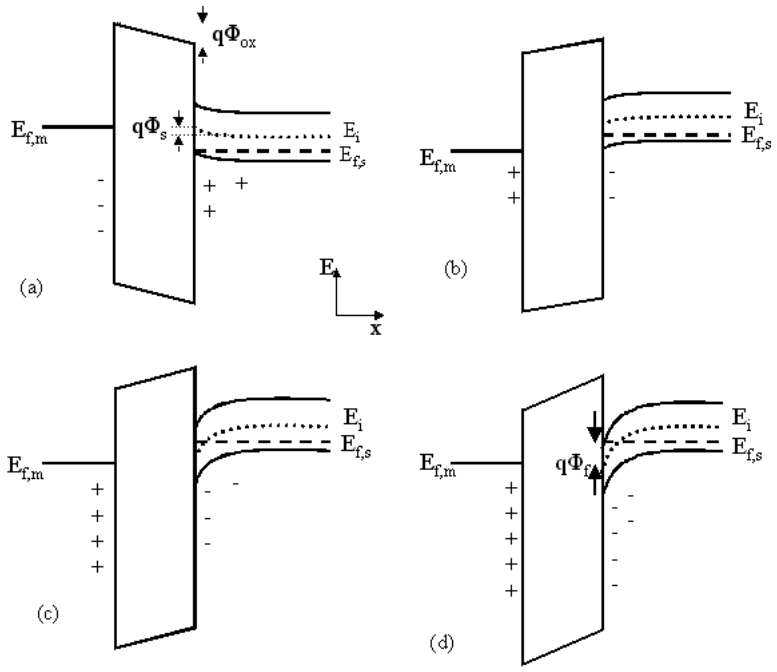

Figure 1.3: MOSFET band diagram for (a)accumulation (b)depletion (c)inversion (d)strong inversion.

Applying a positive gate voltage such that $0 < \Phi_s < \Phi_f$ will put the stack in a condition called depletion. In this condition, holes are pushed away from the surface, leaving behind negatively charged dopant ions. This region is called the depletion region because it is largely depleted of charge carriers. The negatively charged dopants in the depletion region screen the bulk of the semiconductor from the electric field due to the gate voltage. Thermally generated electrons-hole pairs in the depletion region tend to be separated by the electric field, with holes being driven into the Si bulk and the electrons pulled toward the surface. The downward bending of the Si bands, shown in Fig. 1.3(b), reflects an increased electron (minority carrier) density at the surface.

The two remaining conditions are obtained by increasing the positive voltage on the gate. The condition of inversion occurs when $\Phi_f < \Phi_s < 2\Phi_f$. In inversion, more holes are pushed into the bulk of the semiconductor than in depletion, widening the depletion region. More electrons are also drawn to the surface, to the extent that the density of electrons at the surface exceeds that of the holes. Thus, an inversion has taken place where the density of minority carriers is greater than that of the majority carriers at the surface. The band diagram for inversion is shown in Fig. 1.3(c).

By setting the gate voltage such that the $\Phi_s \geq 2\phi_f$, the stack is in a condition called strong inversion, the band diagram for which is shown in Fig. 1.3(d). In this condition there is a high density of electrons at the surface. In the context of MOS function, the region containing the high density of inversion charge carriers is called the channel. Electrons in the channel will flow to the drain electrode due to a potential difference applied between the source and drain. While the current is flowing, the device is in the *on* state. By lowering the gate voltage, the density of electrons in the channel, and likewise, the current drop off exponentially, bringing the device to the *off* state. The critical value of the gate voltage where $\Phi_s = 2\Phi_f$ is called the threshold voltage (V_t). In the case of an MOS stack where the bands are flat in the absence of gate voltage, the threshold voltage is given by equation 1.7.

$$V_t = \Phi_{ox} + 2\phi_f \tag{1.7}$$

The device described above is a n-MOS device, as n-type carriers comprise the current in the *on* state. For a p-MOS device (n-Si substrate), the same description as the one given above applies, but with the opposite sign for the gate voltage. A negative gate voltage will draw minority carriers (holes) and induce a negative Φ_s. When the gate voltage is applied such that $\Phi_s \leq 2\Phi_f$, the device will be in strong inversion, giving a sufficient hole concentration in the channel for the current to flow to the drain.

1.5 Flatband Voltage

A quantity called the flatband voltage (V_{fb}) describes the band bending in the semiconductor of an MOS stack that occurs without any applied voltage. The flatband voltage is the amount of gate voltage that would have to be applied across the stack to make the band edges in the oxide and the semiconductor flat. One factor that causes band bending in the semiconductor is a difference in work function between the metal and the semiconductor. Fig. 1.4(a) shows n-MOS materials before they are in contact. The energy levels are aligned with respect to the vacuum level, in accordance with the Schottky-Mott model of band alignment. The work function of the metal is less

than that of the semiconductor, i.e, the Fermi level of the metal is above that of the semiconductor.

When the materials shown in Fig. 1.4(a) are put in contact, and the metal and the semiconductor are electrically connected to each other, electrons flow from the metal to the semiconductor through the electrical connection to equalize the Fermi levels, bringing about thermal equilibrium. The resulting band diagram is shown in Fig. 1.4(b). According to charge neutrality, the metal has a net positive charge and the semiconductor has a net negative charge. Thus, there is an electric field between the metal and the semiconductor that penetrates some distance into the semiconductor, but only a negligible distance into the metal where it is perfectly screened. As in the condition of depletion described above, negatively ionized dopants in the depletion region of the semiconductor screen the bulk of the semiconductor from the electric field.

In this way, the work function difference (Φ_{ms}), defined $\Phi_{ms}=\Phi_m-\Phi_s$, results in a potential difference across the stack. The work function difference is exploited in a typical MOSFET to lower the threshold voltage. The MOS stack shown in Fig. 1.4(b) has already been brought into inversion by the work function difference, and the positive gate voltage needed to bring the stack into strong inversion is smaller than it is for the case where the metal and the semiconductor work functions are equal.

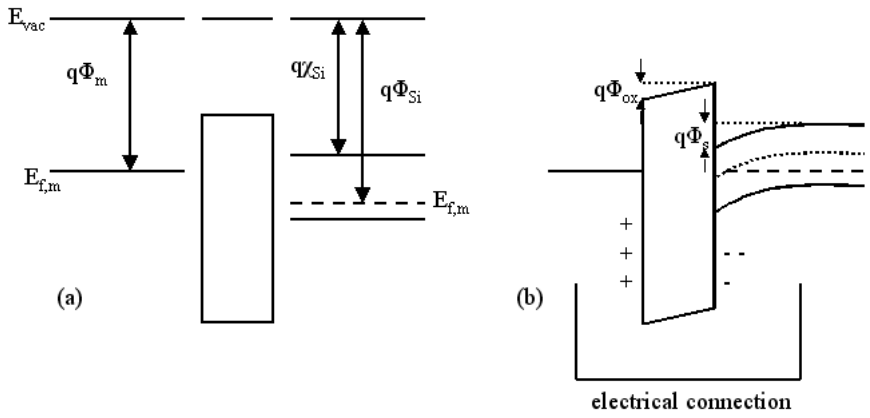

Figure 1.4: Band diagrams of an n-MOS stack (a)before and (b)after contact.

Another factor that can bend the bands in the semiconductor is charged defect states in the oxide. An example of such a defect state is an oxygen vacancy, which often is

positively charged.[29] A net charge in the oxide will cause charge rearrangement in the semiconductor to screen the electric field due to the charge in the oxide. The MOS stacks shown in Fig. 1.5(a) and (b) demonstrate the effect of a net charge in the oxide on the semiconductor and oxide band edges. The oxide shown in Fig. 1.5(a) has positively charged defects near the oxide-semiconductor interface. This induces negative screening charge in the semiconductor, bending the semiconductor bands downward. It also induces negative screening charge in the metal, resulting in an electric field in the oxide. A net negative charge in the oxide, as shown in Fig. 1.5(b), induces positive screening charge in the semiconductor, bending the bands upward, and positive screening charge in the metal.

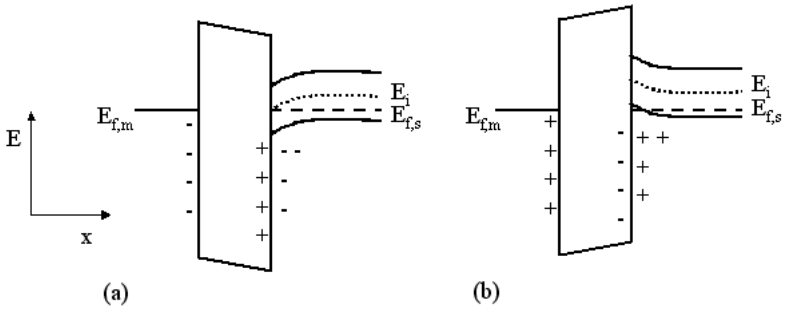

Figure 1.5: Band diagrams of an MOS stack with (a)positive (b)negative charged defect states in the oxide layer.

Equation 1.8 defines the flatband voltage, where the first term is the contribution from metal-semiconductor work function difference and the second term is the contribution from charged defect states in the oxide. In the second term, $\rho(x)$ is the density of charged defect states in the oxide. The integration is carried out from x=0, at the metal-oxide interface, to x=t_{ox}, at the oxide-semiconductor interface. The integral is often separated into two terms, as expressed in equation 1.8, where the first of these is the contribution to the flatband voltage from the charge density at the oxide-semiconductor interface (Q_i), and the second is the contribution from the fixed charge in the bulk of the oxide, which is assumed to have a uniform density (ρ). The threshold voltage is shifted by the flatband voltage as shown in equation 1.9. In the measurements we have made of high-κ oxide/Si samples, we have observed downward band bending in the Si. A possible explanation for this observation is net charge in the oxide layers.

$$V_{fb} = \Phi_{ms} - \frac{1}{\varepsilon_{ox}} \int_0^{t_{ox}} x\rho(x)\, dx = \Phi_{ms} - \frac{Q_i t_{ox}}{\varepsilon_{ox}} - \frac{\rho t_{ox}^2}{2\varepsilon_{ox}} \tag{1.8}$$

$$V_t = V_{fb} + V_{ox} + 2\Phi_f \tag{1.9}$$

1.6 Band Alignment Models

The simplest model used to predict the band offsets at an interface between two materials is the Schottky-Mott (SM) model. This model has been used in all of the band diagrams shown up to this point. In the SM model, the energy levels of materials in contact are aligned with respect to the vacuum level. The SM model is useful because of its simplicity, but it has been shown to be inaccurate due to its neglect of the interactions that take place between materials at interfaces.

In the SM model, band offsets are very easy to calculate. The metal-oxide CBO ($\Delta E_{c,mo}$) is the metal work function minus the oxide electron affinity, given in equation 1.10. The oxide-semiconductor CBO ($\Delta E_{c,os}$) is the semiconductor electron affinity minus that of the oxide, which is given in equation 1.11. These relationships are evident in the band diagram in Fig. 1.2.

$$\Delta E_{c,mo} = q\Phi_m - q\chi \tag{1.10}$$

$$\Delta E_{c,os} = q\chi_s - q\chi_o \tag{1.11}$$

The shortcomings of the SM model were discovered when the CBO of many metal-semiconductor interfaces were measured and found to differ significantly from the values predicted by the model.[30, 31] A pattern was observed where the CBO's for metal/semiconductor systems with the same semiconductor and several different metals with widely differing work functions were nearly the same. This was called Fermi level pinning (FLP) because the metal Fermi level was not free to move to the energy within the semiconductor band gap predicted by the SM model, but rather was pinned at a particular energy with respect to the semiconductor CBM. Bardeen proposed that there

were states at the metal-semiconductor interface that determined the energy within the semiconductor band gap at which the metal Fermi level was pinned, which he called the charge neutrality level (CNL).[30] The CNL is defined as the energy where the interface states have an equal density of donor type states above and acceptor type states below.

In the years after Bardeen proposed this model, vacuum technology improved so that interfaces could be grown with significantly less impurities, but FLP was still a prevalent issue. The interface gap state model (IGS) model was developed to incorporate both the SM and Bardeen models into a single model that could be used to calculate CBO values. An important physical insight into origin of the interface states was given by Louie *et al.*[32] In this work it was shown that, at a metal-oxide interface, states from the metal penetrate into the oxide in the energy region of the band gap and decay exponentially, having a significant amplitude only in the first ∼1-2 Å of the oxide. The distance that metal states penetrate into the oxide before decaying is a measure of the degree of the FLP at that interface.[33]

The charge of a metal-oxide interface is determined by the relationship between the metal Fermi level ($E_{f,m}$) and the CNL of the oxide when the vacuum levels of these materials are aligned. The CNL for a given oxide is determined from analysis of the complex band structure of the oxide.[34] If the metal Fermi level is equal to the CNL, then the interface states are filled up to the CNL, and the interface is neutral. If the metal Fermi level is below the CNL, then there are unfilled acceptor states below the CNL, which gives the interface is a positive charge. If the metal Fermi level is above the CNL, there are filled donor states, and the interface is negatively charged. A charge at a metal-oxide interface will induce screening charge in the metal, which will be localized near the interface in the metal, thus forming a dipole at the interface.

The calculation of a metal-semiconductor CBO in the IGS model is similar to that in the SM model, except that in place of the metal work function ($q\Phi_m$), a quantity called the effect work function ($q\Phi_{m,eff}$) is substituted. The effective work function is defined in equation 1.12, where $q\Phi_{cnl}$ is the difference between the vacuum level and the charge neutrality level, and S is the slope parameter, which describes the the degree of Fermi level pinning. The slope parameter can take on a value between 0 and 1. S=1 is

known as the Schottky limit, where the effective work function is the same as the work function and the SM model is recovered. S=0 is the Bardeen limit, where the effective work function equals $q\Phi_{cnl}$. In this case, the metal Fermi level will be pinned at the charge neutrality level, thus fixing the value of the CBO, regardless of the metal work function. In practice, the S value for a semiconductor or an oxide is always somewhere between 0 and 1. The value of S can be found from the empirical relationship given in equation 1.13, where ε_∞ is the high frequency component of the dielectric constant of the oxide.[35]

$$q\Phi_{m,eff} = q\Phi_{cnl} + S(\Phi_m - \Phi_{cnl}) \tag{1.12}$$

$$S = (1 + 0.1(\varepsilon_\infty - 1)^2)^{-1} \tag{1.13}$$

The interface dipole that forms as a result of charge at the interface has the effect of shifting the band offset from the Schottky limit value towards the Bardeen limit value. Fig. 1.6(a) shows an example where a low work function metal is in contact with an oxide. The positive end of the interface dipole is in the metal, which shifts the Fermi level of the metal downward and increases the CBO from the value predicted by the SM model (ΔE_{SM}) to that predicted by the IGS model (ΔE_{IGS}). Another example is shown in Fig. 1.6(b), where the CBO between a high work function metal and the same oxide is reduced by the interface dipole, which is negative on the metal side.

The full form of the equation used to calculate a metal-oxide or metal-semiconductor CBO is given in equation 1.14. We will use this equation to calculate CBO values to compare to metal-oxide CBO values that we have measured. The CBO between a semiconductor and an oxide can also be calculated in the IGS model. This is done by equation 1.15. The applicability of this model to actual high-κ/Si interfaces is limited, however, by the presence of the SiO_2 interfacial layer. The interfacial SiO_2 layer between the high-κ oxide and the Si substrate means that the latter two materials do not share a common interface, and thus, the IGS model cannot be appropriately applied to calculate the CBO between these materials.

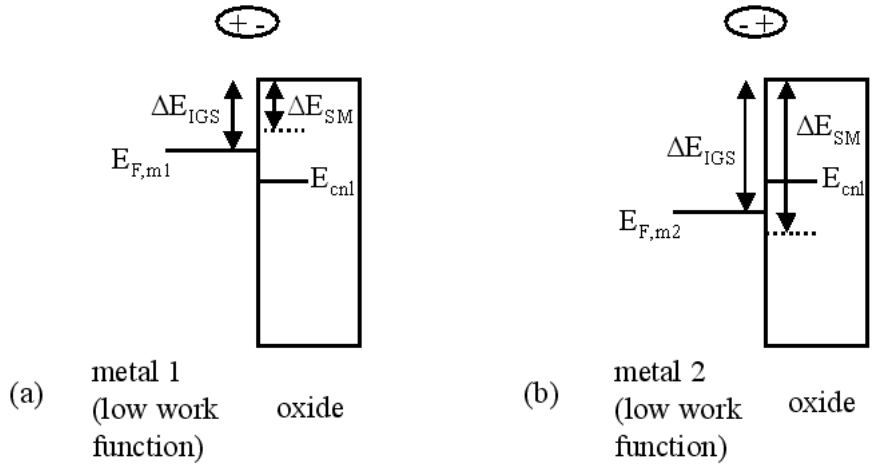

Figure 1.6: The interface dipole shifts the CBO from the Schottky limit value toward the Bardeen limit value.

$$\Delta E_c = q(\Phi_{cnl,ox} + S(\Phi_m - \Phi_{cnl,ox}) - \chi_{ox}) \tag{1.14}$$

$$\Delta E_c = q((\chi_s - \Phi_{cnl,s}) - (\chi_{ox} - \Phi_{cnl,ox}) + S((\Phi_{cnl,s} - \Phi_{cnl,ox})) \tag{1.15}$$

1.7 Alternative Gate Electrode Materials

Highly doped poly-Si has been used as the gate electrode material due to the fact that its work function can be tuned with doping, it has a low defect interface with SiO_2, and it is stable during the high temperature (T>1000°) anneal. A typical n-MOS device has a highly doped n-Si gate. The work function difference for n-Si gate/p-Si substrate pair is negative, reducing the amount of gate voltage needed to attain the threshold voltage, as given in equation 1.9. Similarly, a p-Si gate would be used with a n-Si substrate in a p-MOS device to reduce the threshold voltage.

One disadvantage of using a Si gate is that a depletion region forms in the gate. This puts an additional capacitance in series with the oxide capacitance, which reduces the overall capacitance, as they add reciprocally. When the gate voltage is applied to put the device in strong inversion, the depletion region in the gate increases, reducing the total capacitance further. Gate depletion was less of a problem five to ten years ago when oxide capacitance was smaller, but as the oxide capacitance increases, the

percentage by which it is reduced by the gate depletion becomes greater, making it more of a pressing problem. Another disadvantage of a Si gate is the problem of dopant diffusion. Si dopants, particularly boron, diffuse from the gate into the oxide and semiconductor during the high temperature anneal and degrade the electrical performance of the device. By replacing the Si gate with a metal gate, the problems of gate depletion and dopant diffusion would be eliminated.

The impending use of high-κ gate dielectrics has added another motivation for the use of metal gate electrodes in complementary MOSFETs or CMOS devices. A CMOS device contains two MOSFETs, one n-MOS and one p-MOS, that share a common drain electrode. In order provide work function differences to keep V_t low for each device, an n-Si gate is used for the n-MOSFET, and a p-Si gate is used for the p-MOSFET. Si gates on MOSFETs with high-κ dielectrics, however, have been shown not to produce the desired lowering of $|V_t|$ for both types of devices. This is attributed to Fermi level pinning, which prevents the full shifting of the two Fermi levels in a given stack by the amount predicted by Schottky-Mott based MOS model.[36] Thus, Si gates have been shown to be insufficient for use in high-κ CMOS devices, and suitable metal gates are in great demand. A low work function metal is needed for the n-MOS gate and a high work function metal is needed for the p-MOS gate. The work function alone, however, does not make a material an appropriate gate electrode.

As with high-κ materials, a number of gate electrode candidate materials have been investigated on the basis of thermal and chemical stability in contact with high-κ oxides, band offsets, and ability to lower threshold voltage.[37] Some metals have shown a tendency to diffuse throughout the MOS stack and are disqualified on this basis. Many of the low work function metals are highly reactive, which can affect the composition of the oxide film, as well as the band offsets and the threshold voltage. We have investigated the properties of one high work function metal, Ru, and two low work function metals, Al and Ti. We measured the band offsets between these metals and various high-κ oxides, and studied the chemical composition of the metal layers as well as their effect on the composition of the underlying oxide layers. These results will be presented and discussed in Chapter 4.

1.8 Importance of Band Offsets

Excessive gate leakage current across the ultra-thin oxide is a major obstacle to the continued scaling of MOSFET's. Use of a high-κ gate dielectric is expected to reduce direct tunneling leakage current due to greater physical thickness, but may allow additional leakage current by other mechanisms associated with a reduced CBO. There are four mechanisms for gate leakage current in a MOSFET. They are Fowler Nordheim tunneling, direct tunneling, Poole Frenkel tunneling and Schottky emission. In all of these mechanisms, the current density depends on the CBO, which will be referred to as the barrier height (E_B) in the discussion below. It should also be noted that the *electron* tunneling current is discussed below and not that of *holes*. The hole tunneling current is generally much lower due to lower hole mobility and greater barrier height for holes. Thus, it is less problematic than electron tunneling current.

Fowler-Nordheim (FN) tunneling is the quantum tunneling of an electron through a triangular potential barrier, as shown in Fig. 1.7(a). The current density for FN tunneling is calculated using the WKB approximation, which can be employed when the change in potential is small over one wavelength of the tunneling electron. Equation 1.16 gives the FN tunneling current density (J_{FN}), where m^* is the effect mass of the tunneling electron in the oxide, and A and B are constants.[38] This equation shows that the FN current density has a very strong inverse relationship with the barrier height and oxide thickness and a strong, but slightly weaker, inverse relationship with the effective mass.

$$J_{FN} = \frac{AV_{ox}^2}{E_B t_{ox}^2} \exp(-\frac{B\sqrt{2m^*}E_B^{3/2}t_{ox}}{V_{ox}}) \tag{1.16}$$

Direct tunneling (DT) is tunneling through a trapezoidal barrier, which is shown in Fig. 1.7(b). Equation 1.17 gives the direct tunneling current density (J_{DT}), which is derived in a similar way to that for FN tunneling, but with a different shape for the potential barrier.[38] This equation has also been simplified further using the assumption of a strongly degenerate accumulation layer in the substrate Si. As with the FN equation, the current density for DT has a strong inverse relationship with the barrier

height, oxide thickness, and the effective mass. In the case where, qV_{ox}=E_B, the FN equation is recovered.

$$J_{DT} = \frac{AV_{ox}^2}{E_B t_{ox}^2 (1 - \sqrt{\frac{E_B - qV_{ox}}{E_B}})^2} \exp(-\frac{B\sqrt{2m^*}E_B^{3/2} t_{ox}}{V_{ox}} (\frac{E_B^{3/2} - (E_B - qV_{ox})^{3/2}}{E_B^{3/2}})) \tag{1.17}$$

Poole-Frenkel (PF) tunneling is also called trap assisted tunneling, where an electron tunnels to an unoccupied defect (trap) state, then to another one, and eventually to the other side of the barrier, as shown in Fig. 1.7(c). Equation 1.18 gives an equation for PF tunneling current density.[39] This equation shows that the current density is inversely proportional to the oxide thickness, and it is inversely proportional to the exponential of the barrier height. PF current is also temperature dependent because thermal excitation can propel an electron over an activation barrier from one defect state to another. The PF current density is proportional to the exponential of the temperature. Using this property PF tunneling can be identified and distinguished from FN and DT tunneling, which are only weakly temperature dependent.

$$J_{PF} = \frac{CV_{ox}}{t_{ox}} \exp(\frac{-E_B + q\sqrt{\frac{qV_{ox}}{t_{ox}\pi\varepsilon_{ox}}}}{kT}) \tag{1.18}$$

Current due to Schottky emission (SE) consists of electrons that have been thermally excited to energy levels above the energy barrier and propelled across the oxide by the applied voltage as shown in Fig. 1.7(d). SE current density (J_{SE}) is given by equation 1.19, where A is the Richardson constant, given by equation 1.20.[39] The SE current density is inversely proportional to the exponential of the barrier height, independent of oxide thickness, and has a strong direct relationship with temperature. As with PF tunneling, the temperature dependence of SE tunneling allows it to be identified as the dominant current mechanism. SE is most prominent in cases where the barrier height is low ($E_B \leq$1.0 eV).

$$J_{SE} = AT^2 \exp(\frac{-E_B + q\sqrt{\frac{qV_{ox}}{4t_{ox}\pi\varepsilon_{ox}}}}{kT}) \tag{1.19}$$

$$A = \frac{4\pi e m^* k^2}{h} \tag{1.20}$$

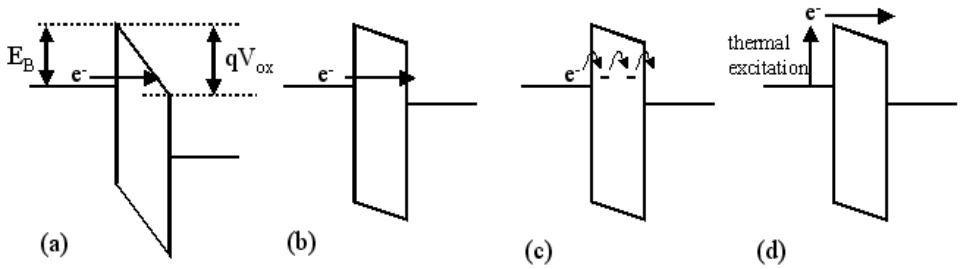

Figure 1.7: Schematic diagram of (a) Fowler Nordheim (b) direct (c) Poole Frenkel (d) Schottky emission tunneling mechanisms.

This discussion shows the strong inverse relationship between gate leakage current and barrier height (CBO) for all four current mechanisms. Clearly, the CBO of a high-κ dielectric with the semiconductor is an important criteria on which to judge the material, so an accurate value must be obtained. An accurate value of the CBO is also useful for understanding and modeling the gate leakage current. As discussed above, the dominant current mechanism can be identified to some degree, and thus, the gate leakage current can be modeled. As the barrier height (CBO) is one of the central parameters in the model of each mechanism, an accurate CBO value is critical to the accurate modeling and understanding of the gate leakage current.

1.9 Measurement of Band Offsets

There are three main methods used to measure the oxide-semiconductor CBO. They are electrical, opto-electrical and spectroscopic methods. The electrical method involves extraction of the CBO from the measurement of current across the oxide as a function of voltage. This is a difficult task because one model of current density must be used, but more than one current mechanism may contribute to the current density. Also, uncertainty in the value of the effective mass, which is difficult to determine precisely, will contribute to uncertainty in the CBO. The electrical method of determining a CBO was commonly used for metal-semiconductor heterojunctions where the CBO is small ($\leq$1 eV) and Schottky emission is the dominant current mechanism.[31] This method

has been less commonly used to find the CBO between high-κ gate dielectrics and semiconductor substrates.

Internal photoemission is an opto-electrical technique where the band offsets are extracted from the measurement of a photo-induced current across an MOS stack. In this measurement, a monochromatic beam of light illuminates an MOS stack, across which a potential difference is applied. The energy of the light is slowly increased over a given range, and current is measured as a function of photon energy. A CBO is found from the photon energy that corresponds to the onset of photo-induced current. This CBO depends on the voltage applied across the stack. In order to find the CBO at zero bias voltage, a CBO is determined at several different voltages, and these are used to extract the CBO at zero voltage. One difficulty with this method arises from the background current, which will be high if the oxide is too thin, making the location of the threshold energy for current uncertain. To avoid this problem, thick oxide layers (t_{ox} >50 Å) are used to lower the background current.[40] Thus, IntPE is unable to measure the band offsets for thin high-κ layers (t$\sim$20 Å), which are the thicknesses that will be used in devices. The properties of high-κ films can depend on thickness, so it is important to measure the properties of films of the appropriate thicknesses.[40]

The most common spectroscopic method of measuring the CBO involves using X-ray photoelectron spectroscopy (XPS) to measure the core levels of a system. The first steps in this method are to measure the energy difference between a core level and the VBM for both the high-κ oxide and the semiconductor of interest.[41] Then a thin high-κ oxide/Si system is measured using XPS to observe energy of the core level from each material. From the energy difference between the core levels, and the energy difference between the core level and the VBM for the respective materials, the VBO between the materials can be determined.

XPS can also be used to measure the oxide band gap through the onset of the loss feature on the high binding energy side of a core level.[42] The precision of finding the band gap this way is limited, however, because the slope of the loss feature is not very different from that of the background of the XPS spectrum. Once the VBO is known and the oxide band gap is measured, an accepted value for the semiconductor band gap

can be used in conjunction with these parameters to find the CBO between the oxide and the semiconductor. An alternative to direct measurement of the oxide band gap is to use a literature value. This approach is also prone to uncertainty in that the oxide band gap has been shown to vary with sample preparation.[43, 44]

We have used UV photoemission spectroscopy (UPS) to measure the occupied DOS of thin film high-κ oxide/semiconductor samples, and inverse photoemission spectroscopy (IPS) to measure the unoccupied DOS. The combination of these techniques gives a measurement of occupied and unoccupied DOS with respect to the Fermi level, which is used to directly extract the oxide VBM and CBM, and hence, the oxide band gap. From soft X-ray photoemission spectroscopy (SXPS) measurements performed on high-κ oxide/semiconductor samples in a separate vacuum system, we measured the Si VBM, and thus, we could determine the oxide-semiconductor VBO and CBO. This method we used avoids several of the difficulties encountered by the other methods I have discussed. It involves a straightforward extraction of parameters, thus, avoids the use of a complex (and perhaps, incomplete) model to extract the CBO, as in the electrical method. It is capable of measuring oxide films which are of the thickness being considered for use in devices, unlike IntPE. With regards to the XPS technique, it gives a more precise measure of the band gap than that determined from the XPS band gap measurement, and, therefore, a more precise measure of the oxide-semiconductor CBO. Also, it is more reliable than the XPS measurements that refer to a literature value for the oxide band gap to determine the CBO.

1.10 Energy Level Alignment in Dye Sensitized Solar Cells

The method of combining UPS and IPS measurements in one UHV chamber is also useful for measuring the energy level alignment between a layer of molecules and an oxide substrate. We have applied these measurements to dye/TiO_2 and dye/ZnO systems, which comprise the core of dye sensitized solar cells (DSSC). DSSC's have been the subject of much investigation over the past 15 years because they are a promising low cost alternative to Si solar cells.[45]

A DSSC consists of transparent conducting oxide (TCO) coated glass plates that form part of a sealed container, as shown in Fig. 1.8. The surfaces of the glass plates inside the container each have an additional coating: one is coated with a TiO_2 nanoparticle film, while the other is coated with Pt. The TiO_2 nanoparticle film is covered with dye molecules and immersed in an electrolyte solution. An electrical circuit is connected to the sealed compartment such that current can flow between the TiO_2 film on one of the plates and the Pt coating on the other.

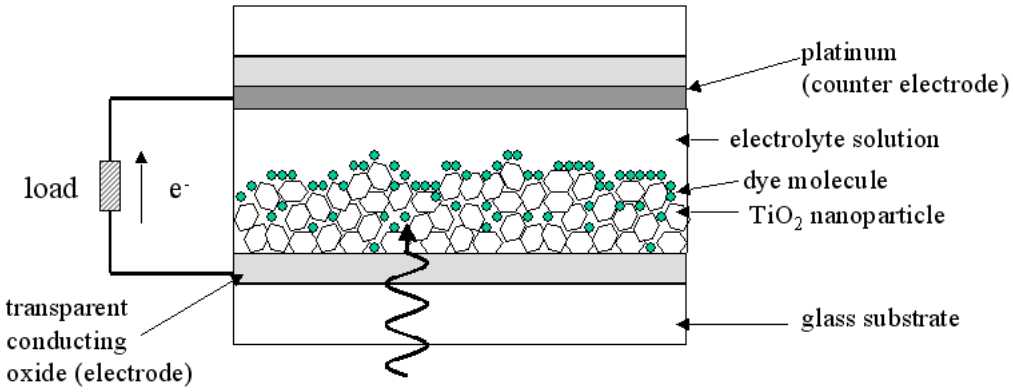

Figure 1.8: Schematic diagram of a dye sensitized solar cell.

A DSSC solar cell works by absorbing photons from the sun with dye molecules. Each absorbed photon excites an electron-hole pair in a dye molecule, which is macroscopically separated when the excited electron is transferred into the TiO_2 conduction band, and the hole is filled by an electron from an anion in the electrolyte. The electron moves through the TiO_2 film and then into the electric circuit, while the oxidized anion diffuses throughout the solution. The process is complete when the electron is donated back to an oxidized anion at the Pt covered glass surface. In this way, sunlight is continuously converted into electrical energy .

The key electronic levels of the dye molecule are known as the highest occupied molecular orbital (HOMO) and the lowest unoccupied molecular orbital (LUMO). The alignment of these levels with respect to the VBM and CBM of TiO_2, shown in Fig. 1.9, is central to the function of a DSSC. In particular, the LUMO of the dye molecule should be above the CBM of the TiO_2 so that an electron in the LUMO can be transferred into the TiO_2 conduction band. Using the combination of UPS and IPS, we have measured

HOMO-LUMO gap and the TiO_2 band gap, as well as the alignment between the HOMO and LUMO and band edges of the TiO_2. This is the first full characterization of the electron level alignment at the dye/TiO_2 and dye/ZnO interfaces by electron spectroscopic methods.

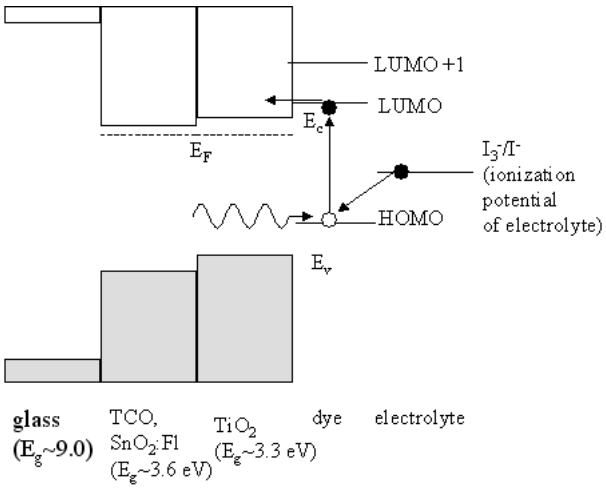

Figure 1.9: Band diagram of a dye sensitized solar cell.

1.11 Outline of Thesis

In this thesis, we show that the combination of UPS and IPS can be applied to a wide range of systems to gain useful information about the electronic structure. The outline of the thesis is as follows. In Chapter 2, a description of the experimental setups of UPS and IPS, as well as other experimental techniques we have used, is given. Measurements of the band offsets of MOS stacks will be presented in Chapters 3 and 4. Chapter 3 contains results for the band offsets between an oxide thin film and a Si substrate for a number of different oxide/Si systems. In Chapter 4, a systematic study of the band offsets between a metal overlayer and an oxide film is presented, where all combinations between Ru, Al and Ti metals and HfO_2, $Hf_{0.7}Si_{0.3}O_2$, Al_2O_3 and SiO_2 films on Si have been investigated. The measured band offset values are compared to band offset values determined using the interface gap state model in to evaluate the effectiveness of the model for these systems. In Chapter 5, the measurement of the energy level alignment for dye sensitized solar cell materials is presented. We have measured the electron level

alignment between a molecular layer and an oxide substrate for all combinations two molecules (N3 dye and isonicotinic acid) and three substrates (rutile $TiO_2(110)$, anatase TiO_2 nanoparticles and a $ZnO(11\bar{2}0)$ epitaxial film). The results for these systems are compared to each other and to results from the literature.

Chapter 2

Experimental

2.1 Introduction

The two parts of this thesis are the measurement of the band offsets between layers of metal-oxide-semiconductor (MOS) stacks with metal gates and high-κ oxides, and the measurement of the electronic level alignment at the organic dye/oxide interface. We used UV photoemission spectroscopy (UPS) to measure the occupied density of states (DOS) and inverse photoemission spectroscopy (IPS) to measure the unoccupied DOS of these systems, from which we extract information such as the band offsets and energy level alignment. These measurements were performed in an ultra high vacuum (UHV) chamber at Rutgers University with a base pressure of 5×10^{-10} Torr. The UHV environment was necessary so that a sample surface could be cleaned and kept clean for a period of time of several hours, during which time measurements were performed. In addition to UPS and IPS, Auger electron spectroscopy (AES) and low energy electron diffraction (LEED) were used to evaluate the preparation of samples in the vacuum. We also performed soft x-ray photoemission measurements (SXPS) at beamline U5 at the National Synchrotron Light Source (NSLS) at Brookhaven National Laboratory to supplement our measurements at Rutgers. In this chapter, all of the aforementioned experimental techniques will be described.

2.2 Ultra High Vacuum

A UHV environment is created inside a sealed stainless steel vacuum chamber by the use of a combination of vacuum pumps. A rotary vane pump is first used to bring the pressure down from atmospheric pressure (760 Torr). In this pump, a vane is swept

through a volume where gas enters from the chamber. The vane traps gas and pushes it to an outlet port where, in its compressed state, it is released into the atmosphere.[46] Once the rotary vane pump reduces the pressure in the chamber to ∼1 Torr, a turbomolecular pump can be turned on. This pump consists of several levels of rotating angled blades paired with stationary blades, called rotors and stators, respectively. The rotors transfer momentum to the gas molecules, pushing them towards the stators, where they pass through separations between the stators to the next level. The rotors and stators are successively closer at each level, resulting in a compression of the gas by a factor of ∼5 per level.[47] Thus, when the gas is pushed below the last stage, it will be forced to the outlet by the compressed gas in the lowest level of the pump. The ratio of the pressure at the outlet of the turbo pump to the pressure at the inlet, or the compression ratio, is approximately 10^6. The gas at the outlet of the turbomolecular pump is pumped away by a rotary vane pump.

When the pressure in the chamber is below 1×10^{-6} Torr, an ion pump can be turned on, which reduces the pressure further by trapping gas molecules. The primary parts of this pump are two parallel, Ti coated, stainless steel walls, and an array of stainless steel cylinders, the central axes of which are oriented perpendicular to the walls. A high voltage (3 kV) is applied between the walls, which are the cathode, and the cylinders, which are the anode. Electrons are emitted from the walls due to the high voltage and are forced to follow a helical path by a magnetic field of 1500 G directed along the axes of the cylinders. The electrons strike gas molecules, creating positive ions which are accelerated into the Ti coated walls of the pump by the high electric field, where they either become embedded or stick by chemisorption. The impact of the ions onto the cathode, in turn, causes some Ti to be emitted, which coats the surface of the anode and traps more gas molecules by chemisorption.[48] After the sputter-ion pump is turned on, the pressure will reduce to $\sim1\times10^{-8}$ Torr after several hours, but it will not reduce much further in the next few days due to water vapor in the chamber. To remove the water vapor the chamber must be heated to a temperature greater than 100°C for approximately 24 hours. After cooling, the pressure will be approximately 5×10^{-10} Torr, which is suitable for measurements.

2.3 Photoemission Spectroscopy

Photoemission spectroscopy (PS) is used to study the occupied electronic states of a sample. The measurement is performed by directing a mono-energetic photon beam onto a sample and collecting electrons that are emitted. The photoemission process for a single photon and electron is shown in Fig. 2.1 for a metal sample. A photon of energy $\hbar\omega$ is absorbed by an electron in an initial state with energy E_i, exciting the electron to a final state with energy E_f. If the energy of the final state is above the vacuum level (E_{vac}), the electron can escape the sample. The kinetic energy of a photoelectron that escapes without inelastically scattering gives information about its initial state, but this information is lost if the electron is scattered. The inelastic mean free path (IMFP), the average distance that an electron can travel in a solid before inelastically scattering, is an indication of the surface sensitivity of a photoemission measurement. For electrons in the energy range of our photoemission measurements (20-140 eV), the IMFP is approximately 10 Å.[49] Thus, the majority of the photoelectrons originate from a depth of 10 Å or less, making the measurements sensitive to the properties of the surface region.

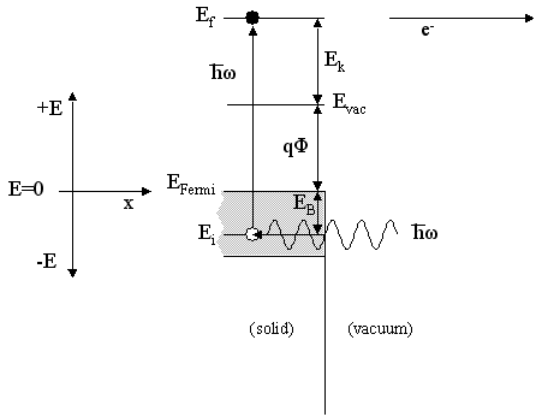

Figure 2.1: Schematic diagram of the photoemission process.

The energetics of a photoemission measurement can be described in a system consisting of a single incident photon and an N electron solid. The initial energy of the system is the photon energy ($\hbar\omega$) plus the energy of the N electron sample (E_N). After a photoemission event has occurred, the total energy of the system is composed of the

kinetic energy of the photoelectron (E_k) plus the energy of the N-1 electron system (E_{N-1}). Energy conservation dictates that the initial and final energies of the system are equal, as expressed in equation 2.1, which can be rewritten as equation 2.2.

$$\hbar\omega + E_N = E_k + E_{N-1} \tag{2.1}$$

$$E_k = \hbar\omega + (E_N - E_{N-1}) \tag{2.2}$$

In the independent electron picture of solids, where the interactions between electrons are neglected, the difference in energy between the N and N-1 electron systems equals the binding energy (E_B) of the initial state of the electron with respect to the vacuum level. It should be noted that in this definition, which is used in equation 2.3, the binding energy is a negative quantity. In many cases it is more convenient to define the binding energy with respect to the Fermi level. When the binding energy is defined in this way it is still a negative quantity, and the kinetic energy of the photoelectron is given by equation 2.4. The definition of the binding energy with respect to the Fermi level is in keeping with the energy scale shown for the schematic diagram in Fig. 2.1.

$$E_k = \hbar\omega + E_B \tag{2.3}$$

$$E_k = \hbar\omega + E_B - q\Phi \tag{2.4}$$

Defining the binding energy with respect to the Fermi level is slightly problematic for a semiconductor because there are no states at the Fermi level, and thus no states to represent the Fermi level in the photoemission spectrum. Defining the binding energy this way is even more problematic for an oxide, which does not have a well-defined Fermi level. This issue will be discussed more in a later part of this section.

A photoemission spectrum is the number of photoelectrons collected as a function of the photoelectron kinetic energy. The spectrum (I(E)) is proportional to the density of occupied electronic states (N(E)) times the photoabsorption cross section (σ_{abs}(E)), as given in equation 2.5. [50] Thus, in order to find the density of occupied states, the cross

section, in principle, should also be known. The photoabsorption cross section is the absorbed energy per unit time divided by the incident energy flux. It is derived using the equation for the transition rate (Γ) for photoelectron excitation, known as Fermi's golden rule, given in equation 2.6. In this equation, $\vec{A}$ is the vector potential and $\vec{p}$ is the momentum of the incident light. The initial state (Ψ_i) is the bound state wave function of the electron in the solid and the final state (Ψ_f) is that of an unoccupied state in the solid to which the electron makes a transition.[51] The transition rate equation is derived by treating the electromagnetic field of the incident photon as a perturbation to the ground state Hamiltonian of the solid.

$$I(E) \propto N(E)\sigma_{abs}(E) \tag{2.5}$$

$$\Gamma = \frac{2\pi}{\hbar}(\frac{q}{mc})^2|\langle\Psi_f|\vec{A}\cdot\vec{p}|\Psi_i\rangle|^2\delta(E_f - E_i + \hbar\omega) \tag{2.6}$$

The matrix element in Fermi's golden rule can be simplified using the dipole approximation, where the spatial part of the vector potential of the incident light, given by $\exp(i(\vec{k_p}\cdot\vec{r}))$, is approximated as 1. This is valid because the wavelength of the incident light (λ_p) is long compared to a lattice spacing in the solid. The matrix element then reduces to $\langle\Psi_f|\hat{\epsilon}\cdot\vec{p}|\Psi_i\rangle$, where $\hat{\epsilon}$ is the polarization vector of the incident light. The expression for the differential absorption cross section per unit solid angle ($\frac{d\sigma_{abs}}{d\Omega}$), which is derived using the Fermi's golden rule in the dipole approximation, is given by equation 2.7. In this equation, $\vec{k}$ is the electron wave vector, ω is the angular frequency of the incident light and α is $\frac{2\pi q^2}{hc}$.[51] The absorption cross section has been calculated as a function of incident photon energy for electronic states of many materials. Observing the energy dependence of the cross section of a spectral feature is often a useful way to identify its orbital character.

$$\frac{d\sigma_{abs}}{d\Omega} = \frac{\alpha|\vec{k}|}{mh\omega}|\langle\Psi_f|\hat{\epsilon}\cdot\vec{p}|\Psi_i\rangle|^2 \tag{2.7}$$

Photoemission spectroscopy that uses incident UV light is called UV photoemission spectroscopy (UPS). The UV light source for our UPS measurements was a He discharge

lamp. In this device, He is differentially pumped through the lamp, and an electrical arc inside the lamp excites electronic transitions in the He atoms. The photons emitted from the He atoms move through a narrow glass tube to the sample. Two strong emission lines from He are used for UPS spectroscopy. A He I photon has an energy of 21.2 eV, and is given off when an electron decays from a $2p$ level to a $1s$ level in a neutral He atom. A He IIα photon has an energy of 40.8 eV, and is given off when an electron undergoes the same decay in a singly ionized He atom. The ratio of He II to He I light generated is increased by decreasing the pressure of He through the lamp. The energy widths of these emission lines are less than 0.1 eV.[52]

Photoelectrons are collected and energy analyzed in our measurements by a cylindrical mirror analyzer (CMA), a schematic diagram of which is shown in Fig. 2.2. A CMA works by the principle of electrostatic deflection. Its inner and outer cylinders are set to specific voltages, so that a photoelectron that has a kinetic energy within a narrow range about a given kinetic energy will pass between the mirrors and reach the 'channeltron' electron multiplier. A photoelectron with a kinetic energy above or below the this range will strike outer or inner cylinder, respectively, and be absorbed. By ramping the kinetic energy at which photoelectrons are collected in a stepwise fashion and counting the photoelectrons at each kinetic energy, a photoemission spectrum is obtained.

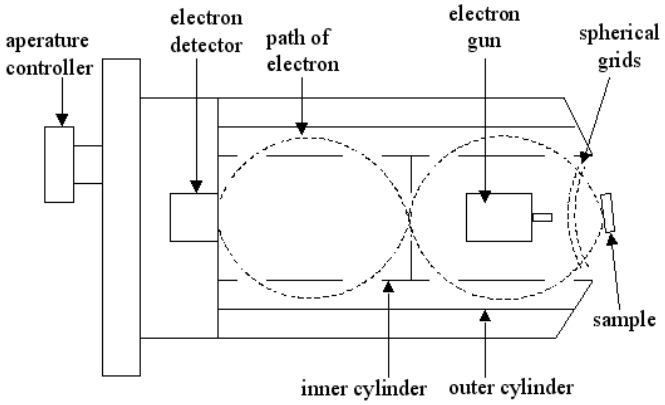

Figure 2.2: Schematic diagram of a CMA.

The channeltron electron multiplier consists of a glass cup with a curved glass tube extending off from it, as shown in Fig. 2.3. The inner surface of this device is coated

with a layer of SiO_2 on top of a conductive layer. When an electron strikes the inside of the cup, multiple electrons are emitted, on average, from the surface. These electrons are drawn down the tube by the applied bias as well as the curvature of the tube. A cascade effect ensues, and at the end of the tube there is a large amount ($\sim 10^7$) of electrons that enters into a wire. This current pulse is converted to a voltage pulse by the circuit shown in Fig. 2.3. The voltage pulse is amplified, shaped by electronic components and counted by a computer.

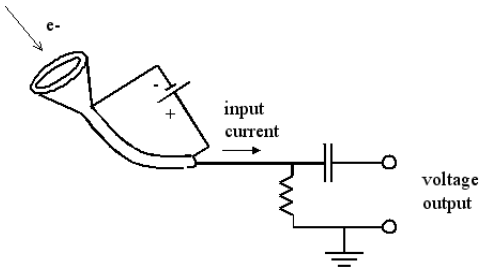

Figure 2.3: (a)Schematic diagram of a channeltron electron multiplier and the current to voltage conversion circuit.

In our UPS measurements, the CMA is operated in what is called the retarding mode. In this mode, the first spherical grid at the entrance aperture of the CMA is grounded to keep the space between the sample and the CMA free of an electric field. The second spherical grid is set to a negative voltage. These grids can be seen in Fig. 2.2. The negative voltage on the second grid reduces the kinetic energy of the photoelectrons so that all photoelectrons that reach the electron multiplier have a specific kinetic energy, known as the pass energy. Similar to the discussion above, only photoelectrons in a narrow range about a given kinetic energy will be reduced to the pass energy and reach the detector. Once again, the kinetic energy of photoelectrons that will reach the detector is ramped to measure the photoemission spectrum.

The resolving power of the energy analyzer is $E/\Delta E$, where E is the energy of the electrons reaching the detector, in this case the pass energy, and ΔE is the energy range of electrons reaching the detector, also known as the energy resolution. The resolving power is fixed by the geometry of the system. Thus, reducing the pass energy will reduce the energy resolution of electrons reaching the detector, which is commonly described as increasing the resolution of the analyzer. The majority of the UPS measurements

we did were taken with a pass energy of 15 eV, for which the energy resolution is ∼0.1 eV.[53] Using a lower pass energy will also reduce the count rate, requiring longer collection times to sufficiently increase the signal to noise ratio in the spectrum.

Earlier in this chapter, the problem of defining the binding energy with respect to the Fermi level of a band gap material was discussed. This problem arises from the fact that there are no states at the Fermi level of these materials. The samples that have been measured in this thesis are, in large part, oxide films on Si substrates, and are subject to this problem. The following discussion will explain how the occupied electronic states measured in an oxide/Si sample can be reported as a function of binding energy with respect to the Fermi level of the Si substrate. First, it must be noted that Fermi level of the Si in an oxide/Si sample is equal to that of all of the material that it is in thermal equilibrium with, i.e., with which it can exchange charge. This includes the sample holder, the vacuum chamber and the detector. Thus, the measured Fermi level of a metal sample that is in thermal equilibrium with an oxide/Si sample gives the Fermi level of the Si in the oxide/Si sample.

Fig. 2.4(a) and (b) show photoemission spectra from a Ta and and a HfO_2/Si sample, respectively, which are displayed as intensity (arbitrary units) vs. kinetic energy (eV). These samples were in thermal equilibrium with one another, and the spectra were taken at the same photon energy. In the spectrum from Ta, the highest kinetic energy electrons originated from the Fermi level of the Ta. The kinetic energy of electrons from the Fermi level (E_K^F) is found to be 34.5 eV by taking the inflection point of the high kinetic energy end of the spectrum, in accordance with the location of the Fermi level in the Fermi-Dirac distribution. This measurement of the Fermi level can be attributed to the HfO_2/Si sample because the two samples were in thermal equilibrium.

The energy scale of the HfO_2/Si spectrum can be converted to binding energy using equation 2.8. Equation 2.8 is calculated by subtracting equation 2.4 ($E_k=\hbar\omega+E_B-q\Phi$) for Ta from that for HfO_2/Si. In equation 2.4 for Ta, the kinetic energy equals the kinetic energy of an electron from the Fermi level ($E_K=E_K^F$), in which case $E_B=0$. The work function of the two samples is the same because the relevant work function is that of the detector, which is larger than those of the samples.

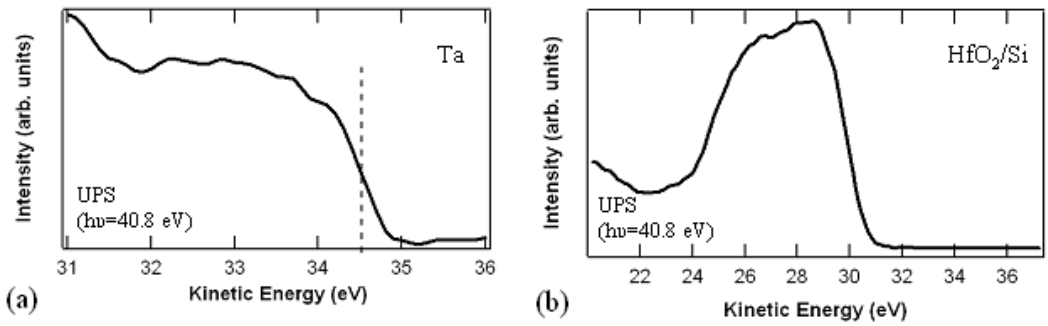

Figure 2.4: Photoemission spectra from a (a)Ta and a (b)HfO_2/Si sample, displayed as Intensity vs. Kinetic Energy. The vertical line in (a)indicates the kinetic energy of electrons originating from the Fermi level.

$$E_B = E_K - E_K^F \tag{2.8}$$

UPS can also be used the measure the difference in energy between the highest occupied electronic state and the vacuum level. Fig. 2.5 illustrates how this measurement is made by describing two electrons that represent the high and low kinetic energy edges of the spectrum shown in the figure. In this measurement, the sample is negatively biased by an amount V_B with respect to the detector, which has the effect of shifting all of the states in the sample up in energy so that the low energy edge of the spectrum can be clearly seen. Electron 1 is emitted from the Fermi level of the sample and thus, contributes to the high kinetic energy edge the spectrum. Electron 2 is originally bound in a state in the middle of the valence band. It absorbs a photon and makes a transition to an excited state, but it also loses energy by inelastic scattering (E_{IL}). Its final state energy is at the vacuum level, so it escapes the sample, but with a kinetic energy that is the lowest of all of the collected electrons. The width of the spectrum is the difference between the high and low kinetic energy edges of the spectrum.

Subtracting the spectrum width (W) from the incident photon energy gives the energy difference between the highest occupied state and the vacuum level. In a metal, this energy is the work function. In a semiconductor or insulator, this energy, which is known as the ionization energy, equals the band gap plus the electron affinity, as given in equation 2.9. We used this measurement to experimentally determine metal work

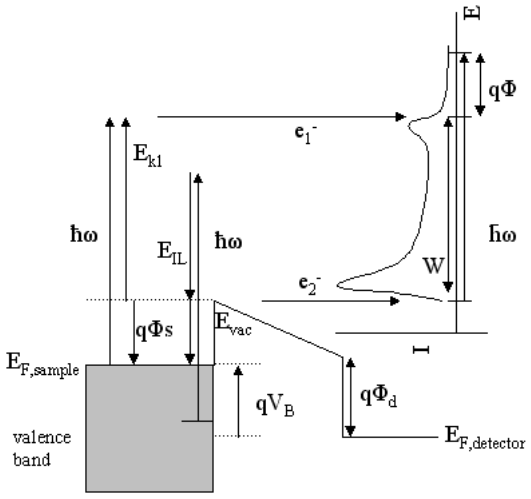

Figure 2.5: Schematic diagram of the spectrum width measurement.

functions and semiconductor and oxide electron affinities.

$$\hbar\omega - W = E_g + q\chi \tag{2.9}$$

In a synchrotron light source, a continuous spectrum of photons is emitted by electrons that are accelerated to high speeds and constrained to move in a circular path. A monochromator is used to select photons in a narrow energy range, which are then focused and directed at a sample. Photoemission measurements made at a synchrotron have the advantages of selection of photon energy and high photon flux. The analyzer used in our measurements at the National Synchrotron Light Source (NSLS) was a hemispherical mirror analyzer (HMA), which works by electrostatic deflection in a manner similar to that of a CMA. It has a higher resolution than a CMA due to its smaller entrance aperture.[54] The primary purpose of the photoemission measurements at the NSLS was to use a higher energy photon source than we had access to at Rutgers in order to measure the core levels of our samples. As the photon energy we used at the NSLS was in the soft X-ray range, these measurements will be referred to as soft X-ray photoemission spectroscopy (SXPS).

2.4 Inverse Photoemission Spectroscopy

Inverse photoemission spectroscopy (IPS) is initiated by directing a highly collimated electron beam with a well-defined energy at a sample. Electrons in the beam will enter the sample, and a subset of them will couple to high lying unoccupied states of the same energy, then decay to a lower lying unoccupied states, emitting photons. This process is illustrated for a single incident electron in Fig. 2.6. The energy of the photon is the energy difference between the initial and final states (E_i-E_f=$\hbar\omega$). As the energy of the initial state equals (the beam energy) is known, measuring the energy of the photon allows the determination of the energy of the final state of the electron. Thus, measuring the number of photons corresponding to each final state energy is a measure of the unoccupied electronic density of states of the material. As with photoemission, IPS is also sensitive to the properties of the surface, as the IMFP of the electrons in the beam, which commonly have energies of ∼20 eV, is ∼10 Å.

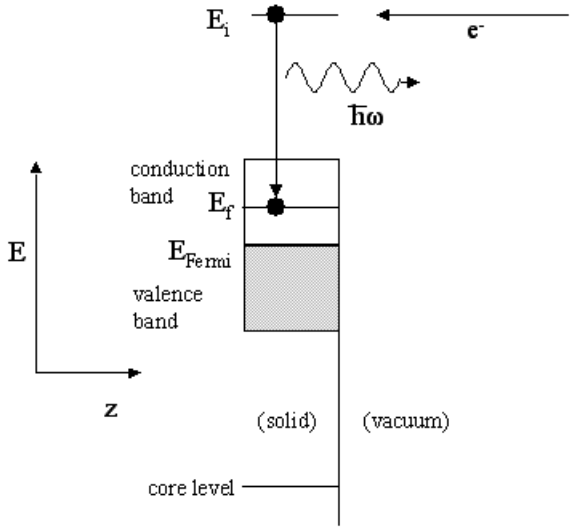

Figure 2.6: Schematic diagram of the inverse photoemission process.

Fermi's golden rule can also be used to describe the rate at which electrons in an IPS experiment undergo transitions from the initial to the final state. For emission of a photon, however, the outgoing electromagnetic field must be quantized for the transition rate to be non-zero. The differential emission cross section per unit solid angle ($\frac{d\sigma_{em}}{d\Omega}$) is shown in equation 2.10.[51] An interesting comparison between photoemission and

inverse photoemission can be made by dividing the differential emission cross section per unit area by that for absorption, equation 2.7. Assuming that the matrix elements are equal, this ratio is given by equation 2.11. The value of this ratio can be calculated for the typical electron (20 eV) and photon energies (40 eV) used in our measurements. It is found to be very small, on the order of 10^{-5}, which indicates that the IPS cross section is much smaller than that for PS. IPS count rates are, indeed, much lower than PS count rates, and IPS data must be collected over a significantly longer time period in order to obtain spectra with good signal to noise ratios. Apart from a smaller prefactor, however, the photoemission cross sections for atomic orbitals are the same as those for photoabsorption. Thus, the study of the energy dependence of the cross section of an unoccupied state can help to reveal its orbital character in the same way that it can for an occupied state.

$$\frac{d\sigma}{d\Omega_{em}} = \frac{\alpha\omega}{mc^2h|k|}|\langle\Psi_f|\hat{\epsilon}\cdot\vec{p}|\Psi_i\rangle|^2 \tag{2.10}$$

$$\frac{d\sigma_{IPS}}{d\Omega}/\frac{d\sigma_{PS}}{d\Omega} = (\frac{\lambda_e}{\lambda_p})^2 \tag{2.11}$$

In IPS, photons are collected in one of two ways. In an isochromat IPS system, only photons in a specific energy are collected. The incident energy of the electrons must be varied to probe a range of final states. In a grating spectrometer system, which was used in the measurements reported in this thesis, an electron beam of a fixed energy is incident on the sample and photons of many energies can be collected at once. The detector design is based on the Rowland circle, which employs the focusing and dispersing properties of a concave spherical mirror with parallel grooves.[55] This grooved, spherical mirror will be referred to as the grating.

Fig. 2.7(a) and (b) show the properties of a grating. The grating shown in these figures has a radius R_m and is tangent to the Rowland circle, which is in the **xy** plane and has radius R_c, where R_m=2R_c. An example of the focusing and dispersing of the grating is that rays of a given wavelength (λ_1) that emanate from point A in the horizontal (**xy**) plane and strike the grating will be refocused on the Rowland circle

at point B. Rays of a longer wavelength ($\lambda_2 > \lambda_1$) that originate from point A and emanate to the grating in the **xy** plane will be refocused on the circle at a point farther from the **y**-axis. In this way, the grating can be used to separate photons of different energies.

To consider the behavior of all of the rays of a given wavelength that emanate from a point on the Rowland circle and strike the grating, the property of astigmatism must be taken into account. An example of astigmatism can be seen in Fig. 2.7(a), where rays of λ_1 that emanate from point A and strike the grating along the projection of the **z**-axis onto the grating will be focused on point D. Thus, due to astigmatism, the focal point for rays of the same wavelength that originate from the same point, but traveling to the grating in different planes, is different.

A full consideration of the property of astigmatism shows that the set of rays of λ_1 that emanate from point A and strike the grating at random points will focus on a line perpendicular to the **xy** plane that passes through Rowland circle at point B, as shown in Fig. 2.7(a). This set of rays will also focus on a line in the **xy** plane and perpendicular to the **y**-axis that passes through point D. The Rowland circle is called the horizontal focus, and the line tangent to the Rowland circle and perpendicular to the **y**-axis (as shown in Fig. 2.7(b)) is called the vertical focus. As the distance from the **y**-axis increases, the horizontal and vertical foci become farther apart.

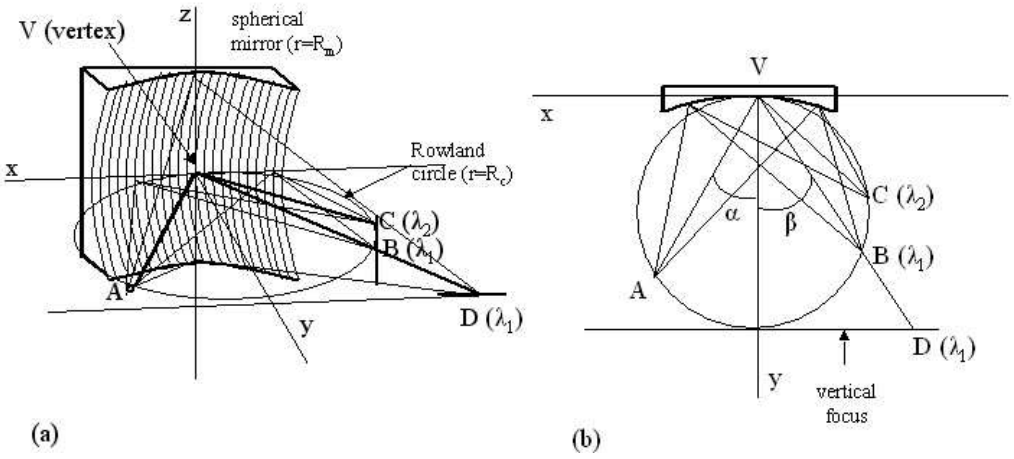

Figure 2.7: Schematic diagram of the properties of a spherical mirror with vertical grooves.

Fig. 2.8 shows the configuration of the grating spectrometer in our UHV system. The sample is effectively a point source of photons because the spot size of the electron beam is very small ($\sim$1 mm^2). The spherical diffraction grating disperses and focuses the light on the Rowland circle, where the photon detector is located. This detector can be moved along the Rowland circle to change the energy range of photons it detects.

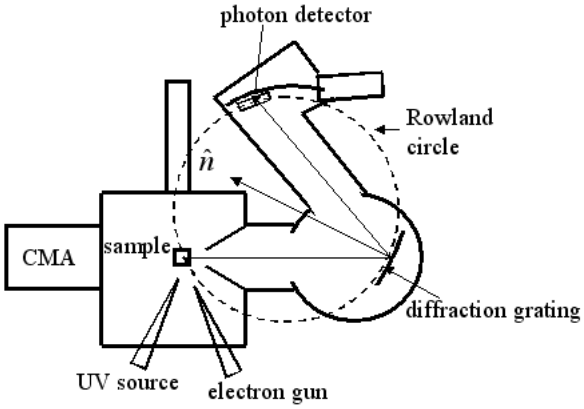

Figure 2.8: Schematic diagram of grating spectrometer IPS system and UPS system.

The photon detector consists of 2 microchannel plates and a resistive anode encoder, as shown in Fig. 2.9. When a photon hits the front of the first plate, it causes a group of electrons to be emitted that are accelerated through the plate and out the back side by the voltage across the plate. These electrons are emitted into the second plate where each one excites an additional group of electrons, which are accelerated through the plate and emitted toward the anode. When the cloud of electrons strikes the anode, which is a sheet of uniform resistance, it produces a current at each corner. The magnitude of the current at each corner, which are labeled A, B, C, and D in Fig. 2.9, is combined such that one position coordinate is given by the relation $\frac{I_A+I_B}{I_A+I_B+I_C+I_D}$, and the other position coordinate is given by $\frac{I_B+I_C}{I_A+I_B+I_C+I_D}$. These coordinates are expressed as two 8-bit digital numbers, so that the position of each photon is expressed as the coordinates of one location in a 256 by 256 grid. The coordinates of each photon are sent to the computer, which keeps a record of the number of photons that strike the detector at each location in the grid.

In the photon count array, one coordinate corresponds to position along the Rowland circle, which will be referred to as the horizontal channel number, and the other

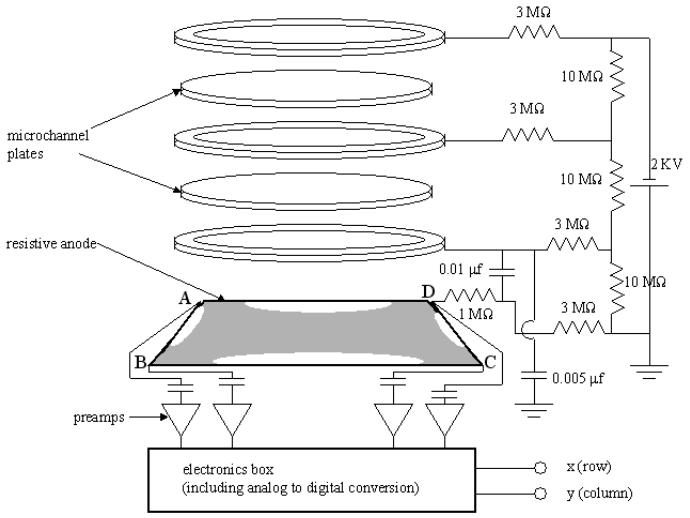

Figure 2.9: 2D position sensitive photon detector.

coordinate corresponds to position normal to the plane of the Rowland circle, which will be referred to as the vertical channel number. For each horizontal channel number, the photon counts for all of the vertical channel numbers are added, as all of these photons have the same energy. This gives the spectrum of photon counts as a function of horizontal channel number. The horizontal channel numbers must then be calibrated to energy. This is done by performing IPS on a clean Au sample. As an Au sample has unoccupied states that extend down to the Fermi level, the energy of the highest energy photons ($\hbar\omega_{max}$) is known to equal the energy of the incident electrons, as shown in Fig. 2.10. This diagram shows that the incident electron energy (E_e) equals the energy of the photon emitted by an electron that decays to a final state at the Fermi level. By taking IPS spectra at a number of different energies and finding the channel number that corresponds to the highest energy photons, one can determine a function that gives the photon energy as a function of horizontal channel number.

The theoretical resolution of the grating spectrometer can be calculated by equation 2.12, where m is the order of the interference point, R_c is the radius of the Rowland circle in meters, n is the number of grooves per mm and β is the angle of reflection of the light with respect to the mirror normal, as shown in Fig. 2.7.[55] For our system, R_c=750 mm, n=1200 lines/mm and β=25°. The calculated resolution the grating spectrometer is 0.06 eV for a photon energy of 19 eV and 0.04 eV for a photon energy

of 15 eV.

$$\frac{d\lambda}{dl} = \frac{\sin\beta}{2mR_c n\cos\beta}(10^4\frac{\mathring{A}}{mm}) \tag{2.12}$$

The electron gun is based on the design of Stoffel and Johnson, where a planar BaO cathode is heated by a filament.[56] Due to the elevated temperature, electrons in the cathode occupy energy levels up to the vacuum level, as shown in density of states (DOS) curve for the cathode in Fig. 2.10. Voltages in the gun extract, accelerate and focus the electrons to a spot size of $\sim$1 mm^2 on the sample. The energy of the electron beam is the voltage on the cathode plus the work function of the cathode ($q\Phi_c$=2.3 eV). The gun can produce a beam with an energy between 4 and 40 eV. The energy spread within the beam is the thermal width of the electrons (ΔE=kT) from the hot cathode, which is 0.2 eV for a typical cathode temperature of $\sim$2300°C. The energy resolution of the electron gun and the grating spectrometer add in quadrature, so the energy resolution of the electron gun is a very good approximation to the overall resolution.

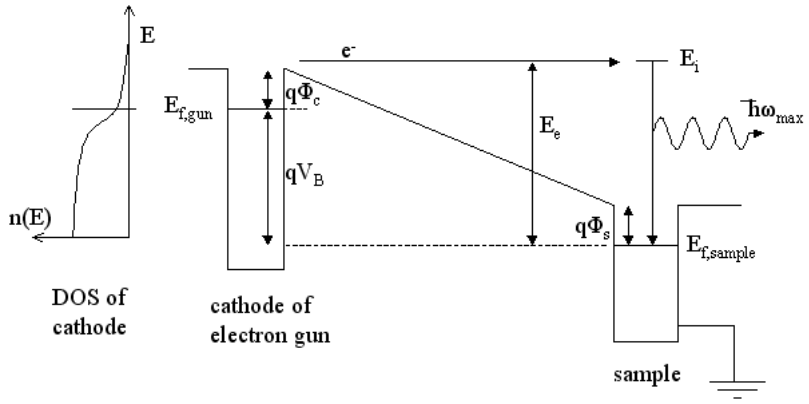

Figure 2.10: Energy diagram for the the electron gun and the sample in inverse photoemission.

2.5 Auger Electron Spectroscopy

Auger electron spectroscopy (AES) is used to identify the elements present at or near the surface of a sample and give a rough indication of their concentration. In this technique, a 3 keV electron beam is incident on a sample. Due to the high energy of the incident electrons, some of these electrons cause core level electrons in the solid to be ejected

from the sample, thus creating core holes. When an electron from a higher energy state decays to fill a core hole, it can do so radiatively, emitting a photon, or by Auger decay, where the energy gained in the decay is transferred to another electron, called the Auger electron. Fig. 2.11 shows the Auger process, where an Auger electron escapes the solid without inelastically scattering, and has a kinetic energy given by equation 2.13. The kinetic energy of Auger electrons emitted from an atom is characteristic of that atom and can be used to identify it.

$$E_k = (E_2 - E_1) + E_3 - q\Phi \tag{2.13}$$

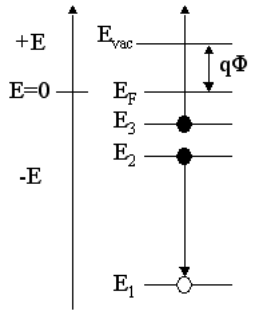

Figure 2.11: Schematic energy diagram of the Auger process.

In our AES measurements, an electron gun contained in a CMA produces the electron beam, and the CMA collects and energy analyzes the electrons emitted from the sample. As with UPS, electrons of a specific kinetic energy are selected by the voltages applied to the inner and outer cylinders. In AES, however, the CMA is not operated in retarding mode, so no retarding voltage is applied to the grid at the entrance aperture, and only the voltage of the outer cylinder is varied, while the inner cylinder is grounded. In this mode, a higher current of electrons reaches the detector, including a large amount of inelastically scattered electrons. To make the features from the Auger electrons stand out more strongly, a voltage modulation technique is employed to measure the first derivative of energy distribution of the emitted electrons (dN(E)/dE). For a CMA, this quantity is proportional first derivative of the collector current (I(E)).[52] The relationship between energy distribution of the electrons and the collector current is important to the voltage modulation technique, which is described below.

A small sinusoidal voltage (V=$V_\circ \sin(\omega t)$, known as the reference signal, is applied to the sample during the AES measurement. This affects the collector current, which can be written as a Taylor expansion with a small oscillating energy about E, as in equation 2.14. Since $V_\circ$ is small compared to the electron energy (E), all terms but the first two in this series can be neglected. By selecting the component of the collector current oscillating at a frequency of ω and measuring it, one measures a quantity proportional to the first derivative of the collector current. This quantity, in turn, is proportional to the first derivative of the energy distribution of emitted electrons.

$$I(E + qV_o \sin(\omega t)) = I(E) + qV_o \sin(\omega t)\frac{dI(E)}{dE} + (qV_o \sin(\omega t))^2 \frac{d^2 I(E)}{dE^2} + ... \quad (2.14)$$

In order to measure the component of the collector current oscillating at a frequency ω, a lock-in amplifier is used. The collector current and reference signals are input to the lock-in amplifier, where they are combined in a multiplier circuit, the output of which has an AC and a DC component.[57] The DC component, which is proportional to the coefficient of the $\sin(\omega t)$ term, is selected by the use of a low pass filter. Thus, a signal which is proportional to dN(E)/dE is selected and input to the computer, which records the AES spectrum that is reported as dN(E)/dE vs. E.

Fig. 2.12 shows two AES spectra taken to determine the purity of a Ru film deposited on Si. The lower spectrum in Fig. 2.12 is from a Si sample that was annealed to 1000°C. The strong feature at E=92 eV is the characteristic LVV Auger line in Si, where the letters LVV represent the electron shells of the core hole, the electron that filled it, and the Auger electron, respectively. The letter L stands for the n=2 shell, while V stands for the valence shell. The absence of the features of typical surface contaminants in this spectrum such as C (270 eV) and O (505 eV) shows that the Si surface was clean. The upper spectrum shows the AES spectrum from the same sample after 15 Å of Ru was deposited on it. This spectrum contains three features characteristic of the MVV Auger decays of Ru. The Si feature can also be seen in this spectrum, which has been attenuated by the metal overlayer. The attenuation of the Si feature by a factor of ∼0.5 due to the relatively thin Ru overlayer is an indication of the surface

sensitivity of AES. The absence of the C and O features in the spectrum from Ru/Si show that the Ru evaporation source was depositing clean Ru.

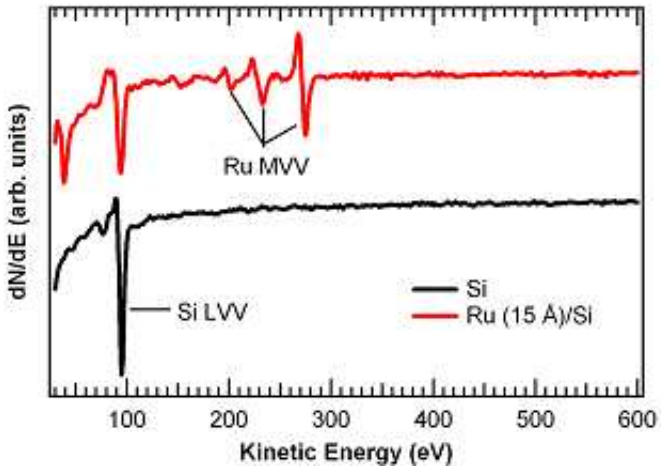

Figure 2.12: AES spectrum of Si and Ru(15 Å)/Si.

2.6 Low Energy Electron Diffraction

In this thesis, low energy electron diffraction (LEED) was used to determine the geometrical structures of rutile $TiO_2(110)$ and $ZnO(11\bar{2}0)$ surfaces. In LEED, A low energy (50-200 eV) electron beam with a well-defined energy is directed at a sample, and the elastically backscattered electrons are monitored by fluorescence from a phosphor-coated screen. If the sample has a well-ordered surface structure, an interference pattern will be visible on the screen. This pattern is an image of the reciprocal lattice of the crystal surface, from which the symmetry of the lattice structure of the crystal surface can be determined.

Fig. 2.13 shows a schematic diagram of a typical LEED apparatus. There are 4 concentric stainless steel mesh grids in front of the phosphor-coated screen. The first grid is grounded to keep the space between it and the sample free from an electric field. The second and third grids are held at a negative voltage slightly lower than the incident electron energy to repel electrons that have been inelastically backscattered. The fourth grid is also grounded to prevent the electric field from extending far beyond the phosphor coated screen that is located behind it. This screen is set to a positive potential of 4

kV to draw the electrons in once they are close to it. The screen will fluoresce at points where it is struck by electrons, i.e., where electrons interfere constructively.

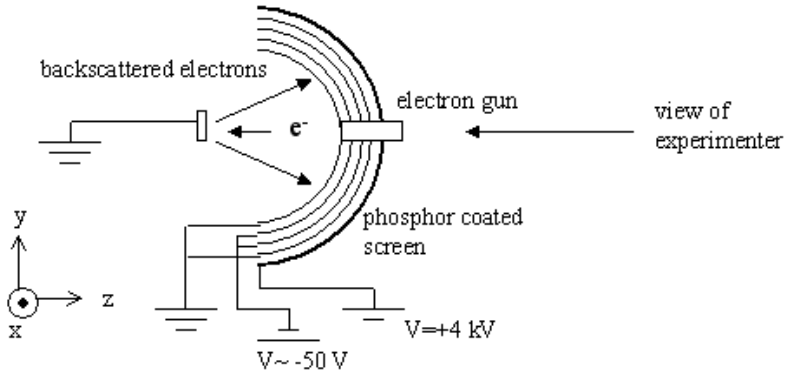

Figure 2.13: LEED apparatus schematic

The lattice and reciprocal lattice vectors of the crystal, $\vec{R}$ and $\vec{G}$ respectively, are related by equation 2.15. In a LEED experiment, the low energy of the incident electrons ensures that the majority of elastically scattered electrons reaching the screen originate from a depth of $\sim$10 Å or less.[49] This allows the lattice of the sample to be approximated as a two dimensional structure in the surface plane, which can be represented by two primitive lattice vectors. The primitive lattice vector perpendicular to the surface is considered to be infinite. For the two dimensional crystal, the reciprocal lattice is also represented by two primitive reciprocal lattice vectors, and the reciprocal lattice vector perpendicular to the plane is zero. Thus, the reciprocal lattice in three dimensions is an array of rods extending perpendicular to the surface at positions given by the in-plane reciprocal lattice vectors.

$$\vec{R} \cdot \vec{G} = 2\pi n \tag{2.15}$$

The condition for constructive interference in electron diffraction is when the incident and backscattered electron wave vectors, $\vec{k}$ and $\vec{k'}$, respectively, differ by a reciprocal lattice vector, as given in equation 2.16. In a LEED experiment with a normally incident electron beam, the condition becomes $k'_{\|} = G_{\|}$. This implies that the interference pattern visible on the LEED screen is an image of the reciprocal lattice structure

of the surface of the crystal. From this image, the symmetry and orientation of the lattice structure of the crystal surface structure can be deduced based on the relationship given in equation 2.15.

$$\vec{k} - \vec{k'} = \vec{G} \tag{2.16}$$

2.7 X-ray Absorption Spectroscopy

Another method to study the conduction band DOS is X-ray absorption spectroscopy (XAS). I will not report XAS measurements in this thesis, but I will discuss XAS results from the literature, so a brief description of the technique is in order. In XAS, the energy of a photon beam incident on a sample is varied over a range which is sufficient to excite electrons from a given core level into unoccupied states. When an electron absorbs a photon and makes a transition to an unoccupied state, it leaves behind a core hole. This core hole can be filled by the same electron, which is called direct recombination, or by an electron from another occupied state above the core hole. An example of the x-ray absorption process is shown in Fig. 2.14, where e_1^-, is the electron that absorbs the photon, e_2^- fills the core hole and e_3^- is an Auger electron that is emitted. As core holes are filled, electrons will be emitted from the sample, which can be collected and used as an indication of the number of transitions to unoccupied states at a given photon energy.

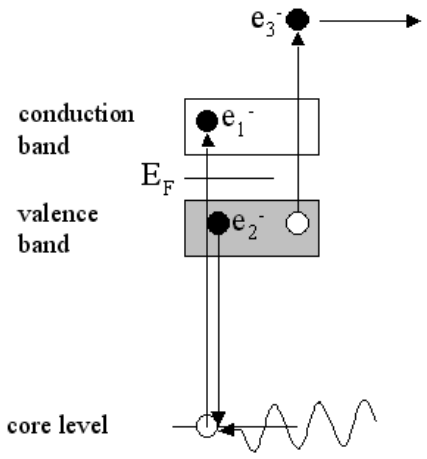

Figure 2.14: Schematic diagram of the x-ray absorption spectroscopy process.

XAS is a competitive technique with IPS in that both measure the unoccupied density of states of a sample, but XAS is prone to the disadvantage that a core hole is present each time an electron is promoted into an unoccupied state. This core hole lowers the energy of all of the electronic states of the atom, in some cases by more than 1 eV, from their ground state energies. The IPS process has the advantage that the electrons that it adds to the sample generally occupy non-localized states, so they can be drained to ground rapidly, and have a minimal effect on the energy of the unoccupied states of the solid.

An XAS measurement is particularly useful for determining the orbital character of unoccupied states. Each XAS spectrum is associated with a core level out of which the electrons are excited, referred to as the absorption edge. Dipole selection rules dictate the unoccupied states that an electron from a given absorption edge can make a transition to. For the purposes of this thesis, the only dipole selection rule that is relevant is the one that states that the initial state and the final state of the electron must have orbital quantum numbers that differ by ± 1 in order for a transition to occur.

Chapter 3

Oxide-Semiconductor Band Offsets

3.1 Introduction

The miniaturization of the MOSFET (metal-oxide-semiconductor field effect transistor) has required that the SiO_2 gate oxide be made thinner in order to increase capacitance per unit area of the device. The thickness of the SiO_2 layer is now as low as 10 Å in some MOSFETs, and it cannot be made thinner without allowing excessively high gate leakage current due to direct tunneling.[1] An alternative approach to thinning the SiO_2 layer is to use a higher dielectric constant (κ) material in place of SiO_2. A high-κ gate oxide could be thicker than an SiO_2 gate oxide, which would result in reduced gate leakage current due to direct tunneling. A MOSFET with a high-κ oxide could also have an increased capacitance per unit area by virtue of the high-κ value of the oxide. Efforts have been ongoing since the late 1990's to investigate high-κ oxides in order to identify those that can improve on the properties of the SiO_2 gate oxide in MOSFET's.

A major concern in the use of high-κ gate oxide is the magnitude of the conduction band offset (CBO) between the oxide and the semiconductor substrate. The band gaps of high-κ materials are smaller than that of SiO_2, and the band offsets between high-κ materials and Si are also smaller than those between SiO_2 and Si. It is critical to the success of a MOSFET using a high-κ gate oxide that the CBO between the high-κ oxide and the semiconductor be at least 1 eV, as set forth by the Semiconductor Industry Association, in order to inhibit the flow of electrons from the semiconductor to the metal, i.e., gate leakage current.[28] A less critical factor to the success of high-κ MOSFET, but still of interest, is the valence band offset (VBO) between the high-κ oxide and the semiconductor. This quantity is less critical because the VBO tends to be larger than the CBO, and because the mobility of holes is approximately half that

of electrons. In this chapter, I will describe how we experimentally determined the valence and conduction band offsets (VBO, CBO) between a high-κ oxide thin film and a semiconductor substrate. I will then present the VBO and CBO values that we measured for five oxide thin films on Si, and compare them to other measured values from the literature.

3.2 Growth of High-κ films on Si

The high-κ oxide films we measured were grown on Si substrates in other labs by either atomic layer deposition (ALD) or metal-organic chemical vapor deposition (MOCVD), and sent to us for characterization. Before an oxide film is grown on a Si substrate, the surface of the substrate is prepared in one of two ways: intentionally growing a thin (5-10 Å) SiO_2 film on the Si, or H-terminating the Si surface. Wet chemical techniques can be used to prepare either kind of surface. Another common way to prepare a thin oxide film is by thermal oxidation, where a clean Si surface is heated in a background pressure of oxygen gas.[58]

ALD is a method that can be used to grow flat, high quality high-κ oxide films of a well controlled thickness. It is a two step process, where the first step is exposure of a prepared Si substrate to a flux of gas molecules (precursor A), an example of which is $ZrCl_4$. These molecules bond to the surface in a self-limiting way, where no additional molecules will adsorb once all of the available bonding sites are occupied. Then the substrate is exposed to a flux of a different type of gas molecules (precursor B), an example of which is H_2O. The O from these molecules bonds with the Zr to form a layer of the ZrO_2, and the H reacts with Cl to form HCl molecules and other by-products, which are carried away in the flux. These two steps are repeated to grow a high-κ oxide film in a layer by layer fashion. A drawback of ALD is that the rate of film growth is slow, only 100-300 nm/hr.[58]

In MOCVD growth, a prepared Si substrate is exposed to a flux of precursor molecules at a specified temperature and pressure. An example of a metal-organic precursor that is used to grow HfO_2 films is Hf-tetra-tert-butoxide ($Hf(C_4H_9O)_4$). By

flowing this gas into a reaction chamber at a pressure of 1 mTorr and a temperature of 250-450°C, the gas will decompose and the constituents will form a HfO_2 film on the Si substrate.[59] Though the details of the chemical reactions involved MOCVD process are often poorly understood, MOCVD is a commonly used growth technique in industrial applications because its growth rate is high (1-1000 nm/min). Despite this advantage, MOCVD films have more impurities and are less uniform than those grown by ALD.[58]

3.3 Interfacial SiO_2 Oxide Layer

In the ALD and MOCVD growth of high-κ oxide films on Si substrates, there is almost always a thin ($\sim$10 Å) SiO_2 interfacial layer (IL) between the high-κ oxide and the Si. As stated earlier, this layer is often intentionally pre-grown. The reason for this is that an IL layer tends to form between the high-κ oxide layer and Si substrate during normal growth and/or processing conditions even if it is not pre-grown, so it is better to grow a high quality (low defect) SiO_2 layer intentionally than for a poor quality layer to form spontaneously.

In MOCVD growth, the elevated temperatures required to decompose the precursor inevitably result in the growth of an IL on an H-terminated Si substrate. In ALD, however, successful attempts to avoid the formation of an IL have been made by growing high-κ films on H-terminated Si surfaces. Chabal *et al.*, have grown HfO_2 films on Si without the formation of an IL, but this approach has not been widely adopted.[60] One problem is that the early stages of growth are especially slow. Another problem is that the films grown on an H-Si surface are less uniform and of a lesser electrical quality than those grown on pre-grown SiO_2 layers.[61] A third issue is that even if a film can be grown without an IL, an IL will form during the high temperature (1000°C) annealing of the film that must be performed in the processing of a MOSFET wafer. The purpose of this anneal is to activate the dopants in the source and drain electrodes. Thus, it is still common practice for high-κ oxide layers to be grown on intentionally grown SiO_2 layers on Si substrates.

The IL has both a desirable and an undesirable effect on the MOS stack. The desirable effect is that a low defect SiO_2-Si interface results in high carrier mobility in the channel of the Si. The undesirable effect is that the SiO_2 layer reduces the capacitance per unit area of the MOS stack as its capacitance per unit area adds reciprocally with that of the high-κ oxide. Alternatively stated, the IL increases the effect oxide thickness (*eot*) of the stack. The *eot* of a non-SiO_2 oxide is the thickness that an oxide composed solely of SiO_2 would have to be to give the same capacitance as the non-SiO_2 oxide. The *eot* of a high-κ dielectric is expressed in equation 3.1. In an MOS stack with a high-κ oxide layer and an SiO_2 IL, the total *eot* is the *eot* of the high-κ layer plus the thickness of the SiO_2 layer.

$$eot = (\frac{\kappa_{SiO2}}{\kappa_{high-\kappa}})t_{high-\kappa} \tag{3.1}$$

Despite the presence of the IL, the CBO between the high-κ oxide and the semiconductor is still an important quantity to measure. Fig. 3.1 shows a schematic band diagram of a HfO_2/SiO_2/p-Si system, where the high-κ oxide-semiconductor CBO and VBO are labeled $\Delta E_{c,os}$ and $\Delta E_{v,os}$, respectively. These quantities will be referred to as the oxide-semiconductor band offsets. Though the CBO between SiO_2 and Si is large, the SiO_2 layer is thin ($\sim$10 Å), and, therefore, allows a high level of leakage current by direct tunneling. The oxide-semiconductor CBO is needed as a barrier to this current. As high-κ MOS stacks are improved, the thickness of the IL will be reduced further to decrease the total *eot*, increasing the leakage current that the IL allows. Another factor to consider is that when the SiO_2 layer is less than 7 Å, the band gap does not attain its full bulk value, which will increase leakage current even further.[62] Thus, despite the presence of the IL layer, the oxide-semiconductor band offsets, particularly the CBO, are critical parameters to the success high-κ gate dielectric MOSFET's.

3.4 Comment on Sample Preparation

In the growth and characterization of high-κ oxide films on semiconductor substrates, the ideal situation is one where the films are grown and prepared in a vacuum chamber

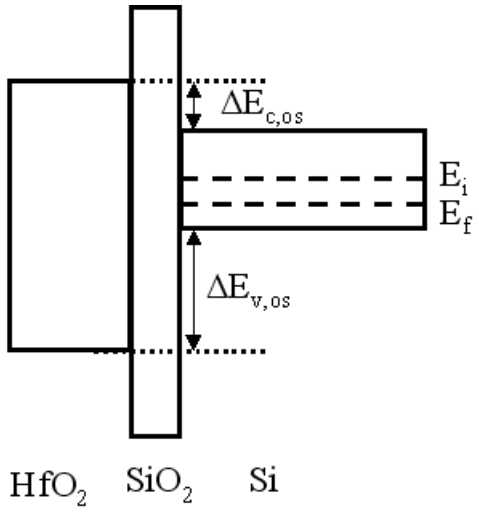

Figure 3.1: Band diagram of a HfO_2/SiO_2/p-Si stack.

in which all of the necessary measurements can be made. In practice, samples are often grown in one chamber and then measured in another, between which times they are exposed to atmospheric contamination. For surface science measurement techniques, it is common practice to anneal these samples in vacuum to remove the atmospheric contamination from the surface in order to measure a clean surface.

It is also often true that samples from the same wafer are measured in different vacuum chambers that house different measurement techniques, and the measurements are combined in the characterization of the film. Care must be taken in this case to see that the samples are prepared in the same way in each chamber, as the properties of high-κ oxide films have been shown to depend on sample preparation.[43, 44] Even sample preparations that are nominally the same may differ between two vacuum chambers due to different heating methods, imprecise temperature measurement and different background pressures and gases. In general, the best characterization system is one that combines as many techniques as possible in one chamber so that different measurements can be made on a sample with a given preparation, so they can be appropriately combined.

3.5 Experimental Methods

The method we used to measure the oxide-semiconductor band offsets is based on UV photoemission spectroscopy (UPS) and inverse photoemission spectroscopy (IPS) measurements in the same vacuum chamber. This combination of techniques gives a direct measurement of the occupied and unoccupied density of states (DOS) of the oxide layer with respect to the Fermi level, from which the valance band maximum (VBM) and conduction band minimum (CBM) of the oxide can be obtained. We performed UPS using a He discharge lamp as a photon source and a cylindrical mirror analyzer to collect and energy analyze the photoelectrons. IPS was performed with a Stoffel-Johnson style electron gun and a grating spectrometer for analyzing the emitted photons. The details of these measurements are described more fully in Chapter 2, Sections 3 and 4. Unless otherwise noted, the photon energy for the UPS measurements was 40.8 eV (He II radiation) and the electron energy for the IPS measurements was 20.3 eV. We also measured the occupied electronic structure of samples in a vacuum chamber at beamline U5 at the National Synchrotron Light Source (NSLS) with soft X-ray photoemission spectroscopy (SXPS). In these measurements, a hemispherical mirror analyzer was used to collect and analyze the photoelectrons. The photon energy for the SXPS measurements was 150 eV. It is important to note that the sample preparation conditions used in the chamber at the NSLS were matched as closely as possible to those used in the chamber at Rutgers.

3.6 Preliminary Considerations

As mentioned earlier, all of the thin film oxide/Si samples that we measured were grown in other labs and sent to us for characterization. Medium energy ion scattering (MEIS) was performed on one sample from each wafer we received to confirm the stated stoichiometry and thickness of the films. In order to remove atmospheric contamination from samples before UPS, IPS and SXPS measurements, we annealed the samples in vacuum at 500-600°C for 3-5 min. The effect of the vacuum anneal was investigated with MEIS, Auger electron spectroscopy (AES) and SXPS. The MEIS measurements

showed that the annealing had the effect of changing the high-κ films from slightly oxygen rich to stoichiometric. An AES spectrum of an annealed HfO_2/Si sample, shown in Fig.3.2(a), demonstrates that there is only a small amount of C on the surface after annealing. It should be noted that in identifying samples, the IL is omitted for the sake of simplicity, although it is present between the HfO_2 and Si in the samples. The effect of the annealing was also monitored in SXPS. Fig. 3.2(b) shows that the SXPS spectrum of HfO_2/Si in the as loaded and annealed conditions are very nearly the same.

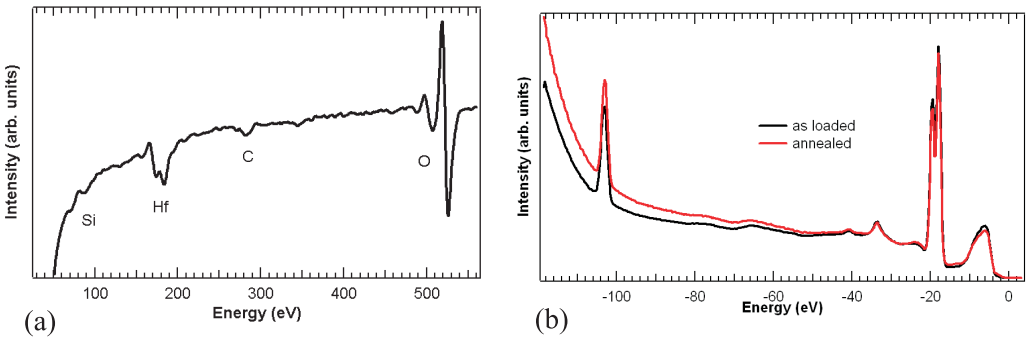

Figure 3.2: (a)AES spectrum of annealed HfO_2/Si. (b)SXPS spectra of as loaded and annealed HfO_2/Si.

An interesting effect that we observed in the preparation of HfO_2/Si samples should also be noted here. Performing IPS on a sample that was not annealed in vacuum had the effect of introducing spectral intensity in the band gap region of HfO_2, as observed in the UPS and IPS spectra. Fig. 3.3 shows UPS and IPS spectra from an HfO_2/Si sample that was exposed to the electron beam for 10 minutes on a single spot, then annealed in vacuum and measured with UPS and IPS. The UPS and IPS spectra from the exposed spot are shown in red, and the spectra from a different spot on the sample, not exposed to the electron beam before annealing, are shown in black.

The band gap region of the HfO_2 is defined by the sharp increase in the UPS spectra at $\sim$-3 eV and the sharp increase in the IPS spectra at $\sim$2 eV. Within this region, it can be seen that spectra from the spot exposed to the electron beam before annealing have greater intensity in the HfO_2 band gap region. This intensity suggests the presence of defect states in the oxide film, which are caused by the electron beam stimulating a

reaction between the atmospheric contaminants and the HfO_2 film. This interpretation of the intensity in the band gap region is supported by theoretical calculations that show that defect states of HfO_2 occur in the band gap region.[63] Further annealing of the sample was shown not to remove the additional intensity from the band gap region.

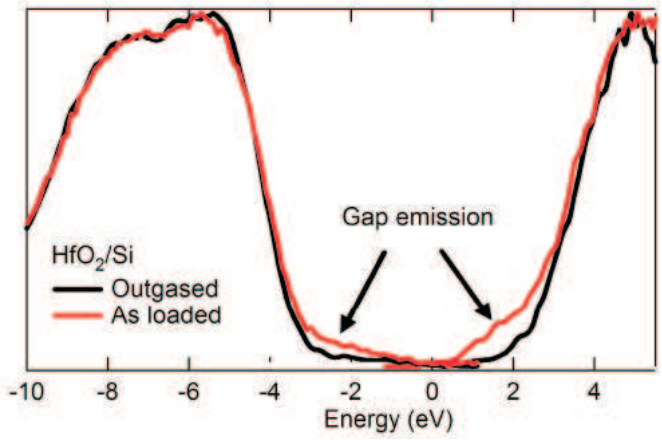

Figure 3.3: UPS and IPS from HfO_2/Si, where the red spectra were taken on a spot that was exposed to the electron beam before annealing and the black spectra were taken on a spot that was annealed before being exposed to the electron beam.

Sample charging is always a concern when performing electron spectroscopy on an oxide film. When an electron is added to the sample in IPS, it must be drained quickly so that the electronic states of the sample will not be shifted upward by its electrostatic potential. Charging can also occur in UPS if the positively charged hole is not drained quickly to ground, causing the spectral features to occur lower in energy than they would if the sample was not charged. We attempted to eliminate charging by measuring samples with thin oxide films (t_{ox} $\leq$30 Å) and high substrate conductivity, and by optimizing the electrical contact to the sample.

In cases where we observed charging in IPS, a number of short spectra (t$\sim$1 min) were taken, which were interspersed with short anneals to discharge the sample. In UPS, the effect of charging was determined by taking short spectra of the valence band edge region of a uncharged sample, and continuing to take spectra over a period of time until the energy of valence band maximum was constant. These spectra enabled us to measure an energy shift due to charging. The spectrum of the entire valence band of a sample that was observed to charge was shifted upwards in energy by the measured

energy shift due to charging to correct for this effect.

3.7 HfO_2-Si Band Offsets

Fig. 3.4 shows a UPS, SXPS and an IPS spectrum from a HfO_2(15 Å)/Si sample that are displayed on the same graph. The energy scales of these measurements have been joined at the Fermi level. The zero of the combined energy scale has been set, however, to the midgap level of the Si at the interface between Si and the IL. The determination of this level will be discussed more below. It should also be noted that the UPS, SXPS and IPS spectra are normalized so that the peak intensity of each spectrum is equal. As is characteristic of a transition metal oxide, the occupied density of states (DOS) of HfO_2 is composed mostly of O $2p$ electrons, and the unoccupied DOS is dominated by Hf $5d$ states that are mixed with O $2p$ states.

In order to find the energy of the VBM of HfO_2, a method of linear fitting is used. A linear fit is performed on both the low binding energy valence band edge and the emission in the band gap region of the UPS spectrum, as shown in Fig. 3.4. The energy where the two linear fits intersect is the HfO_2 VBM. We find that the HfO_2 VBM from the UPS spectrum is -3.3 eV. By the same method, the VBM from the SXPS spectrum is -3.2 eV. The HfO_2 CBM is found by applying the same method of linear fitting to the low energy edge of the conduction band and the emission in the band gap region of the IPS spectrum, as shown in Fig. 3.4, which gives a CBM value of 2.4 eV.

In order to estimate the uncertainty of the VBM and CBM values determined by the linear fitting procedure, we have obtained alternative values for the VBM and CBM. These values were obtained by adding and/or subtracting 2 standard deviations (2σ) from the slope and intercept of the band edge fits in order to maximize and minimize the VBM and CBM values. The VBM and CBM values manipulated in this way were shifted from the original values by less than 0.1 eV. On this basis, we estimate that the uncertainty in the VBM and CBM values to be $\pm$ 0.1. Thus, the VBM values obtained from the UPS and SXPS measurements agree within the range of the experimental error. The value of the HfO_2 band gap is found by adding the absolute value of the VBM

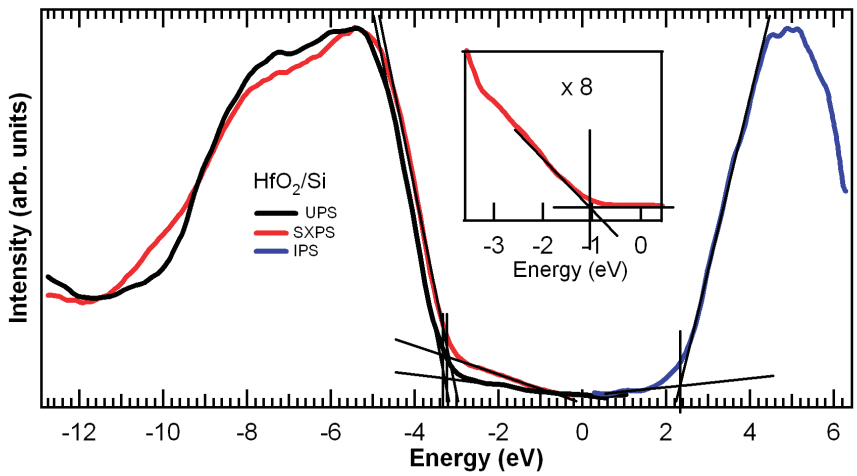

Figure 3.4: UPS, SXPS and IPS spectra from HfO_2/Si, where E=0 is the midgap of the Si at the interface. The inset shows SXPS spectrum where the intensity scale is increased by a factor of 8, and E=0 corresponds to the Fermi level.

from the UPS spectrum with the CBM from the IPS spectrum, as these measurements were taken on the same sample in the same chamber. We find an HfO_2 band gap of 5.7 eV with an uncertainty of $\pm$0.2 eV.

Using the accepted value of 1.12 eV for the band gap of Si, the Si VBM and CBM are 0.56 eV below and above the Si midgap level, respectively. As the energy resolution of our measurements is 0.1 eV, we round these values so that the Si VBM is -0.6 eV and the CBM is 0.5 eV. Thus, the VBO and CBO between HfO_2 and Si are 2.7 eV and 1.9 eV, respectively, each with an uncertainty of $\pm$0.2 eV.

The energy of the Si midgap level is found from the determination of the Si VBM in the SXPS spectrum from HfO_2/Si. In order to use this spectrum to find the Si VBM, it is necessary to establish that the intensity in the band gap region is due to the Si substrate. The following two arguments support this assertion. The first is that the SXPS spectrum has greater intensity in the HfO_2 band gap region does the UPS spectrum, as shown in Fig. 3.4. This observation can be explained by assigning the emission in the band gap region to the underlying Si, and using the differences in inelastic mean free path (IMFP) for the Si valence band photoelectrons in the SXPS and UPS measurements to explain the difference in intensity.

As discussed in Chapter 2, Section 3, the IMFP of an electron is the average distance

the electron will travel in a solid before being inelastically scattered. Fig. 3.5 shows the electron IMFP as a function of kinetic energy. In this curve, it can be seen that the kinetic energy corresponding to the shortest IMFP is 60 eV. At this energy, the IMFP of an electron in a solid is ∼10 Å, while both lower and higher kinetic energies have longer IMFP's. The kinetic energy range of the Si valence band photoelectrons in the UPS measurement is 30-35 eV, while these electrons have energies of 133-138 eV in the SXPS measurement. As the Si valence band photoelectrons in the UPS measurement are close in energy to the minimum IMFP, while those in the SXPS measurement are in a higher energy range where the IMFP is longer, the Si valence band photoelectrons contribute more strongly in the SXPS measurement.

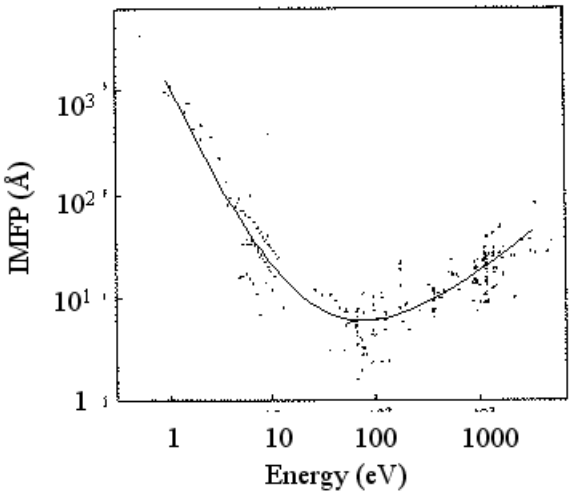

Figure 3.5: Electron Inelastic Mean Free Path (IMFP) vs. kinetic energy.[2]

The second argument for attributing the emission in the band gap region of the SXPS spectra from HfO_2/Si to the Si substrate can be made through an analysis of SXPS core level and valence band spectra from an SiO_2(20 Å)/Si sample. The SiO_2/Si sample had a smaller thickness (20 Å) than the total oxide thickness than that of the HfO_2/Si sample (25 Å), allowing the substrate Si to contribute more strongly to the SXPS spectra. Using a literature value for the energy difference between the Si $2p_{3/2}$ core level and the Si VBM, we can show that the emission in the band gap region of the SXPS spectrum from SiO_2/Si is accurately attributed to the Si substrate.

Fig. 3.6(a) shows the SXPS spectrum of the valence band region from SiO_2/Si,

where E=0 corresponds to the Fermi level of the sample. The spectrum is plotted twice, once where the SiO_2 valence band can be seen, and a second time where the intensity scale has been increased by a factor of 10 to highlight the emission in the band gap region. By performing a linear fit to the edge of the emission in the band gap region and extrapolating to zero emission, the edge of this intensity is found to be -0.7 eV. In Fig. 3.6(b), the Si $2p$ core level spectrum is also plotted twice. In one spectrum, the Si $2p$ core level from SiO_2 and is shown. This feature is centered at -103.7 eV, which is characteristic of Si in the 4+ oxidation state.[64] A re-scaled version of the SXPS spectrum is also shown, where the Si $2p_{3/2}$ core level from elemental Si (oxidation state=0) can be seen, centered at -99.4 eV. We note that the energy difference between the edge of the emission band gap region and the Si $2p_{3/2}$ core level is 98.7 eV. This is the same as the energy difference between these spectral features reported in the literature for elemental Si, confirming that the emission in the SiO_2 band gap region is due to substrate Si.[65]

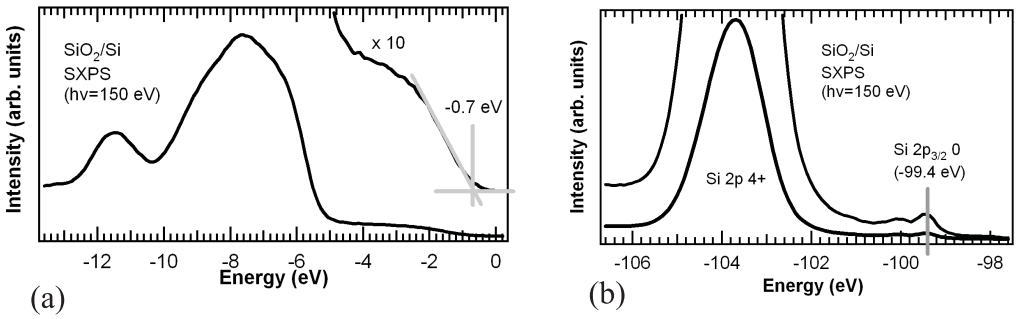

Figure 3.6: SXPS spectra of the (a)valence band (b)Si $2p$ core level regions from SiO_2/Si.

Based on these two arguments, we attribute the emission in the band gap region in the SXPS spectra from all of our high-κ oxide/Si samples to Si. We were not able to confirm this assertion in the same way that it was confirmed for SiO_2/Si, however, as the Si $2p_{3/2}$ core level was not visible in the SXPS spectra from the high-κ oxide/Si samples.

The process of determining the Si VBM for the HfO_2/Si system is shown in the inset of Fig. 3.4. In the inset, the SXPS spectrum from HfO_2/Si is plotted on an energy scale

where E=0 corresponds to the Fermi level. The intensity scale is has been increased by a factor of 5 to show the Si valence band more clearly. By fitting the low binding energy edge of the Si valence band with a straight line and extrapolating to zero emission, we find that the Si VBM is -1.0 eV. Once this quantity is known, the Si CBM and midgap level can be found using the accepted value of 1.1 eV for the Si band gap.

It is important to note the difference between the values of the Si VBM and CBM at the SiO_2/Si interface of HfO_2/Si and those in the bulk of the Si substrate. As discussed above, the Si VBM was determined from the SXPS measurement from HfO_2/Si. Despite being more bulk sensitive than the UPS measurement in the valence band region, the SXPS measurement is still considered surface sensitive. Owing to the surface sensitivity of the SXPS measurement, the Si valence band photoelectrons originate from only the top 5-10 Å of the Si, which is the region near the SiO_2/Si interface.

The bulk Si VBM and CBM can be determined from the value of the conductivity of the Si substrate. For the HfO_2(15 Å)/SiO_2/Si sample measured above, the Si was p-doped with a conductivity of 1-2 Ωcm^{-1}. This gives a VBM of -0.2 eV and a CBM of 0.9 eV by the equations discussed in Chapter 1, Section 2. The difference between Si VBM and CBM values at the interface and those in the bulk indicates that there is a downward band bending in the Si of 0.8 eV. In an Si sample with a typical doping density ($\sim 1 \times 10^{-15} (cm^{-3})$) such as we used, this band bending place over a distance on the order of thousands of Å from the SiO_2/Si interface. The band diagram in Fig. 3.7 shows the downward band bending that we observe in HfO_2/Si. Possible explanations for the Si band bending will be discussed later.

Table 3.1 shows the values we measured for the HfO_2 band gap and the HfO_2-Si VBO and CBO along with several measurements of these quantities from the literature. A first look at this table shows that the values we measured are in good general agreement with the literature values. The value we measured for the CBO (1.9 eV) is one of the higher ones reported, along with a value of 1.91 eV determined by a combination of XPS and core photoelectron energy loss spectroscopy (energy loss),[66] and a value of 2.0 eV, determined by internal photoemission (IntPE).[43] Sayan *et al.* used a method similar to ours, combining SXPS and IPS, although these measurements were not performed

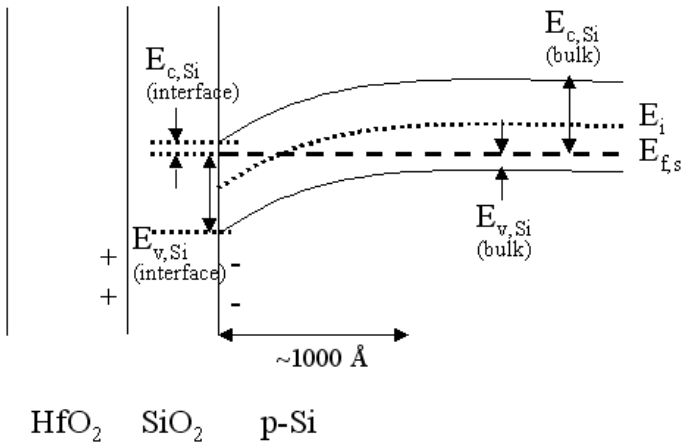

Figure 3.7: Band diagram of HfO_2(15 Å)/Si showing how the Si VBM and CBM differ in the bulk and at the interface.

in the same UHV chamber.[67] They found a CBO that is lower than ours by ∼0.3 eV.

Toyoda *et al.* used a combination of XPS and x-ray absorption spectroscopy (XAS), the latter of which is prone to error on the CBO value due to the lowering of the conduction band states resulting from the presence of the core hole.[68] This explains why the CBO and band gap values from Toyoda *et al.* are the lowest we found in the literature. The VBO value measured by Toyoda *et al.*, however, agrees well with our value and the other literature values. Another of the lower CBO values was obtained from a current-voltage (I-V) measurement, where a CBO value is determined by fitting a measured I-V curve with a model expression for a single leakage current mechanism.[69] Spectroscopic ellipsometry (SE) was used to measure the band gap of HfO_2. Nguyen *et al.* measured a value that was lower than ours by ∼0.1 eV, [70] and Mondreanu *et al.* reported several values, some of which agree with ours and some are higher by ∼0.3 eV.[44]

3.8 Predicted HfO_2-Si Band Offsets

A number of calculations of the HfO_2/Si band offsets have been performed, which make use of two primary methods.[20, 74, 75, 33] As discussed in Chapter 1, Section 6, the interface gap state (IGS) model can be used to calculate an oxide-semiconductor band offset, though the validity of this measurement is compromised by the lack of a

method	E_g (eV)	VBO (eV)	CBO (eV)
this work	5.7	2.7	1.9
XPS, energy loss[20]	5.7	3.10	1.48
XPS, energy loss[66]	5.25	2.22	1.91
XPS, IPS[67]	5.86	3.28	1.46
XAS, XPS[68]	5.1	3.0	1.0
UPS[71]	—	2.75	—
IntPE[43]	5.6,5.9	2.5	2.0
XAS[72]	6.0	—	$\geq$1.2
EELS[73]	5.8	—	—
SE[70]	5.56	—	—
SE[44]	5.66-5.95	—	—
I-V[69]	—	—	1.1
IGS[74]	6.0	3.4	1.5
RP[20]	5.7	2.69-3.04	1.54-1.89
RP[33]	5.8	2.9	1.8

Table 3.1: Measured values for HfO_2 band gap and HfO_2-Si VBO and CBO.

chemically abrupt high-κ oxide-Si interface. Robertson and Demkov *et al.* have used this method and obtain CBO values for HfO_2-Si of 1.5 eV and 1.4 eV, respectively.[74, 33]

The other method used to calculate the oxide/Si band offsets is known as the reference potential (RP) method. In this method, the average electrostatic potential inside each material is calculated, as well as the difference between the average potentials of the two materials. Then, from the energy difference between the VBM and the average potential for each material, the VBO can be found. Once the VBO between the materials is calculated, values for the HfO_2 and Si band gaps can be used to calculate the CBO.[76] This method has been used by Puthenkovilakam *et al.* to calculate values between 1.5-1.9 eV for the HfO_2-Si CBO. The CBO was found to increase as a function of O coordination at the interface.[20] It should be noted, however, that the SiO_2 interfacial layer was not taken into account in these calculations. Demkov *et al.* have also used the RP method, from which they found a CBO value of 1.8 eV.[33] This calculation, which includes an SiO_2 interfacial layer, agrees best with the value we measured for the HfO_2-Si CBO.

3.9 $Hf_{0.7}Si_{0.3}O_2$-Si Band Offsets

Fig. 3.8 shows a UPS, an SXPS and an IPS spectrum from $Hf_{0.7}Si_{0.3}O_2$(20 Å)/Si. In this graph, and all subsequent graphs showing the UPS, SXPS and IPS spectra, the zero of the energy scale corresponds to the midgap energy of the Si at the interface. By the method of linear fitting, the VBM and CBM of $Hf_{0.7}Si_{0.3}O_2$ are found to be -3.4 eV and 2.6 eV from the UPS and IPS spectra, respectively, giving a band gap of 6.0 eV. The VBM from the SXPS spectrum is -3.1 eV, which is lower in binding energy than the VBM found from the UPS spectrum, and outside the range of experimental error. The discrepancy between the UPS and SXPS VBM values will be discussed below. As the Si VBM is -0.6 eV and the CBM is 0.5 eV, the VBO and CBO between $Hf_{0.7}Si_{0.3}O_2$ and Si are 2.8 eV and 2.1 eV, respectively.

As was the case for HfO_2/Si, and will be the case for all subsequent oxide/Si systems discussed, the Si VBM with respect to the Fermi level was found from the SXPS spectrum plotted on a scale where E=0 corresponds to the Fermi level. This spectrum, shown in the inset of Fig. 3.8, was fit with a straight line to find the Si VBM at the interface, which was -1.1 eV. The bulk Si VBM, calculated from using the bulk Si resistivity of 1-2 Ωcm^{-1}, was -0.2 eV. Thus, the band bending in the Si of $Hf_{0.7}Si_{0.3}O_2$/Si was downward by 0.9 eV.

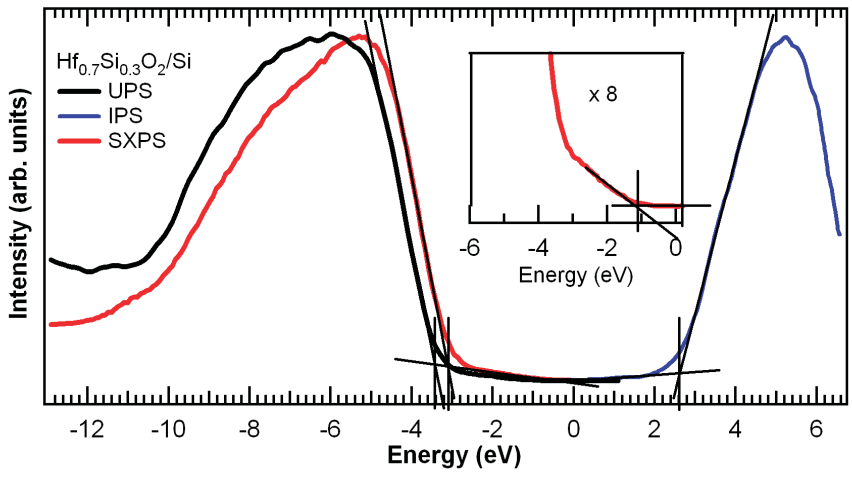

Figure 3.8: UPS, SXPS and IPS spectra from $Hf_{0.7}Si_{0.3}O_2$/Si.

We did not find experimental values for $Hf_xSi_{1-x}O_2$-Si band offsets in the literature.

One value for the band gap of an $Hf_{0.7}Si_{0.3}O_2$ film on Si was reported, where a value of 6.2 eV was determined by spectroscopic ellipsometry, in good agreement with the value we measured (6.0 eV).[77] Puthenkovilakam *et al.* used the RP method to calculate a VBO of 2.8 eV for the $HfSiO_4$/Si system. They also use a band gap of 6.0 eV, which was reported by Robertson[74], to determine a CBO of 2.1 eV.[20] These values agree well with our measured values for $Hf_{0.7}Si_{0.3}O_2$/Si, though their validity is limited by the neglect of the SiO_2 interfacial layer in the calculation.

A previous study by Lucovsky *et al.* of the $Zr_xSi_{1-x}O_2$/Si system is also relevant to our measurements of the $Hf_{0.7}Si_{0.3}O_2$/Si and HfO_2/Si band offsets.[19] The analysis of zirconium silicate is relevant to hafnium silicate because Zr and Hf are chemically very similar, Zr being directly above Hf on the periodic table. This study showed that increasing the SiO_2 concentration in the zirconium silicate alloy in $Zr_xSi_{1-x}O_2$/Si samples linearly increased the oxide-semiconductor VBO, but left the CBO unchanged until the ZrO_2 concentration was low as x=0.1. The authors attributed the change in the VBO to changes in the bonding environment of O $2p$ states that compose the valence band. The constancy of the CBO was attributed to the localized nature of the the Zr $4d$ states in the conduction band, which are not strongly affected by the presence of Si.

We observe a small increase in VBO (0.1 eV) and a slightly larger increase in CBO (0.2 eV) between HfO_2/Si and $Hf_{0.7}Si_{0.3}O_2$/Si. Thus, our results differ from those of Lucovsky *et al.* in that we observe an increase in the CBO with increasing SiO_2 composition where they find none, and we observe a smaller increase in the VBO with increasing SiO_2 composition than they find.

3.10 ZrO_2-Si Band Offsets

The UPS, SXPS, and IPS spectra for ZrO_2(25 Å)/Si are shown in Fig. 3.9. From the UPS and IPS measurements, the VBM and CBM are found to be -3.3 eV and 2.2 eV, respectively, relative to the Si midgap level at the interface. Thus, we measure a band gap of 5.5 eV for ZrO_2, and a VBO and CBO of 2.7 eV and 1.7 eV, respectively, between

ZrO_2 and Si. The VBM from the SXPS spectrum is -3.1 eV, which is again lower in binding energy than the UPS value, but within the range of experimental error. As the Si resistivity is 0.02 Ωcm^{-1}, the bulk Si VBM is -0.1 eV. This differs from measured Si VBM at the interface, which is found to be -0.9 eV from the SXPS spectrum shown in the inset of Fig. 3.9. The comparison of these two values for the Si VBM indicates that the band bending in the Si of ZrO_2/Si is downward by 0.8 eV.

Table 3.2 shows the values we measured for the ZrO_2 band gap and ZrO_2-Si band offsets, along with values reported in the literature. The values we measured fall within the scatter of the values reported in the literature, though there is less consensus in the literature as to the band offsets for ZrO_2-Si than for HfO_2-Si. The CBO value we measured (1.7 eV) is in between two higher values (2.0 eV) and five lower values (0.88 - 1.2 eV) reported in the literature. The calculated CBO values of Puthenkovilakam *et al.* (0.64 - 1.02 eV) agree better with the lower CBO values, and differ from the CBO we measured by 0.7 eV or more.[78]

method	E_g(eV)	VBO(eV)	CBO(eV)
this work	5.5	2.7	1.7
XPS, energy loss[78]	5.65	3.65	0.88
XPS, energy loss[79]	5.50	3.35	1.03
XPS, energy loss[17]	5.6	2.5	2.0
XPS, UPS[80]	5.7	3.4	1.2
UPS[71]	—	3.0	—
SXPS, IPS[81]	5.68	3.40	1.16
IntPE[18]	5.4	2.3	2.0
EELS[73]	5.0	—	—
XAS[72]	6.0	—	$\geq$1.2
I-V[82]	—	—	1.0
RP[78]	5.65	3.51-3.89	0.64-1.02

Table 3.2: Measured values for ZrO_2 band gap and ZrO_2-Si VBO and CBO.

A possible explanation for the pattern of VBM values that are lower in binding energy in the UPS spectrum than in the SXPS spectrum is the difference in photon flux between the two measurements. The helium discharge lamp at Rutgers gave a sample current of $\sim$1 nA, whereas the sample current in the SXPS measurement at the NSLS was $\sim$10 nA, indicating a higher photon flux. The high photon flux and the small spot size at the NSLS may have resulted in local heating of the sample,

providing a more conductive pathway through which holes could drain to the substrate and to ground. The samples measured at Rutgers, on the other hand, might have had a low level of charging that was not alleviated by local heating of the sample. This explanation is consistent with the observation that the greatest different between the UPS and SXPS VBM values occurs for the samples with the greatest total oxide thicknesses ($Hf_{0.7}Si_{0.3}O_2$ (t_t=30 Å), ZrO_2 (t_t=35 Å), Al_2O_3 (t_t=35 Å)), which are the most likely to charge during measurement.

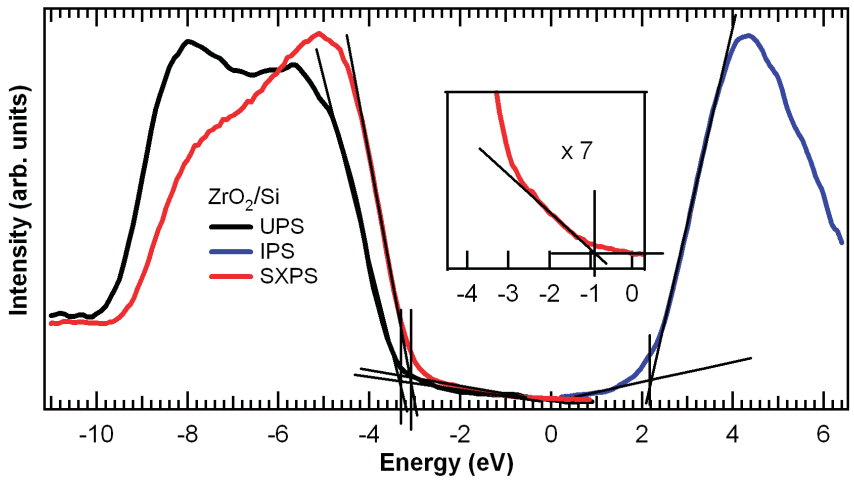

Figure 3.9: UPS, SXPS and IPS spectra from ZrO_2/Si.

3.11 Al_2O_3-Si and SiO_2-Si Band Offsets

We also measured the band offsets of Al_2O_3 and SiO_2 with Si. These oxides have relatively low dielectric constants, but they have been widely studied and there are a number of published band offset values for them, to which we can compare our results. Fig. 3.10 shows the UPS, SXPS, and IPS spectra from Al_2O_3(25 Å)/Si. For this sample and for SiO_2/Si, the IPS spectra were taken at an incident electron energy of 23.3 eV. The shape of the IPS spectrum is interesting in that the conduction band edge rises gradually from the band gap region. This is different than the conduction band shape of the transition metal oxides (HfO_2, $Hf_{0.7}Si_{0.3}O_2$, ZrO_2) shown above, where the conduction band edge rises sharply due to the strong d band features in the density of states. The conduction band of Al_2O_3, on the other hand, is composed of strongly

dispersing Al 3s and 3p states mixed with O states, typical of a non-transition metal, that do not constitute strong features in the density of states.[83]

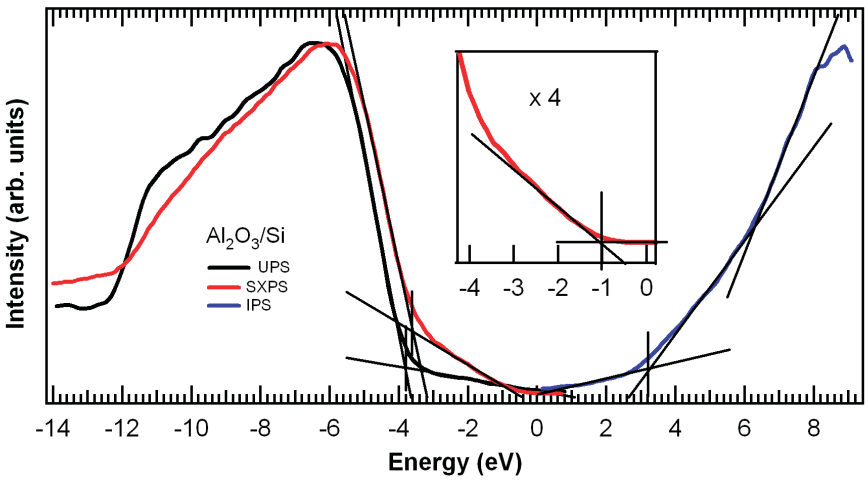

Figure 3.10: UPS, SXPS and IPS spectra from Al_2O_3/Si.

As can be seen in the IPS spectrum in Fig. 3.10, the shape of the Al_2O_3 conduction band requires two lines to fit the two regions of the IPS spectrum, one for the gradually sloping region between 3-6 eV, and another for the more steeply sloping region between 6-9 eV. The CBM is the energy at which the fit to the lower energy region of the conduction band crosses the fit to the emission in the band gap, which is 3.2 eV. The VBM determined from the UPS and SXPS spectra are -3.8 and -3.6 eV, respectively, continuing the trend of the SXPS VBM values that are lower in binding energy. From the VBM and CBM values with respect to the midgap level of the Si at the interface, we find the band gap of Al_2O_3 to be 7.0 eV, and the Al_2O_3-Si VBO and CBO to be 3.2 eV and 2.7 eV, respectively. As shown in the inset of Fig. 3.10, the VBM of the Si at the interface relative to the Fermi level is -1.0 eV. The bulk Si VBM, however, is -0.1 eV, as determined using the resistivity of 0.01 Ωcm^{-1}. In keeping with the other p-Si substrates, the band bending is downward by 0.9 eV.

Table 3.3 shows the values we measured for the Al_2O_3 band gap and band offsets with Si, as well as other values for these quantities from the literature. The value we measured for the band gap agrees well with the larger of the reported values (6.7 eV, 6.95 eV), but differs from the smaller values by as much as 0.8 eV. It is interesting

method	E_g(eV)	VBO(eV)	CBO(eV)
this work	7.0	3.2	2.7
XPS, energy loss[79]	6.95	3.75	2.08
XPS, plasmon loss[66]	6.52	3.03	2.37
XPS, plasmon loss[17]	6.7	2.9	2.7
IntPE[18]	6.2	2.95	2.15
SE[70]	6.26	—	—
BEEM[84]	—	—	2.8

Table 3.3: Measured values for Al_2O_3 band gap and Al_2O_3-Si VBO and CBO.

to note that a band gap of 8.8 eV was measured for a bulk α-Al_2O_3 crystal, which is significantly larger than the measured band gaps of thin, amorphous Al_2O_3 layers listed in Table 3.3.[85] The band gaps for the other high-κ oxides we studied were not as strongly dependent on thickness and crystal phase as Al_2O_3.[74] The value we measured for the Al_2O_3-Si VBO falls near the center of the range of literature values, while that for the CBO is one of the higher values.

The UPS, SXPS and IPS spectra from SiO_2/Si, where the IPS spectrum was taken at an incident electron energy of 23.3 eV, are shown in Fig. 3.11. The shape of the IPS spectrum from SiO_2/Si is similar to that from Al_2O_3/Si in that it rises gradually from the band gap region, which reflects the strongly dispersing Si $3s$ and $3p$ character of the low energy conduction band states. Previous IPS measurements of SiO_2 show a similar conduction band shape.[65, 86]

Using two lines to fit the SiO_2 IPS spectrum and one to fit the emission in the energy region of the band gap, we find a CBM of 3.8 eV. The VBM of the UPS spectrum of SiO_2 is -5.1 eV, which agrees well with the VBM from the SPXS spectrum. Thus, the band gap we measure for SiO_2 is 8.9 eV, and the VBO and CBO between SiO_2 and Si are 4.5 eV and 3.3 eV, respectively. As shown in the inset of Fig. 3.11, the Si VBM from the SXPS spectrum is found to be -0.7 eV with respect to the Fermi level. The bulk Si, which is n-type and has a resistivity of 70 Ωcm^{-1}, has a VBM of -0.8 eV. Thus, the band bending in the Si substrate of the SiO_2/Si sample upward by 0.1 eV. The difference in the band bending behavior between the SiO_2/Si and high-κ oxide/Si samples is interesting to note, and will be discussed in a subsequent section. Table 3.4 shows that the values we measured for the SiO_2 band gap and the SiO_2-Si band offsets

are in good agreement with the literature values, among which there is considerable agreement.

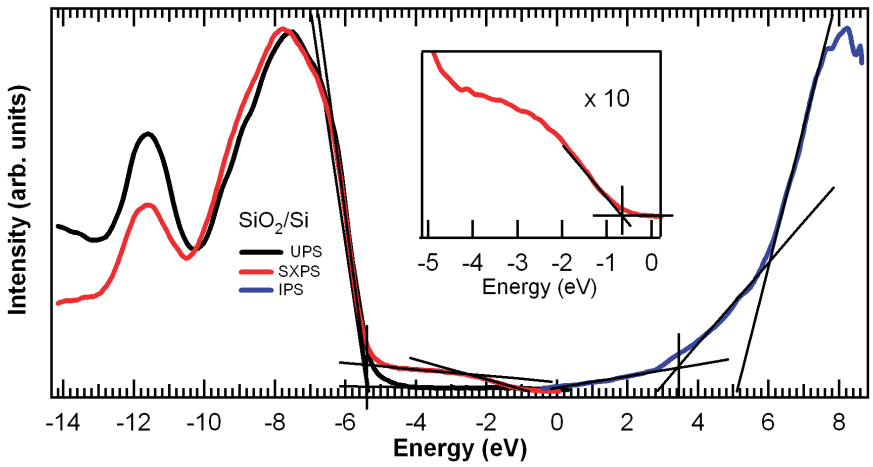

Figure 3.11: UPS, SXPS and IPS spectra of SiO_2/Si.

group	E_g(eV)	VBO(eV)	CBO(eV)
this work	8.9	4.55	3.25
XPS, plasmon loss[79]	8.95	4.49	3.34
XPS, UPS[80]	9.0	4.4	3.5
IntPE[18]	—	—	3.15
XPS[87]	—	4.35	—
XPS[88]	8.95	4.54	3.28
EELS[73]	8.8	—	—

Table 3.4: Measured values for SiO_2 band gap and SiO_2-Si VBO and CBO.

3.12 Importance of Sample Preparation; Specific Cases

In order to highlight the dependence of oxide band gaps and oxide-Si band offsets on sample preparation, which underlies the importance of measuring the valence and conduction bands in the same vacuum chamber, I will describe some specific instances where sample preparation has had an impact on these parameters. In a study by Fulton *et al.*, thin films of HfO_2, ZrO_2 and TiO_2 were grown on SiO_2/Si by remote plasma oxidation or remote plasma enhanced chemical vapor deposition. The authors then measured the VBO's of these samples using UPS and XPS before and after annealing them at 500°. They found that the VBO values increased by 0.7 eV, 2.0 eV and 0.9

eV for HfO_2/Si and ZrO_2/Si, TiO_2/Si, respectively, after the annealing.[71] The large changes in VBO were attributed to excess oxygen in the as deposited high-κ films, which was driven out by the annealing.

Mondreanu *et al.* studied the effect of both film growth and processing on the band gap of HfO_2 films on Si.[44] In this study, HfO_2 films were grown on Si(100) by two chemical vapor deposition (CVD) methods, UV assisted injection liquid source (UVILS) CVD and thermal assisted injection liquid source (TILS) CVD. Spectrscopic ellipsometry was used to measure the HfO_2 band gaps. The structure of the study was that several groups of samples grown, where each group was grown by one of the two CVD methods under a particular set of conditions. Each sample in a group was then exposed to different annealing conditions. In this way, the effect of both the growth conditions and the annealing conditions on the HfO_2 band gap could be analyzed.

In one instance, three HfO_2(94-97 Å)/Si samples were grown by TILS-CVD at 316° in an Ar and O_2 environment. One of the films was left unannealed, while another was annealed at 800°C for 3 min. in O_2, and the other was annealed at 800°C for 3 min. in Ar. The HfO_2 band gaps of the as-deposited film was found to be 5.95 eV, while the band gaps of the O_2 annealed and Ar annealed films were found to 5.83 eV and 5.71 eV, respectively. This result, as well as two others, showed that annealing the sample decreased the band gap. Another observation was that annealing in Ar resulted in a smaller band than annealing in O_2. The largest band gap this group measured was 5.95 eV, and the smallest was 5.66 eV.[44]

Similar behavior for HfO_2 films was reported by Afanas'ev *et al.*[43] In this study, HfO_2 films were grown on Si by CVD, and the HfO_2 band gap and band offsets with Si were measured by internal photoemission (IntPE). The photoconductivity spectrum from as-deposited Au/HfO_2/Si showed a threshold value of 5.9 eV, which gives the value of the band gap of the HfO_2 film. After annealing the sample at 650°C for 10 min in O_2, the photoconductivity spectrum contained a lower energy feature, the threshold of which was 5.6 eV. A large part of the spectrum from the annealed sample, however, could still be fitted with a line that gave a threshold of 5.9 eV. The authors attributed the 5.6 eV band gap to a crystallized portion of the HfO_2 film and the 5.9 eV band

gap with amorphous HfO_2.[43] Though they observe a lowering of the band gap with annealing, the authors only report one value for the HfO_2-Si CBO and VBO, which presumably applies to the HfO_2 in the as-loaded and annealed conditions.

These three studies show that growth method and processing conditions have an impact on the oxide band gap and oxide-semiconductor band offsets of thin film oxide/Si systems. In our study, we have performed both UPS and IPS on the same sample in the same chamber to ensure that measurements used to find the oxide VBM, CBM and band gap were performed on a single sample with a given preparation. The samples measured by SXPS at the NSLS were prepared in conditions that were matched as closely as possible to those in the UHV chamber at Rutgers.

3.13 Si Band Bending

For all of the high-κ oxide on p-Si samples we measured, we observed downward bending bending between 0.8-0.9 eV. In contrast, the SiO_2 on n-Si samples we measured showed upward band bending by 0.1 eV. There are two possible explanations for these results. One is that there is Fermi level pinning at the SiO_2/Si interface, and the Fermi level will always be close to the CBM (n-type), regardless of the doping of the Si. The other is that there are positively charged defect states in the SiO_2 or high-κ layers of the high-κ/Si samples, and not in the SiO_2 layer from SiO_2/Si. This positive charge will draw negative charge carriers to the surface of the Si substrate, bending the bands downward. A full investigation of the Si band bending would involve measurements of high-κ oxides on n-Si, as well as SiO_2 on p-Si. We were not able, however, to obtain these additional samples from those who grew the samples for us.

The explanation of Fermi level pinning should be treated differently for SiO_2/Si and high-κ/Si samples. One of the foundations of the traditional (poly-Si/SiO_2/Si) MOSFET has been that there is little to no Fermi level pinning at the interface for an SiO_2/Si system with a thermally grown, high quality oxide. This allows the lowering of the threshold voltage for traditional n-MOS and p-MOS devices. The presence of the high-κ layer has been shown, however, to have an impact on the properties of the SiO_2

interfacial layer, which may render the SiO_2/Si interface different for MOS stacks with high-κ layers than it is for traditional MOS stacks. Bersuker *et al.* have shown that MOS stacks consisting of TiN/$Hf_{0.8}Si_{0.2}O_2$/SiO_2/Si have interfacial SiO_2 layers that contain positively charged oxygen vacancies.[29] These vacancies also give the SiO_2 layer an increased dielectric constant over that of stoichiometric SiO_2. The substoichiometric condition of the SiO_2 film could have an effect on the SiO_2/Si interface, as well, which may result in Fermi level pinning. In one measurement from an HfO_2/n-Si sample, we observed no significant band bending in the Si. This suggests that Fermi level pinning may explain the downward band bending, but more measurements from high-κ oxide/n-Si substrates would have to be done to demonstrate this in a credible way.

To investigate the explanation of positively charged defects states in the high-κ and SiO_2 layers causing the downward band bending, we considered capacitance-voltage (C-V) measurement results from the literature. In one report, which was mentioned above, Bersuker *et al.* determined that there was positive charge in the SiO_2 layer of TiN/$Hf_{0.8}Si_{0.2}O_2$/SiO_2/Si.[29] They found that this charge was greater if the SiO_2 layer was initially grown thin (∼3-5 Å), in which case it would become thicker (10 Å) during the high temperature anneal (1000°C). While the finding of positive charge in the SiO_2 layer qualitatively supports the possible explanation for the downward band bending we observe, it is difficult to claim that it strongly supports the explanation of positive charge in the oxide layers. First of all, the samples that we measured did not use SiO_2 layers that were intentionally grown thin, which showed the greatest density of positive charge in the study. Second, the samples in the study discussed above were annealed at a different temperature than our samples were annealed, which weakens the validity of a comparison. Thus, this study provides only moderate support for the explanation of positive charge in the oxide layers. It should also be noted that we observe downward band bending in high-κ/Si samples that have not been annealed, which suggests that growth conditions may have a role in the downward band bending.

Another report of C-V results, where Ru_xTa_{1-x}/HfO_2/SiO_2/Si systems were measured, determined the density of charge at the HfO_2/SiO_2 and SiO_2/Si interfaces. This study, performed by Rashmi *et al.* showed that there was negative charge at

the HfO_2/SiO_2 interface, and slightly lower density of positive charge at the SiO_2/Si interface.[89] The charges at these interfaces roughly negate each other in terms of the effect on band bending in the Si. Thus, this report does not support the explanation of positive charge in the oxide layers as the cause of the band bending.

At this point, the explanation for the downward band bending in the Si from high-κ oxides on p-Si substrates must be considered an open question. More measurements should be made on high-κ/n-Si samples to see if there is negligible band bending, which would suggest that there is Fermi level pinning at the SiO_2/Si interface when there is a high-κ oxide on top of the SiO_2 in the stack. The explanation of positive charge in the oxide layers could be investigated by annealing the high-κ/p-Si samples in a passivating environment. If the charged defects could be passivated, the band bending in the p-Si would be alleviated.

3.14 Conclusions

In this chapter, I have shown that the combination of UPS and IPS in the same vacuum chamber is an effective way to measure the occupied and unoccupied DOS of thin film oxide/Si samples, and to find the energy of the oxide VBM and CBM with respect to the Fermi level. The oxide-Si band offsets were found from the VBM and CBM of the oxide thin film and the Si VBM, determined from the emission in the oxide band gap region in the SXPS spectra. We measured the band offsets in this way for a number of oxide/Si thin film samples and found them to be in good agreement with experimental and theoretical results from the literature, with the exception of some outlying literature values. As high-κ oxide band gaps and band offsets with Si have been shown to vary with sample growth and preparation, and have been measured by a wide variety of experimental techniques, a wide range of experimental results is not surprising.

We have shown that the band offsets with Si for the leading candidates to replace SiO_2 as the gate dielectric, HfO_2 and $Hf_{0.7}Si_{0.3}O_2$, both have a sufficient CBO with Si (1.9 eV and 2.1 eV, respectively) to be used in MOSFET's, as they are greater than 1.0

eV.[28] We have also shown that ZrO_2 and Al_2O_3 also have sufficient band offsets with Si, though they are held back from use in MOSFET's due to thermal instability and low dielectric constant, respectively. A trend that we have observed in our measurements of the high-κ oxide/Si samples is downward band bending in the Si of up to 0.9 eV. The effect may either be due to Fermi level pinning at the SiO_2/Si interface of high-κ/Si samples, or due to positive charged defect states in the high-κ or SiO_2 interfacial layers.

Chapter 4

Metal Oxide Band Offsets

4.1 Introduction

In current MOS technology, highly doped polycrystalline Si (poly-Si) is used as the gate material, which is separated from the semiconductor by a thin (10-20 Å) SiO_2 layer. The poly-Si gate has the advantages of a tunable work function that is used to control the threshold voltage, a low defect interface with SiO_2, and compatibility with well established Si manufacturing processes. However, the poly-Si gate also suffers from gate depletion, where a depletion layer forms in the gate, decreasing the overall capacitance of the MOS stack. Diffusion of dopants from the poly-Si gate into the gate dielectric and Si substrate is also an important drawback of a poly-Si gate. The issues of gate depletion and dopant diffusion could be avoided by using a metal as the gate electrode.

The investigation of metal gate electrodes has been coupled with that of high-κ gate dielectrics for a number of reasons. First, the need to eliminate gate depletion is intensified by the fact that the percentage by which the total capacitance is decreased due to gate depletion increases as the oxide capacitance decreases. Second, as SiO_2 will no longer be the gate dielectric, the advantage of a low defect Si-SiO_2 interface for a poly-Si gate is eliminated. Third, it has been shown that a poly-Si gate cannot be used to control the threshold voltage in both n-MOS and p-MOS high-κ MOS stacks as it can in traditional MOS stacks.[36] This phenomenon has been associated with Fermi level pinning. Lastly, it would be practical to introduce the new gate electrode and gate dielectric manufacturing processes simultaneously.

To successfully implement metal gate electrodes into CMOS transistors, two metal gates are needed, one with a high work function to be used in the p-MOS stack (n-Si

substrate), and one with a low work function to be used in the n-MOS stack (p-Si substrate). The work function difference between the metal and semiconductor has the effect of bending the Si bands, as shown in Fig. 4.1 (and discussed in Chapter 1, Section 5), which reduces the threshold voltage for each device.

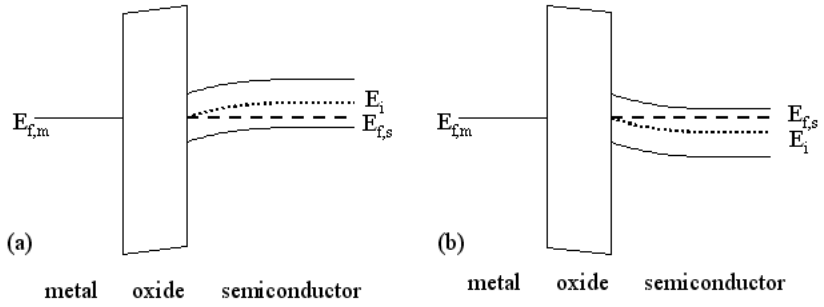

Figure 4.1: Band diagrams for an (a)n-MOS stack with a low work function metal and (b)p-MOS stack with a high work function metal.

Several high and low work function metals have been investigated to determine if they can be used as metal gate electrodes. A suitable metal will have an appropriate work function to sufficiently lower the threshold voltage. It will also have large band offsets (at least 1.0 eV) with the oxide to block gate leakage current.[28] Finally, a suitable metal will not diffuse into the dielectric or semiconductor layers during high temperature annealing, and will not react strongly with the high-κ gate dielectric.

A number of high work function candidate metals have emerged from these studies, such as Pt, Ru, Au and Ni.[37, 90] Finding a suitable low work function metal has been more difficult, however, due to the tendency of low work function metals to react with the high-κ gate dielectric, which may alter the electrical properties of the MOS stack. In an effort to investigate both high and low work function metals, we have studied the properties of one high work function metal (Ru) and two low work function metals (Al, Ti) on high-κ oxide/Si systems. We have measured the band offsets between each of these metals and several oxide thin films. Using core level spectroscopy, we have also observed the degrees of oxidation and reduction that take place within the layers of the MOS stacks as a result of the deposition of the metal layers.

One issue that we can address through observation of the composition of layers in the MOS stack is the reduction of the interfacial SiO_2 layer. The presence of an SiO_2

layer between the high-κ oxide and semiconductor layers in an MOS stack is a well known problem, which has the effect of decreasing the total capacitance of the stack. Removing this layer would increase the capacitance of the MOS stack, but it would most likely have a negative effect, as well. This effect is a decrease the mobility of the charge carriers in Si due to Coulomb scattering by defect states in the region of the SiO_2/Si interface that trap charges.

The removal of part or all of the interfacial SiO_2 layer in an HfO_2/Si system has been demonstrated by Stemmer, *et al.*[91] In this study, Ti, Al and Pt metal gates were grown on identical HfO_2/Si systems. Through transmission electron microscopy (TEM), it was shown that the SiO_2 interfacial layer was thinner in stacks with Ti gates than it was in stacks with a Pt or Al gates. Electrical measurements were also reported in this study, which showed that the stack with the Ti gate had a higher capacitance than the other stacks, confirming the reduced thickness of the SiO_2 interfacial layer. Using core level spectroscopy, we were also able to evaluate the ability of a gate metal to reduce the interfacial layer in a thin film high-κ MOS stack.

In this chapter, I will explain the spectroscopic methods we used for measuring the metal-oxide band offsets in an MOS stack, and present our results. These results will be compared with band offset values from the interface gap state (IGS) model. I will also present observations of the degrees of oxidation and reduction throughout the MOS stack, which will be discussed with regards to their effect on band offsets and their relevance to the reduction of the interfacial layer. Lastly, I will describe other experimental methods for determining metal-oxide band offsets and compare our results with results obtained using these methods.

4.2 Experimental Methods

We have performed UV photoemission spectroscopy (UPS), inverse photoemission spectroscopy (IPS), and soft x-ray photoemission spectroscopy (SXPS) on several MOS stacks with various combinations of Ru, Al and Ti metal gates and HfO_2 (15 Å), $Hf_{0.7}Si_{0.3}O_2$ (20 Å), Al_2O_3 (25 Å) and SiO_2 (20 Å) oxides on Si substrates. The thin

high-κ oxide films were grown on the Si substrates by either atomic layer deposition (ALD) or metallorganic chemical vapor deposition (MOCVD), and the SiO_2/Si sample was grown by thermal oxidation. These films were grown in other laboratories and sent to us for characterization. All of the thin film samples we measured were annealed at 500-600° C for 3-5 min. in ultra-high vacuum to remove atmospheric contamination. The spectroscopic measurements were made in two vacuum chambers. One chamber, at Rutgers University, was equipped with UPS and IPS capabilities. The second chamber, an end station on beamline U5 at the National Synchrotron Light Source (NSLS), was equipped with SXPS capability. Both chambers housed Ru, Al, and Ti metal deposition sources.

In order to measure the metal-oxide band offset, we first measured the electronic properties of the clean surface of an oxide/Si sample. Then we evaporated a thin layer (usually ∼2-5 Å) of metal onto the oxide surface, as monitored by a quartz crystal microbalance, and measured the electronic properties of the surface region. This process of deposition and measurement was continued until it was clear that the oxide states had stopped shifting. The band offsets were then determined by the energies of the oxide valence band maximum (VBM) and conduction band minimum (CBM) before metallization and the shifts in these energies upon metallization. The method will be described in more detail below.

4.3 Metal-Oxide Band Offsets for Ru/HfO_2/Si

Fig. 4.2(a) and (b) show UPS and IPS spectra from a HfO_2/Si sample that was sequentially metallized with Ru. It should be noted that there is an SiO_2 interfacial layer approximately 10 Å thick between the HfO_2 and Si layers in this sample, as there also is in the $Hf_{0.7}Si_{0.3}O_2$/Si and Al_2O_3/Si samples that will be discussed in this chapter. For simplicity, however, I will not list the interfacial layer when identifying the materials in the stack. The UPS spectra in Fig. 4.2(a) were normalized with respect to the peak intensity of the valence band. The IPS spectra in Fig. 4.2(b) were normalized with respect to electron dose, which is the sample current multiplied by the time of the spectrum.

The UPS and IPS spectra from the clean HfO_2 surface, shown in black in Fig. 4.2(a) and (b), respectively, were linearly fit using the procedure described in Chapter 3, Section 4, to find the VBM and CBM. This procedure involves performing a linear fit to the valence and conduction band edges closest to the Fermi level, as well as to the intensity in the band gap region. The energies where the band edge fits cross the band gap region fits are the band edge energies, which are -3.8 eV and 1.9 eV for the HfO_2 VBM and CBM, respectively. We have analyzed this fitting procedure by obtaining a VBM closer to and farther from the Fermi level using standard deviations (σ) from the linear fitting routine. The VBM value closer to (farther from) the Fermi level was determined by adding (subtracting) 2σ to (from) the slope and y-intercept of the linear fit. The VBM values obtained using these modified linear fits were within ± 0.1 eV of the original value. From this analysis, we estimate the uncertainty of the band edge energies to be ± 0.1 eV.

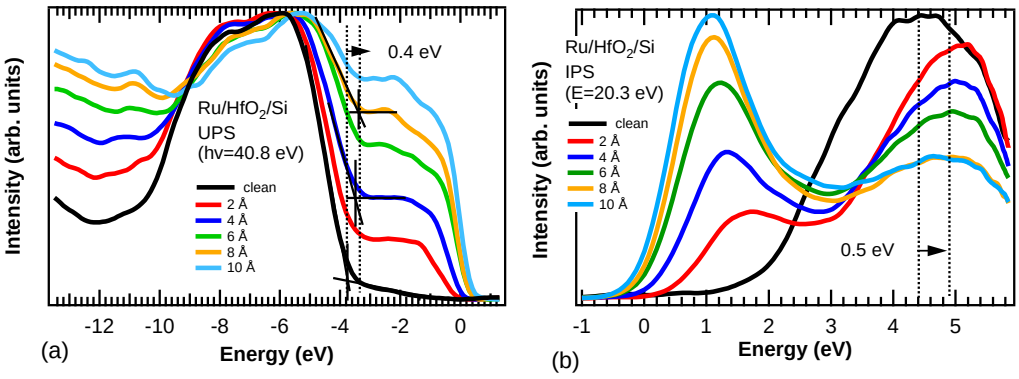

Figure 4.2: (a)UPS and (b)IPS measurements of HfO_2/Si metallized with Ru.

Once Ru is deposited onto the surface, Ru states can be seen in the UPS and IPS spectra in the band gap region of HfO_2. The occupied Ru states in the HfO_2 band gap region have $5s$ and $4d$ orbital character, and appear relatively flat in the UPS spectra. The Ru states above the Fermi level have a strong feature centered at $\sim$1 eV, which is due to $4d$ states. As the Ru coverage increases, the HfO_2 states are more and more attenuated, but are still visible in the spectra for coverages up to $\sim$10 Å. The HfO_2 VBM can be determined from the UPS spectra from the Ru covered surfaces using the linear fitting procedure. This is the case as long as the states from the metal

overlayer are relatively uniform and do not greatly alter the shape of the oxide band edge. Applying the linear fitting procedure to the spectrum of the 10 Å Ru covered surface, as shown in Fig. 4.2(b), gives a VBM of -3.4 eV. Thus, the shift in the HfO_2 VBM upon Ru deposition is 0.4 eV upwards in energy.

The best way to find shift in energy of the HfO_2 states due to Ru coverage from the IPS spectra shown in Fig. 4.2(b) is to use the peak of the HfO_2 conduction band. The conduction band edge cannot be used because the Ru $4d$ feature strongly alters the shape of the HfO_2 conduction band in the region of the band edge. In contrast, the shape of the HfO_2 conduction band in the region of the peak is not altered significantly with Ru converage. The HfO_2 conduction band peak is centered at 4.4 eV in the IPS spectrum from the clean surface, and is centered at 4.9 eV in the spectrum from the 10 Å Ru covered surface. Thus, the oxide states are observed to shift upwards in energy by 0.5 eV. In both the UPS and IPS spectra, it is interesting to note that the full shift in energy of the HfO_2 VBM and CBM is complete or nearly complete after the first deposition of Ru.

Fig. 4.3(a) and (b) show SXPS spectra of the valence band and Hf $4f$ core levels, respectively, from a sequentially metallized $Ru/HfO_2/Si$ sample taken at a photon energy of 150 eV. The valence band and core level spectra were both normalized with respect to maximum intensity of the spectra from the clean surface. By the linear fits shown in Fig. 4.3(a), the VBM of the clean HfO_2 surface was found to be -3.6 eV. For the 10 Å covered surface, the HfO_2 VBM is -3.3 eV, shifted upward in energy by 0.3 eV. It should be noted that the HfO_2 VBM from the clean surface as determined by SXPS differs slightly (0.2 eV) from the HfO_2 VBM determined by UPS. We will use the VBM from the UPS measurement in further band offset analysis because it can combined with the IPS measurement from the same sample in the same chamber to determine the band gap.

Core level spectroscopy is the best way to determine the shift in the energy of the oxide states as a result of metal deposition. This is due to the well defined shapes of core levels, which allows for clear marking of their energies. Fig. 4.3(b) shows the Hf $4f_{5/2}$ and $4f_{7/2}$ lines from the clean and Ru covered HfO_2/Si. In the spectrum from

the clean surface, the Hf $4f_{5/2}$ and $4f_{7/2}$ lines are centered at binding energies of -19.3 and -17.7 eV, respectively, which are characteristic of Hf in the 4+ oxidation state.[92] In the spectrum from the 10 Å Ru covered surface, the Hf $4f_{7/2}$ line is centered at -17.2 eV. Thus, the presence of the Ru layer shifts the HfO_2 states upwards in energy by 0.5 eV. The four values that we have found for energy shift in the HfO_2 states due to Ru deposition, 0.4 eV, 0.5 eV, 0.3 eV and 0.5 eV, are consistent in direction and magnitude to within 0.2 eV. When it is available, we will use the energy shift value determined from the core levels to determine the metal-oxide conduction band offset. The consistency between the energy shifts determined from valence band, conduction band and core level spectra that was generally observed, however, justifies the use of energy shifts determined from other spectra when core level spectra are not available.

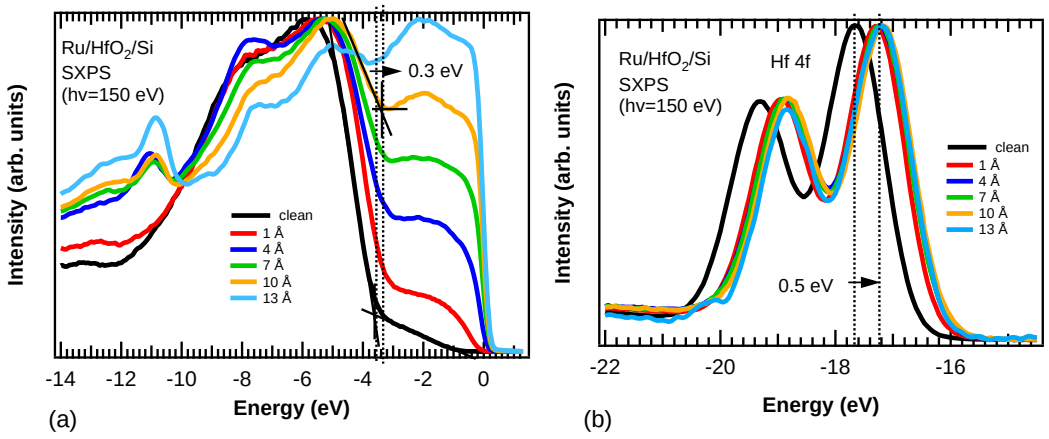

Figure 4.3: SXPS (a)valence band and (b)Hf $4f$ core level spectra from HfO_2/Si metallized with Ru.

As the shifts that occur in the HfO_2 states upon Ru deposition are, in principle, electrostatic, it is not surprising that we observe consistent shifts for the HfO_2 VBM, CBM and core levels. In order to determine the metal-oxide VBO, we add the energy shift upon metallization (E_s) to the clean surface VBM. As shown Fig. 4.4(a), the VBM is the energy of the HfO_2 valence band maximum (E_v) with respect to the Si Fermi level. When the metal layer is deposited, the Fermi level of the metal aligns with that of the Si, as shown in Fig. 4.4(b). Adding the energy shift to the VBM determined prior to metal deposition gives the new energy of the HfO_2 VBM with respect to the metal

Fermi level, the absolute value of which is the metal-oxide VBO ($\Delta E_{v,mo}$). Similarly, the metal-oxide conduction band offset (CBO, $\Delta E_{c,mo}$) is found by adding the CBM of the high-κ oxide (E_c) to the shift upon metallization. In the case of Ru/HfO_2, we find a clean surface VBM and CBM of -3.8 and 1.9 eV, and a shift upon metallization of 0.5 eV, which gives a metal-oxide VBO and CBO of 3.3 eV and 2.4 eV, respectively.

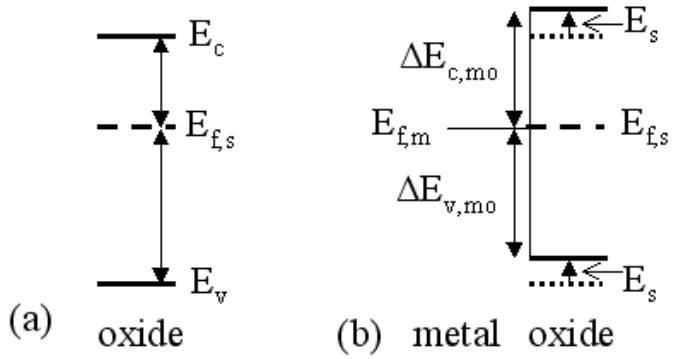

Figure 4.4: (a) Band diagram of an oxide on a thin film oxide/Si sample, where the Fermi level is extrapolated into the oxide from the Si. (b) Adding the shift in oxide states upon metallization to the oxide VBM and CBM gives the metal-oxide VBO and CBO.

4.4 Metal-Oxide Band Offsets for Al/HfO_2/Si and Ti/HfO_2/Si

We have also measured HfO_2/Si samples sequentially metallized with Al and Ti to find the Al/HfO_2 and Ti/HfO_2 band offsets. Fig. 4.5(a) and (b) show the SXPS valence band and Hf 4*f* level spectra, respectively, from sequentially metallized Al/HfO_2/Si. One difference between the valence band spectra from Al/HfO_2/Si and Ru/HfO_2/Si is that the emission due to Al states in the HfO_2 band gap region is much weaker than that from the HfO_2 layer, even at a relatively high Al coverages (27 Å). This is not the case for valence band spectra of Ru/HfO_2/Si, where the intensity of the Ru states in the band gap region exceeds that of the HfO_2 states at a thickness of approximately 13 Å. The low intensity of the Al states is due to the low cross section of Al 3*s* and 3*p* states near the Fermi level. In Fig. 4.5(a), the clean surface HfO_2 VBM is found to be -3.9 eV, and the VBM of the 27 Å Al covered surface is -4.4 eV. Thus, the energy shift due to Al metallization is -0.5 eV.

The effect of Al deposition on the Hf $4f$ core levels is shown in Fig. 4.5(b). The Hf $4f_{7/2}$ line is centered at an energy of -17.9 eV in the spectrum from the clean surface. In the spectrum from the 27 Å Al covered surface, Hf $4f_{7/2}$ level is centered at -18.3 eV, shifted downwards in energy by 0.4 eV. As with $Ru/HfO_2/Si$, it is interesting to not that the full shift of HfO_2 states occurs with the first Al deposition. By adding the energy shift in the Hf $4f$ core level (-0.4 eV) to the VBM and CBM from the UPS and IPS measurements of the clean HfO_2 surface (-3.8 eV and 1.9 eV, respectively), the Al/HfO_2 VBO and CBO are found to be 4.2 eV and 1.5 eV, respectively.

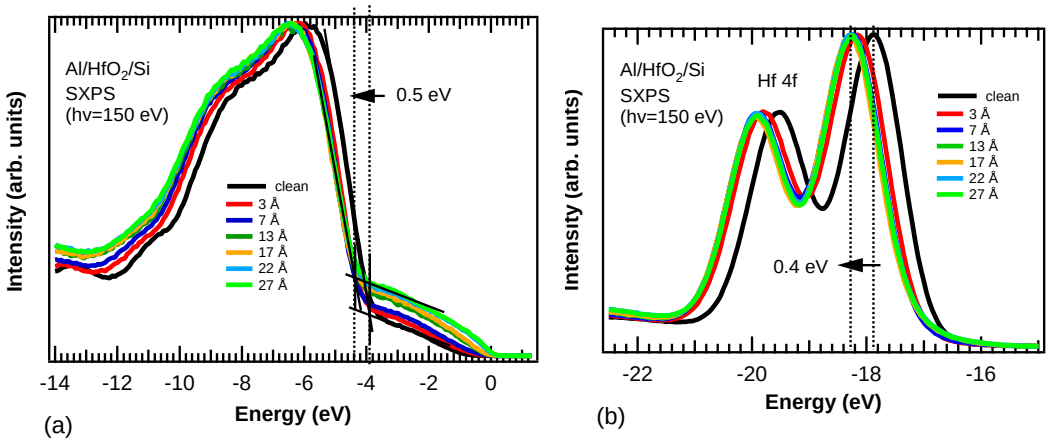

Figure 4.5: SXPS (a)valence band and (b)Hf $4f$ core level spectra from HfO_2/Si metallized with Al.

Fig. 4.6(a) and (b) show SXPS valence band and Hf $4f$ core level spectra from sequentially metallized $Ti/HfO_2/Si$. Analysis of the clean surface spectra in Fig. 4.3(a) gives a value of -3.7 eV for the HfO_2 VBM. It is difficult, however, to find the VBM from the Ti covered surface because the Ti overlayer strongly alters the shape of the HfO_2 valence band, particularly in the region of the valence band edge. It appears, however, that the center of the HfO_2 valence band in the spectrum from clean surface is at approximately the same energy as it is in the spectrum from the 9 Å Ti covered surface. From this observation, we estimate that the shift in the HfO_2 valence band due to the Ti layer is less than $\sim$0.1 eV. In the SXPS spectra from the clean surface shown in Fig. 4.6(b), the Hf $4f_{7/2}$ core level is centered at -17.8 eV. This core level is centered at -17.9 eV in the spectrum from the 9 Å Ti covered surface, shifted downward

in energy by 0.1 eV. Adding this energy shift to the VBM and the CBM from the clean surface gives a VBO and CBO for Ti/HfO_2 of 3.9 eV and 1.8 eV, respectively.

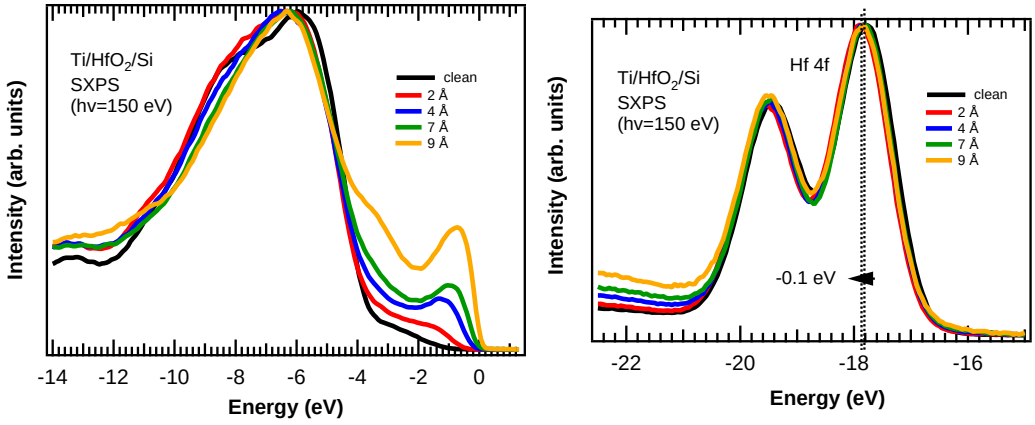

Figure 4.6: (a)UPS and (b) IPS measurements from HfO_2/Si metallized with Ti.

4.5 Energy shifts for Ru/, Al/, and Ti/$Hf_{0.7}Si_{0.3}O_2$/Si

The next three sections (1.5-1.7) will show UPS, IPS and SXPS spectra from samples composed of $Hf_{0.7}Si_{0.3}O_2$/Si that have been sequentially metallized with Ru, Al and Ti. The energy shift in the oxide states upon metallization will be determined from these spectra. A general trend that will be apparent is that the energy shifts determined from the spectra of different features (valence band, conduction band and core levels, where available) agree well. The value of the energy shift (E_s) for each metal-oxide combination is listed Table 4.1, along with the metal-oxide VBO and CBO that it was used to calculate.

Fig. 4.7(a) and (b) show the UPS and IPS spectrum from Ru/$Hf_{0.7}Si_{0.3}O_2$/Si. The VBM of $Hf_{0.7}Si_{0.3}O_2$ shifts upwards in energy by 0.4 eV. The CBM also shifts upwards in energy by 0.4 eV, as observed by the shifting of the peak of the HfO_2 conduction band.

Fig. 4.8(a) and (b) show the UPS and IPS spectra from Al/$Hf_{0.7}Si_{0.3}O_2$/Si, respectively. Metallization with Al causes the $Hf_{0.7}Si_{0.3}O_2$ VBM and CBM to shift downward in energy by 0.6 eV and 0.5 eV, respectively. The SXPS valence band and Hf 4f spectra

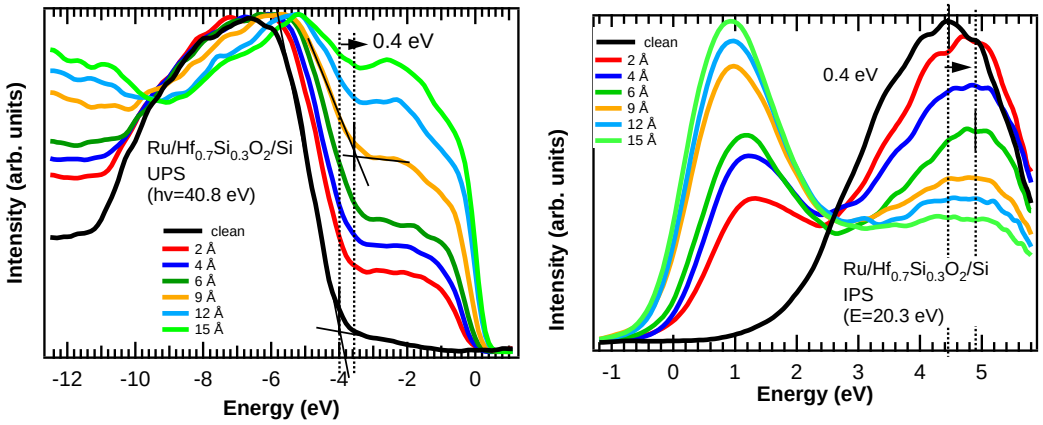

Figure 4.7: (a)UPS and (b)IPS measurements from $Hf_{0.7}Si_{0.3}O_2$/Si metallized with Ru.

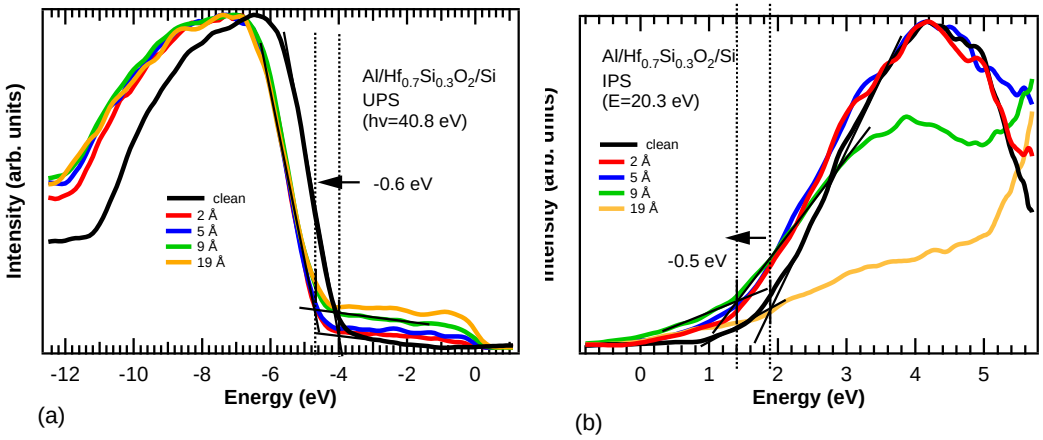

Figure 4.8: (a)UPS and (b)IPS measurements from $Hf_{0.7}Si_{0.3}O_2$/Si metallized with Al.

from Al/$Hf_{0.7}Si_{0.3}O_2$/Si are shown in Fig. 4.9(c) and (d), respectively. We observe a downward energy shift for the VBM of 0.6 eV, and a downward energy shift for the Hf $4f$ level of 0.5 eV. The energy shift from the core levels, -0.5 eV, is used to calculate the metal-oxide band offsets in Table 4.1.

The SXPS valence band and Hf $4f$ spectra from Ti/$Hf_{0.7}Si_{0.3}O_2$/Si are shown in Fig. 4.10(a) and (b), respectively. Similar to the valence band spectra of Ti/HfO_2/Si shown in Fig. 4.6(a), it is difficult to determine the shift in the $Hf_{0.7}Si_{0.3}O_2$ VBM from the spectra in Fig. 4.10(a) because the Ti overlayer changes the shape of the $Hf_{0.7}Si_{0.3}O_2$ valence band, particularly in the region of the VBM. The Hf $4f$ level spectra can be used, however, to find an energy shift which is downward in energy by 0.3 eV.

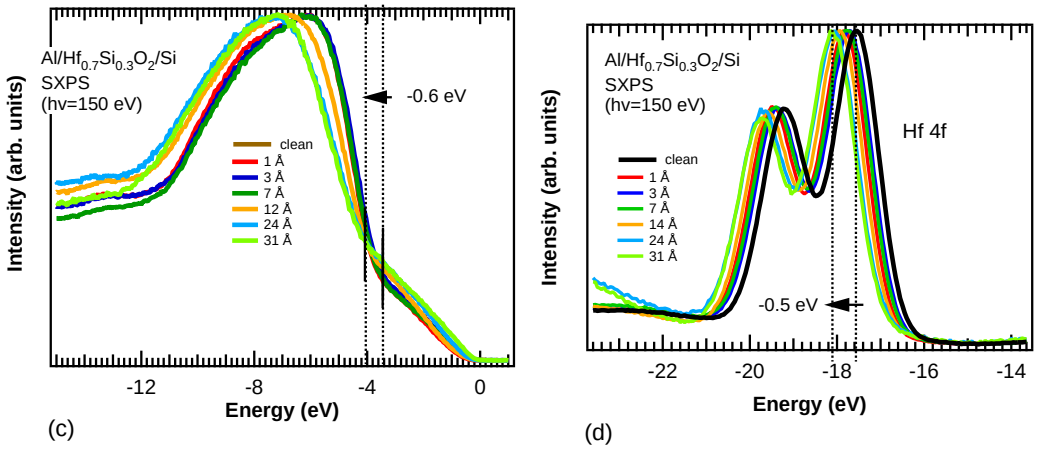

Figure 4.9: SXPS measurements of the (a)valence band and (b)Hf $4f$ core levels from $Hf_{0.7}Si_{0.3}O_2$/Si metallized with Al.

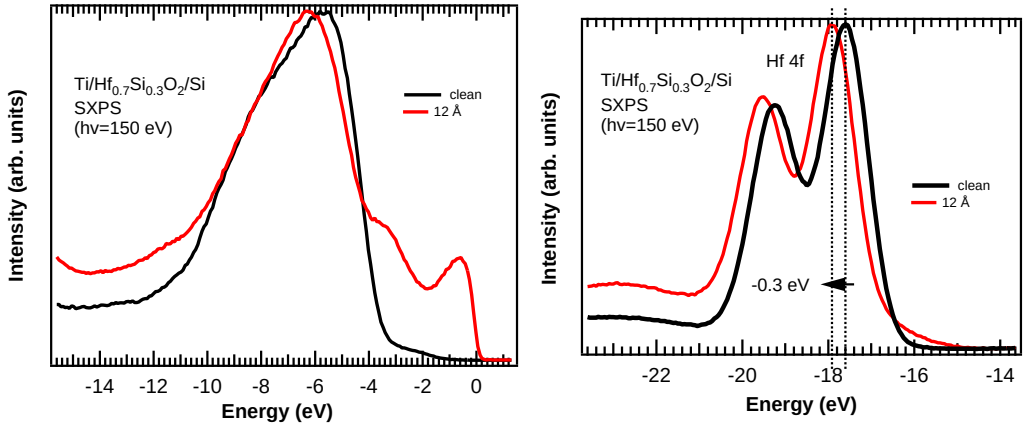

Figure 4.10: SXPS measurements of the (a)valence band and (b)Hf $4f$ core level from $Hf_{0.7}Si_{0.3}O_2$/Si metallized with Ti.

4.6 Energy shifts for Ru/, Al/, and Ti/SiO_2/Si

Fig. 4.11(a) and (b) show the UPS and IPS spectra from Ru/SiO_2/Si. The VBM is observed to shift upwards in energy by 0.3 eV upon Ru metallization. In the determination of the shift of the conduction band states, a feature that can be used is the sharp upward slope in the IPS spectra between 6 eV and 8 eV. By aligning this feature in the IPS spectrum from the clean surface with that in the spectrum from the 3 Å Ru covered surface, we determine that the CBM is shifted upward in energy by 0.3 eV. The IPS spectra for higher Ru coverages show no indication of a reversal of this upward

shift in energy.

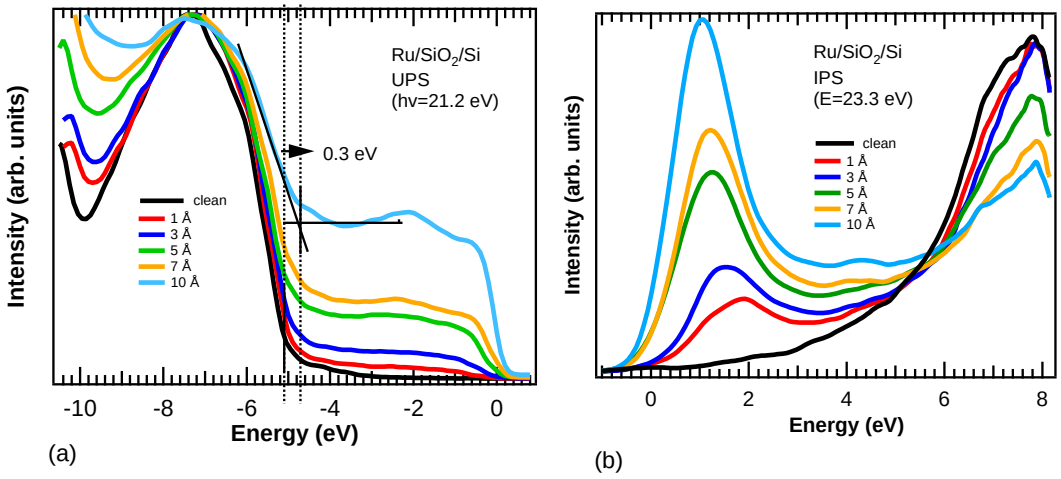

Figure 4.11: (a)UPS and (b)IPS and measurements from SiO_2/Si metallized with Ru.

The SXPS spectrum of the clean SiO_2 surface in Fig. 4.12(a) reveals an additional feature of the SiO_2 valence band, centered at -11.4 eV, which is not entirely visible in the UPS measurement of the clean surface. This feature shifts upward in energy to -11.1 eV with Ru metallization, giving an energy shift of 0.3 eV. The shift found from the VBM in the SXPS spectra is also 0.3 eV.

Fig. 4.12(b) shows the spectra of the Si $2p$ core level. A linear approximation to the background has been subtracted from each spectrum, and the spectra are normalized with respect to the photon beam dose. In the spectrum from the clean surface, the Si $2p$ core level is centered at an energy of -103.5 eV, which characteristic of Si in the 4+ oxidation state.[93, 64] This feature shifts upward in energy by 0.2 eV with Ru metallization. We use the energy shift from the Si $2p$ core level, 0.2 eV, to calculate the Ru/SiO_2 band offsets.

The UPS and IPS measurements from sequentially metallized Al/SiO_2/Si are shown in Fig. 4.13(a) and (b), respectively. In the UPS spectra, the SiO_2 VBM shifts downward in energy by 0.3 eV with Al metallization. The energy shift in the CBM due to Al deposition is difficult to determine because the CBM region of the SiO_2 conduction band is gradually sloped. From the sharp upward slope in the SiO_2 conduction band between 6 and 8 eV, however, we estimate that the shift due to Al metallization is -0.1

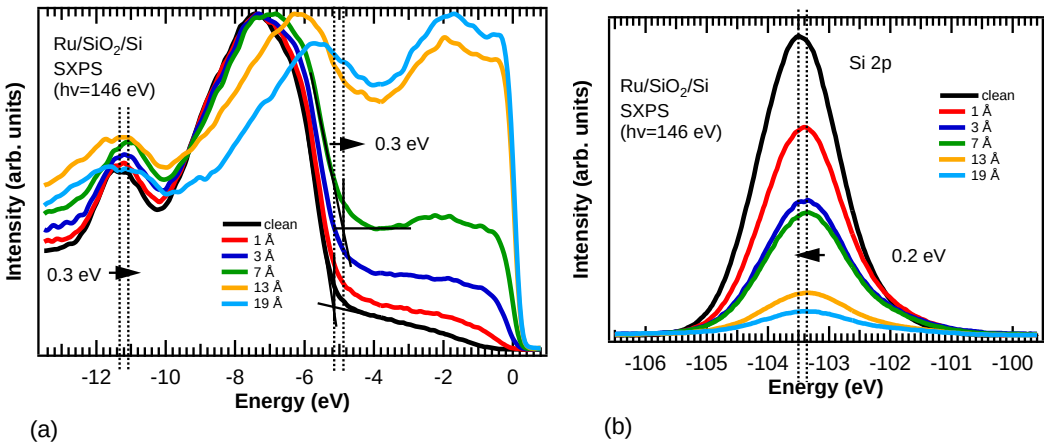

Figure 4.12: SXPS measurements of the (a)valence band and (b)Si 2p core level from SiO_2/Si metallized with Ru.

eV.

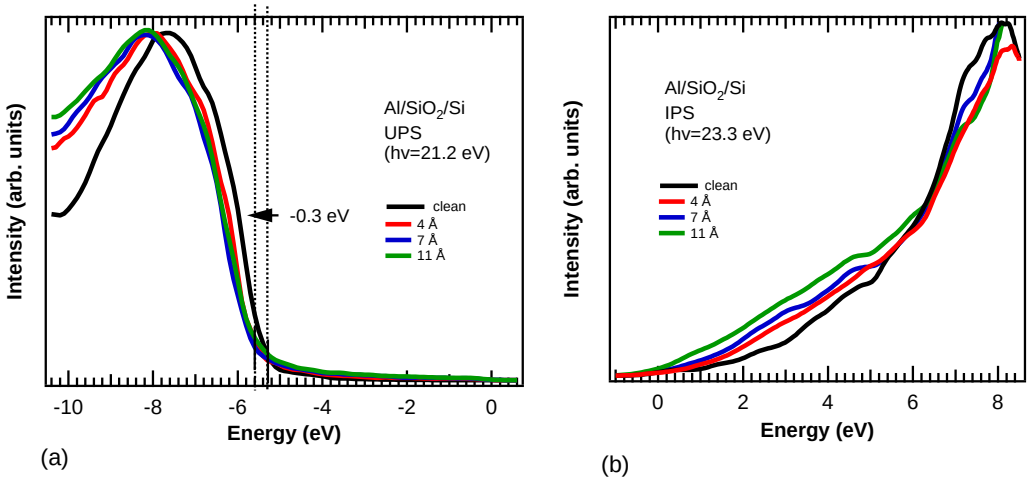

Figure 4.13: (a)UPS and (b)IPS 2p measurements from SiO_2/Si metallized with Al.

The SXPS valence band and Si 2p core level measurements from sequentially metallized Al/SiO_2/Si are shown in Fig. 4.14(a) and (b), respectively. From the spectra in Fig. 4.14(a), a downward shift in energy of 0.1 eV is observed in the VBM, while the feature between -10 eV and -13 eV shifts downward by 0.2 eV. The Si 2p core level is observed to shift downward by 0.1 eV in the spectra in Fig. 4.14(d).

Fig. 4.15(a) and (b) show the UPS and IPS measurements from Ti/SiO_2/Si. The IPS spectra do not yield any information about the shift of the SiO_2 conduction band as

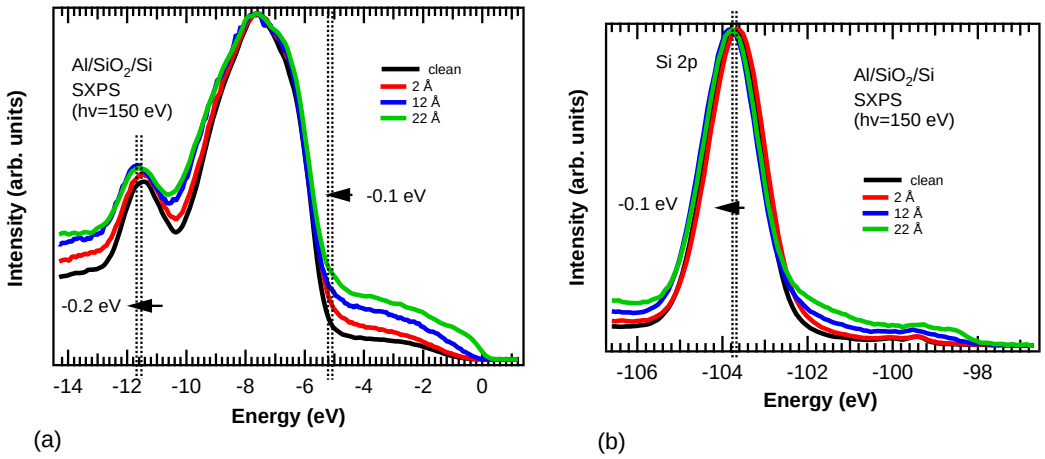

Figure 4.14: SXPS measurements of the (a)valence band and (b)Si $2p$ core level from SiO_2/Si metallized with Al.

the Ti $3d$ feature, centered at $\sim$2 eV, strongly alters the shape of the SiO_2 conduction band seen in the IPS spectra. An energy shift can be determined from the UPS spectra, however, by observing the feature centered between -10 eV and -13 eV. This feature shifts downward in energy by 0.5 eV upon Ti metallization. As with the Ti/HfO_2/Si and Ti/$Hf_{0.7}Si_{0.3}O_2$/Si, the shape of the SiO_2 valence band is altered by the Ti overlayer, making the determination of the energy shift from the VBM difficult. It is interesting to note that the VBM appears to shift upward in energy upon metallization, though the shift we find from the high binding energy valence band feature is downward by 0.5 eV.

4.7 Energy Shifts for Ru/, Al/ and Ti/Al_2O_3

This section describes the determination of the energy shift in Al_2O_3 states upon deposition of Ru, Al and Ti layers. Fig. 4.16(a) and (b) show the UPS and IPS measurements, respectively, from sequentially metallized Ru/Al_2O_3/Si. From the UPS spectra, we find that the Al_2O_3 VBM shifts upward in energy by 0.4 eV. The shift in the Al_2O_3 CBM cannot be determined from the IPS spectra due to the absence of a feature that can be tracked as a function of metal coverage.

The SXPS valence band and Al $2p$ core level spectra from Ru/Al_2O_3/Si are shown

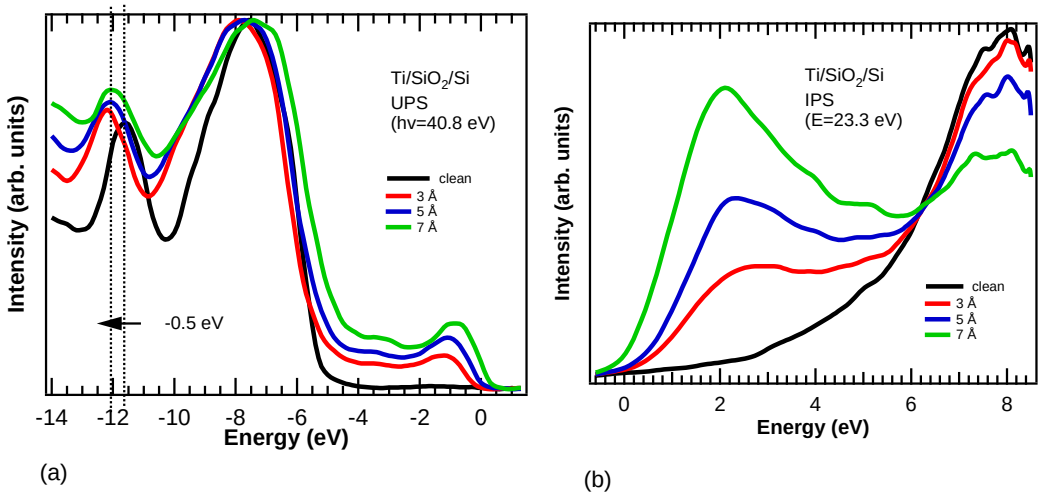

Figure 4.15: (a)UPS and (b)IPS measurements from SiO_2/Si metallized with Ti.

in Fig. 4.17(a) and (b), respectively. The VBM of Al_2O_3 is observed to shift upwards in energy by 0.2 eV upon Ru deposition. The Al $2p$ core level is centered at -75.1 eV in the spectrum from the clean surface shown in Fig. 4.17(b). This is characteristic of Al in the 3+ oxidation state, as demonstrated in previous XPS studies of Al_2O_3. [94, 95] We observe the Al $2p$ core level to shift upwards in energy by 0.3 eV with Ru deposition.

The UPS and IPS measurements of sequentially metallized Al/Al_2O_3/Si is shown in Fig. 4.18(a) and (b). From the UPS measurements, a downward shift in energy of 0.6 eV is observed in the Al_2O_3 VBM. An energy shift cannot be extracted from the IPS measurements. The SXPS measurements from Al/Al_2O_3/Si are shown in Fig. 4.19(a) and (b). The VBM shifts downward in energy by 0.7 eV with metallization. The Al $2p$ 3+ binding energy peak, which is centered at -75.1 eV in the spectrum from the clean surface, shifts downward in energy by 0.7 eV with Al metallization, as well.

The UPS and IPS spectra from sequentially metallized Ti/Al_2O_3/Si are shown in Fig. 4.20(a) and (b). As with the Ti/SiO_2/Si system, the shift of the Al_2O_3 conduction band states cannot be determined from the IPS spectra. A careful analysis of the UPS spectra, however, gives a downward shift in energy of 0.3 eV. After the initial Ti deposition, a downward shift can be observed on the low binding energy side of the Al_2O_3 valence band as well as the high binding energy side. The high binding energy

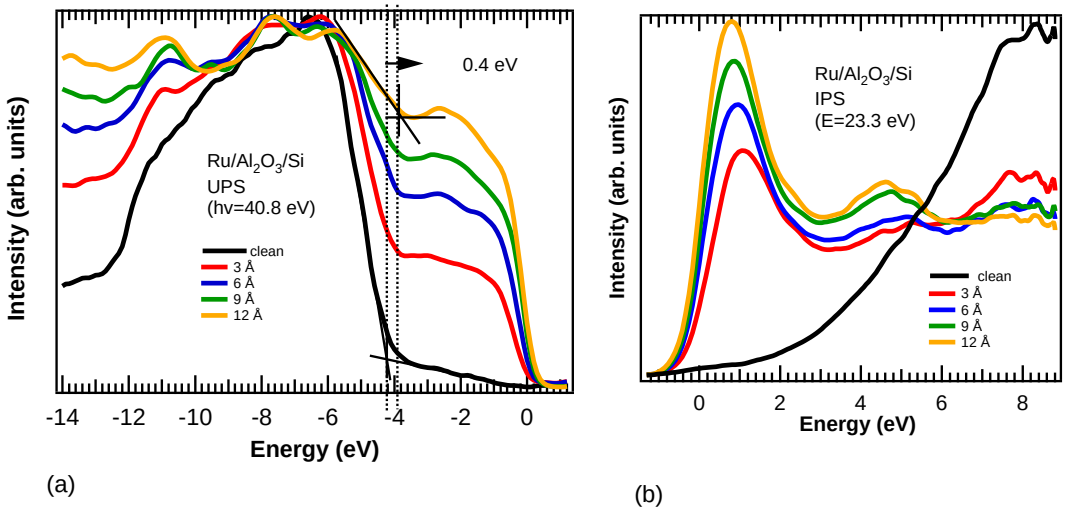

Figure 4.16: (a)UPS and (b)IPS measurements from Al_2O_3/Si metallized with Ru.

side of the valence band can also be observed to shift downward in energy for higher Ti coverages, as well. As the high binding energy side of the valence band in the spectrum from the 6 Å covered surface closely resembles that from the clean surface, while Ti is known to change the shape of the valence band spectrum in the VBM region, we used the high binding energy Al_2O_3 valence band edge to estimate the energy shift in the oxide states.

In order to analyze the higher binding energy side of the Al_2O_3 valence band, a differentiation method was employed. Differentiation of the UPS spectrum from the clean Al_2O_3 surface showed that the inflection point of the high binding energy edge of the valence band occurs at -12.2 eV. The energy of the inflection point of the high binding energy side of the spectrum from the 6 Å covered surface was -12.5 eV. By this analysis, the Al_2O_3 valence band shifts downward in energy by 0.3 eV with Ti deposition. As the VBM seems to shift upwards in energy with greater Ti coverage due to the alteration of the shape Al_2O_3 states in this region, tracking the VBM would give a contradictory and, we believe, misleading shift.

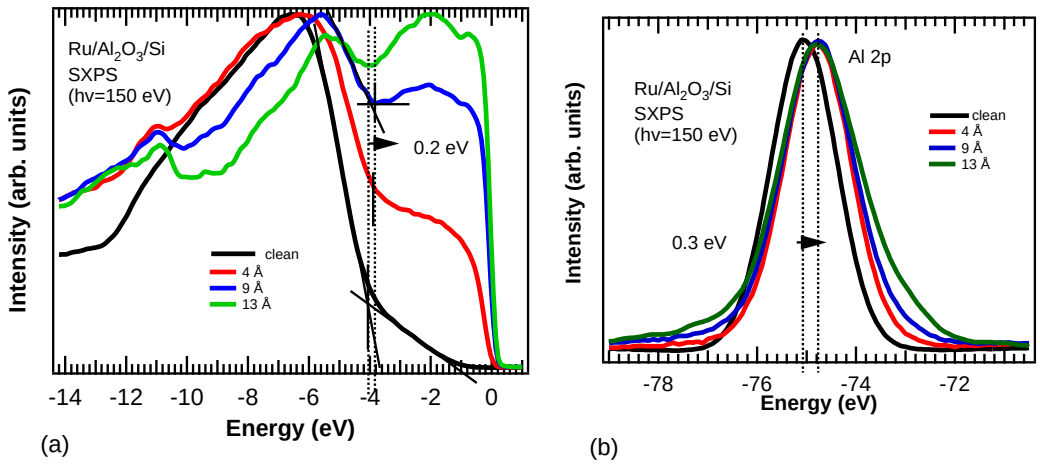

Figure 4.17: SXPS measurements of the (a)valence band and (b)Al $2p$ core level from Al_2O_3/Si metallized with Ru.

4.8 Theoretical Metal-Oxide Band Offsets

The most basic theoretical model for finding the band offsets between adjacent layers of an MOS stack is the Schottky-Mott model. In the Schottky-Mott model, the vacuum levels of all materials are aligned, which is based on the assumption of no charge exchange at the interfaces between the materials. In the Schottky-Mott model, the metal-oxide CBO is the difference between the metal work function and the oxide electron affinity. Similarly, the oxide-semiconductor CBO is the difference between the oxide and semiconductor electron affinities.[34] In an alternative model, attributed to Bardeen, the CBO between a metal and an oxide is determined solely based on the position of a charge neutrality level (CNL) in the band gap of the oxide, at which energy the Fermi level of the metal is assumed to be pinned. The CNL is the energy where the interface states have an equal density of donor type states above and acceptor type below. A more detailed description of the Schottky-Mott and Bardeen models can be found in Chapter 1, Section 6.

The interface gap state (IGS) model is way to interpolate between the extremes of the Schottky-Mott model and Bardeen models. This model can be used to calculate band offsets at a metal-oxide interface or an oxide-semiconductor interface, although in this chapter, only metal-oxide interfaces are considered. It is important to note

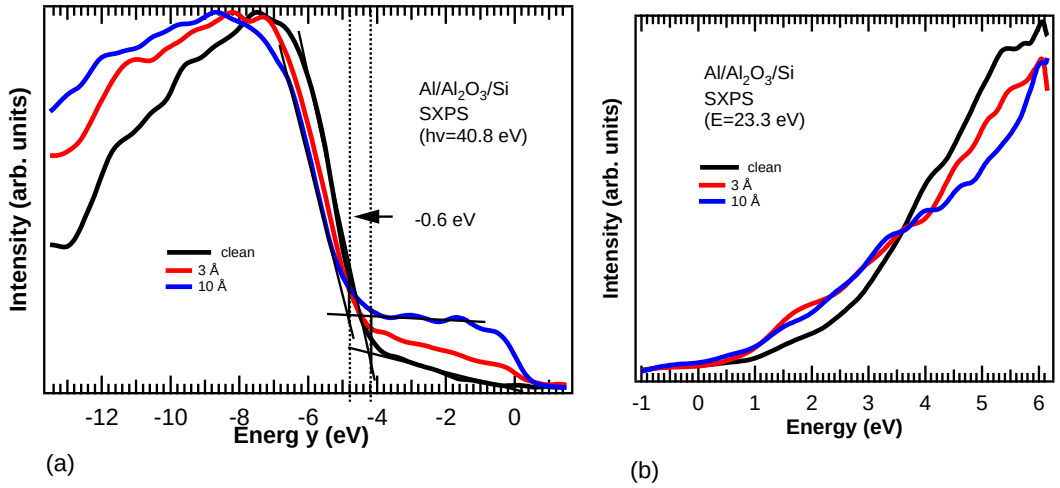

Figure 4.18: (a)UPS and (b)IPS measurements from Al_2O_3/Si metallized with Al.

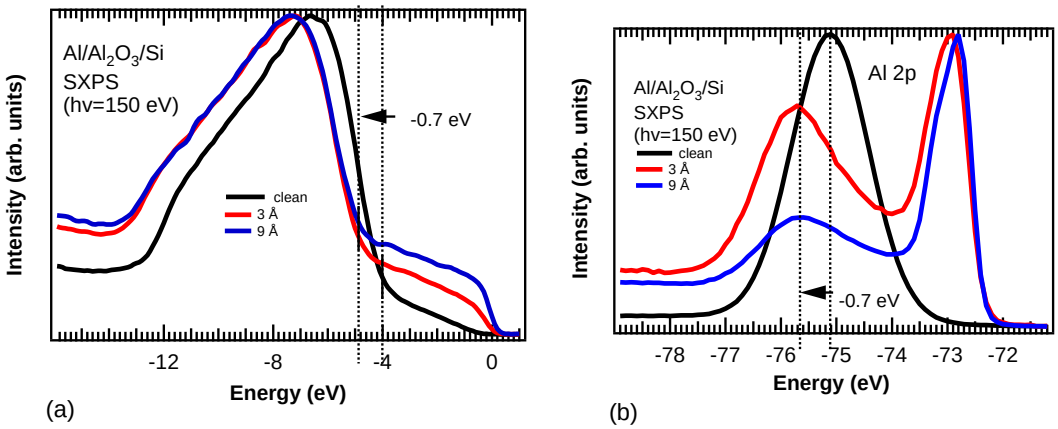

Figure 4.19: SXPS measurements of the (a)valence band and (c)Al 2p core level from Al_2O_3/Si metallized with Al.

that IGS model can only be appropriately applied to a chemically abrupt metal-oxide interface. This is to say that if there is an interfacial layer between the metal and oxide under consideration, the IGS model does not, in principle, describe the CBO between the metal and the oxide.

The IGS model uses a pinning parameter (S), which takes on values between 0 and 1, to interpolate between the cases of no pinning, the Schottky limit (S=1), and total pinning, the Bardeen limit (S=0). The IGS model is frequently used because it allows for straightforward calculation of band offset values to which experimentally determined band offsets can be compared. A numerical value for a metal-oxide CBO

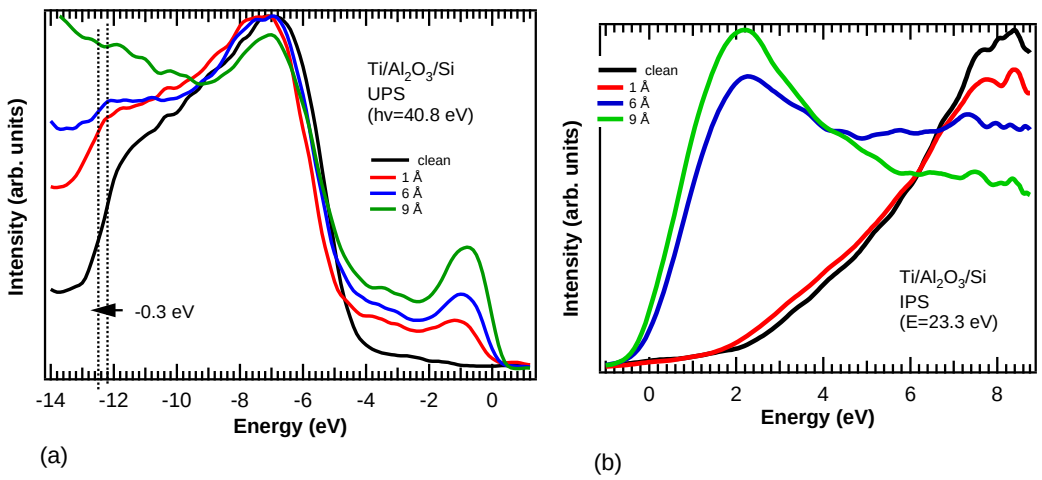

Figure 4.20: (a)UPS and (b)IPS measurements from Al_2O_3/Si metallized with Ti.

can be determined from the IGS model using equation 4.1, where qΦ_{cnl} is the difference between the the vacuum level and the charge neutrality level, qΦ_m is the metal work function, and qχ_{ox} is the electron affinity of the oxide. In order to calculate CBO values from this equation, we used values for the pinning parameter and CNL that were obtained from the literature, along with metal work function and oxide electron affinity values that we measured.

$$\Delta E_{c,mo} = q(\Phi_{cnl} + S(\Phi_m - \Phi_{cnl}) - \chi_{ox}) \tag{4.1}$$

To find a value for S and qΦ_{cnl}, we referred primarily to the work of Robertson[74], and also to the work of Demkov.[33] The pinning parameter of an oxide is determined from the empirical relation given in equation 4.2, that depends only on the high frequency dielectric constant of the oxide. The CNL is the branch point of the complex band structure of the oxide.[34, 74] It is a fixed fraction of the band gap above the VBM. Therefore, it was necessary to rescale the CNL values given by Robertson and Demkov to the band gaps that we measured. Using the rescaled CNL values and the electron affinities we measured, we determined values for qΦ_{cnl}. This quantity is the sum of the oxide electron affinity and the energy of the CNL below the oxide CBM, as shown in Fig. 4.21. It is interesting to note that the IGS model uses only bulk quantities to calculate the CBO, a quantity that would seem to depend, at least to

some degree, on the oxide being a thin film, and/or properties specific to the interface.

$$S = (1 + 0.1(\varepsilon_\infty - 1)^2)^{-1} \tag{4.2}$$

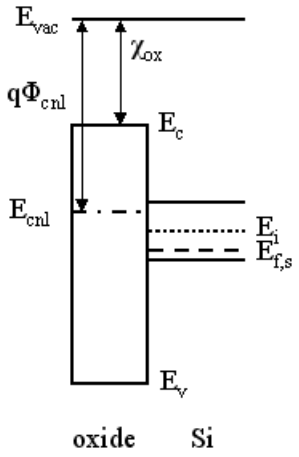

Figure 4.21: Band diagram showing the quantities involved in the IGS model calculation of the metal-oxid CBO.

The work function of a metal and the electron affinity of an oxide or semiconductor can be determined from a UPS measurement, as described in Chapter 2, Section 3. We performed this measurement using He I radiation (21.2 eV), and applying a bias of approximately -5 V to the sample to uniformly raise the energy of the photoelectrons so that the low energy cutoff would be visible in the spectrum. By measuring the width (W) of the UPS spectrum, the difference between the highest occupied state and the vacuum level (E_{vac}) of a sample could be determined by subtracting the spectrum width from the photon energy.

Fig. 4.22(a) shows the UPS measurement described above from a 15 Å Ru film on Si. By fitting the low and high energy edges with straight lines with respect to the background, we find the width of the spectrum to be 16.0 eV. Subtracting the spectrum width from the photon energy (21.2 eV) gives a Ru work function of 5.2 eV. For the other metals we used, Al and Ti, we found work functions of 4.2 eV. Fig. 4.22(b) shows the UPS measurement from a negatively biased HfO_2/Si sample. The width of the UPS spectrum is 13.0 eV. Subtracting this width from the photon energy gives a difference of 8.2 eV between the HfO_2 valence band maximum and the vacuum level.

For a material such as HfO_2, which has a band gap, this energy difference is equal to the band gap plus the electron affinity, as can be seen in Fig. 4.21. Using the HfO_2 band gap of 5.7 eV that we determined for this sample, we find an electron affinity of 2.5 eV. For the other oxides we measured, $Hf_{0.7}Si_{0.3}O_2$, Al_2O_3 and SiO_2, we found electron affinities of 2.8 eV, 2.5 eV and 1.3 eV, respectively. Thus, the value of all of the parameters in equation 4.1 were known, and the metal-oxide CBO could be calculated. Table 4.1 shows the CBO values calculated with the IGS model along with the accompanying VBO values for various combinations of metals and oxide. The experimental CBO values are also listed in Table 4.1 to allow for a comparison between the experimental and IGS CBO values.

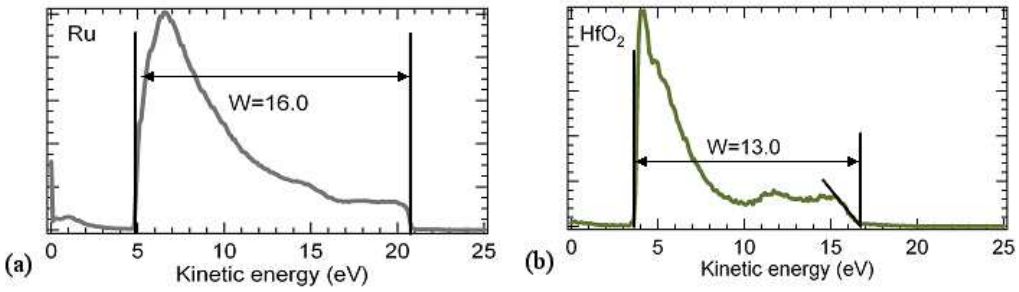

Figure 4.22: Spectrum width measurement of (a)Ru and (b)HfO_2.

metal/oxide	VBM,CBM(eV)	E_s(eV)	VBO,CBO(eV) (Expt.)	VBO,CBO(eV) (Theor.)
Ru/HfO_2	-3.8, 1.9	0.5	3.3, 2.4	3.2, 2.5
$Ru/Hf_{0.7}Si_{0.3}O_2$	-4.0, 2.0	0.4	3.6, 2.4	3.6, 2.4
Ru/SiO_2	-5.3, 3.6	0.2	5.1, 3.8	5.0, 3.9
Ru/Al_2O_3	-4.3, 2.7	0.3	4.0, 3.0	4.3, 2.7
Al/HfO_2	-3.8, 1.9	-0.4	4.2, 1.5	3.8, 1.9
$Al/Hf_{0.7}Si_{0.3}O_2$	-4.0, 2.0	-0.5	4.5, 1.5	4.2, 1.8
Al/SiO_2	-5.3, 3.6	-0.1	5.4, 3.5	5.9, 3.0
Al/Al_2O_3	-4.3, 2.7	-0.7	5.0, 2.0	5.0, 2.0
Ti/HfO_2	-3.8, 1.9	-0.1	3.9, 1.8	3.8, 1.9
$Ti/Hf_{0.7}Si_{0.3}O_2$	-4.0, 2.0	-0.3	4.3, 1.7	4.2, 1.8
Ti/SiO_2	-5.3, 3.6	-0.5	5.8, 3.1	5.9, 3.0
Ti/Al_2O_3	-4.3, 2.7	-0.4	4.7, 2.3	5.0, 2.0

Table 4.1: The experimental values for the metal-oxide VBO and CBO are determined by adding the VBM and CBM of the oxide before metallization and the energy shift (E_s) upon metallization (and taking the absolute value for the VBO). Metal-oxide band offsets values determined with the IGS model are also shown for comparison.

4.9 Discussion of Experimental and Theoretical CBO Values

Table 4.1 shows that the experimental metal-oxide CBO values for samples with Ru overlayers agree well with theoretical CBO values calculated using the IGS model. The experimental and theoretical CBO values for $Ru/Hf_{0.7}Si_{0.3}O_2$ and Ru/SiO_2 are the same, while the theoretical and experimental values for Ru/HfO_2 differ by only by 0.1 eV. The values for Ru/Al_2O_3 differ by a slightly larger amount, 0.3 eV.

There is less agreement for samples with Al overlayers. The experimental and theoretical CBO's for Al/HfO_2, $Al/Hf_{0.7}Si_{0.3}O_2$ and Al/SiO_2 differ by 0.4 eV, 0.3 eV and 0.5 eV, respectively. In the case of Al/Al_2O_3, however, the experimental and theoretical CBO's are the same.

The agreement between the experimental and theoretical CBO's for samples with Ti overlayers is also good. The values differ by only 0.1 eV for Ti/HfO_2, $Ti/Hf_{0.7}Si_{0.3}O_2$ and Ti/SiO_2, while for Ti/Al_2O_3, they differ by 0.3 eV. The slightly larger disparity between the experimental and theoretical CBO for Ti/Al_2O_3 may be attributed to the difficulty in determining the energy shift of the Al_2O_3 states upon metallization. Thus, a general trend of good agreement between the experimental and theoretical CBO values for samples with Ru and Ti overlayers is observed, along with a trend of worse agreement between the values for samples with Al overlayers. To investigate these trends further, we analyzed the composition of the deposited Ru, Al and Ti layers using core level spectroscopy. We found that the composition of the metal layers could be correlated with the trends of agreement between the experimental and theoretical CBO values. This correlation is discussed below.

The composition of the deposited metal overlayer can be evaluated by examining the SXPS spectra of a core level of the metal. Fig. 4.23(a), (b) and (c) show SXPS spectra of the Ru $4p$ core level from sequentially metallized $Ru/HfO_2/Si$, $Ru/SiO_2/Si$ and $Ru/Al_2O_3/Si$, respectively. These spectra are normalized with respect to the incident photon beam. The Ru $4p$ feature, occurring between energies of -42 eV and -48 eV, is composed of the $4p_{3/2}$ and $4p_{1/2}$ states, which overlap each other. The binding energy of the Ru $4p$ feature is in agreement with established binding energy for the Ru $4p$ core

level for metallic Ru.[96]

A key observation from Fig. 4.23(a), (b) and (c) is that as the thickness of the Ru layers increase, the shape of the Ru 4p feature does not change significantly. This shows that the Ru layers are metallic at all thicknesses. From the observation of metallic Ru overlayers, we conclude that the Ru/oxide interfaces are chemically abrupt. This observation correlates with the trend of good agreement between the experimental and theoretical CBO values for the Ru/oxide systems.

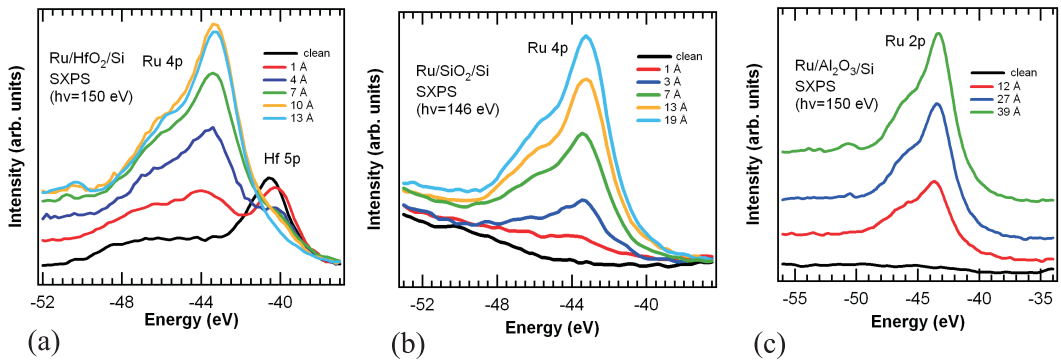

Figure 4.23: SXPS measurement of Ru 4p level from (a)HfO_2/Si, (b)SiO_2/Si and (c)Al_2O_3/Si metallized with Ru.

The behavior of Al overlayers is in sharp contrast to Ru overlayers. SXPS spectra of the Al 2p feature from sequentially metallized Al/HfO_2/Si, Al/$Hf_{0.7}Si_{0.3}O_2$/Si, Al/SiO_2/Si and Al/Al_2O_3/Si are shown in Fig. 4.24(a), (b), (c) and (d), respectively. Fig. 4.24(a), for example, shows the Al 2p feature centered at ∼-75 eV, which is characteristic of Al in the 3+ oxidation state. As the Al thickness is increased, another Al 2p feature grows at ∼-73 eV, which is characteristic of metallic Al (0+).[94, 96] The pattern of an oxidized Al overlayer at lower coverages, and a stronger metallic component at higher Al coverages is evident for Fig. 4.24(a), (b) and (c). In Fig. 4.24(d), however, the Al 2p spectra from Al/Al_2O_3/Si, the metallic Al component is strong even at low coverages. The shift in the Al 2p core level from the Al_2O_3 layer by -0.7 eV was used to calculate the Al/Al_2O_3 CBO in earlier in this section.

We interpret these core level spectra as showing that there is an interfacial Al_2O_3 layer between the Al film and the oxide for Al/HfO_2/Si, Al/$Hf_{0.7}Si_{0.3}O_2$/Si, Al/SiO_2/Si. This observation can be correlated with the trend of poorer agreement between the

experimental and IGS CBO values for samples with Al overlayers. The presence of this interfacial Al_2O_3 layer can explain this poorer agreement makes because the IGS model cannot be appropriately to the Al-oxide interface, as it is not not chemically abrupt. The notable exception is $Al/Al_2O_3/Si$, which has a chemically abrupt metal-oxide interface despite the possibility of some additional Al_2O_3 growth, and for which we find agreement between the IGS and experimental CBO values.

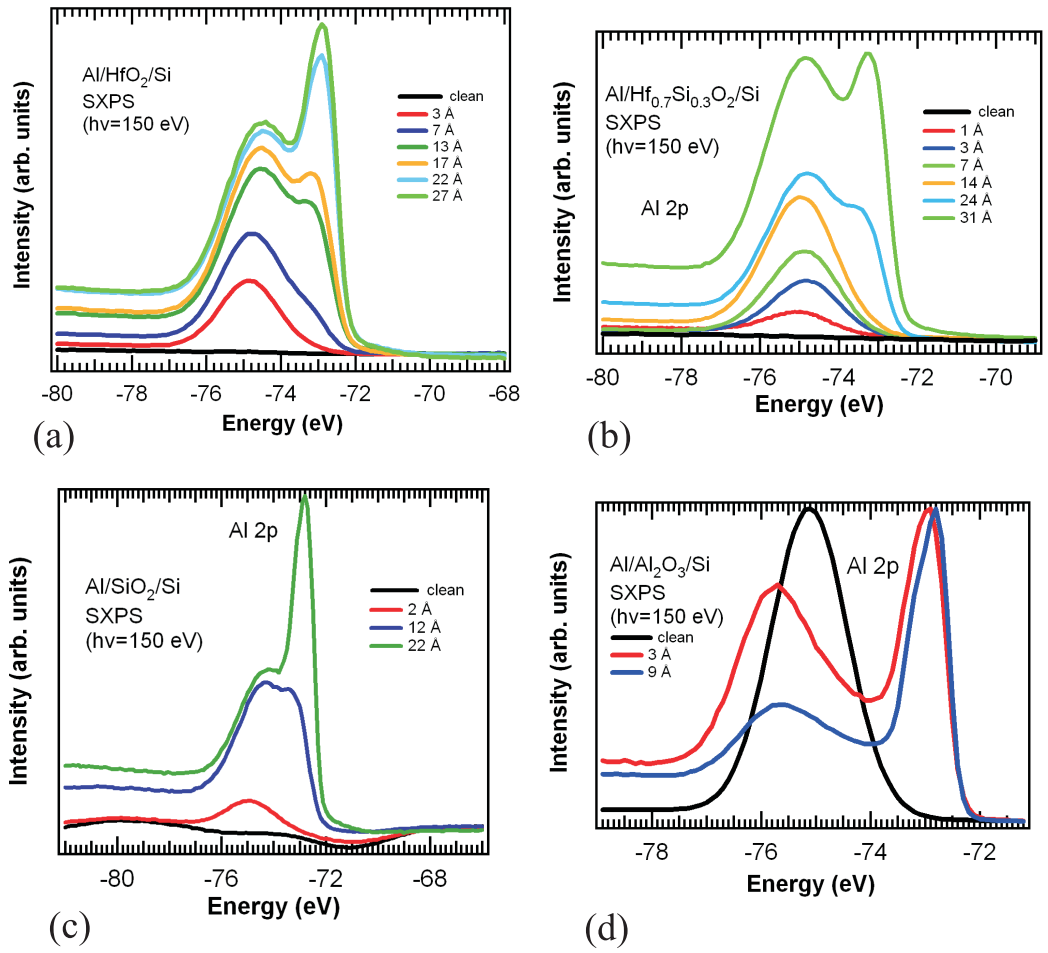

Figure 4.24: SXPS measurement of the Al $2p$ core level from sequentially metallized (a)HfO_2/Si, (b)$Hf_{0.7}SiO_2/Si$ and (c)/SiO_2/Si metallized with Al.

Another factor that influenced the Al $2p$ core level lineshape must be noted. While performing SXPS measurements, exposure to the photon beam resulted in additional oxidation of the Al overlayer. This is shown in Fig. 4.25, where the Al 0+ peak reduces in intensity as a function of exposure to the photon beam. Once the sample is moved so that the beam strikes it at a different spot, the Al 0+ is restored to its original

intensity. Though the beam clearly contributes to the oxidation of the Al, the fact that there is oxidized Al when the beam strikes a new spot on the sample shows that there is significant oxidation of the Al even when the beam has only been on the new spot for several seconds. Thus, the oxidation of the Al is a result of the interactions between the Al and the oxide layers, and not only a result of the beam effect.

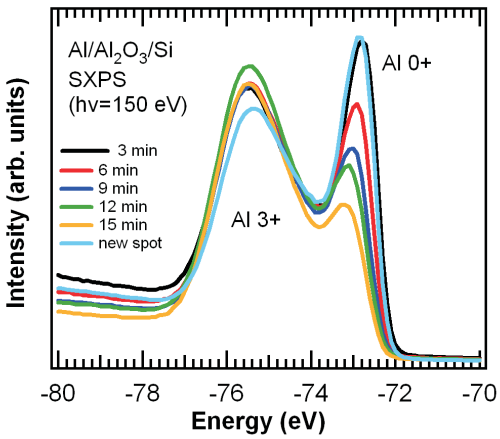

Figure 4.25: SXPS measurement of Al $2p$ level from $Al/Al_2O_3/Si$ showing that beam exposure contributes to the oxidation of the Al overlayer, and that a new spot has the original ratio of metallic and oxidized Al.

The behavior of Ti overlayers bears some resemblance that of Ru overlayers and to that of Al overlayers. Fig. 4.26(a) and (b) show the SXPS spectra of Ti $3p$ from $Ti/HfO_2/Si$ and $Ti/Hf_{0.7}Si_{0.3}O_2/Si$, respectively. In both of these figures the Ti $3p$ feature in the spectra from the high Ti coverage surfaces has a peak at $\sim$ -34 eV, which is in the range of the established binding energy for the Ti $3p$ from metallic Ti.[96] For the sake of comparison, the Ti $3p$ core level from Ti in the 4+ oxidation state has a binding energy of $\sim$38 eV.[97]

The spectra in Fig. 4.26(a) and (b) show that the shape of the Ti $3p$ changes gradually as the thickness of the layer increases, becoming narrower for thicker films. The width of the Ti $3p$ feature at lower coverages in Fig. 4.26 suggests that the Ti overlayer has some interaction with O at these coverages, and becomes more Ti rich at higher coverages. As the evolution of the Ti $3p$ does not suggest a completely metallic film, neither does it suggest the formation of a stoichiometric TiO_2 layer. We interpret

the Ti 3p feature to show that the Ti film is a dilute Ti-O_x alloy, which becomes slightly more Ti rich as the distance above the HfO_2 film increases. An alloy of this kind has been observed in an medium energy ion scattering study of the Ti/HfO_2/Si system.[98] Thermodynamic calculations were also presented in this study by Goncharova *et al.* that showed that the Ti-O_x alloy is stable at room temperature.

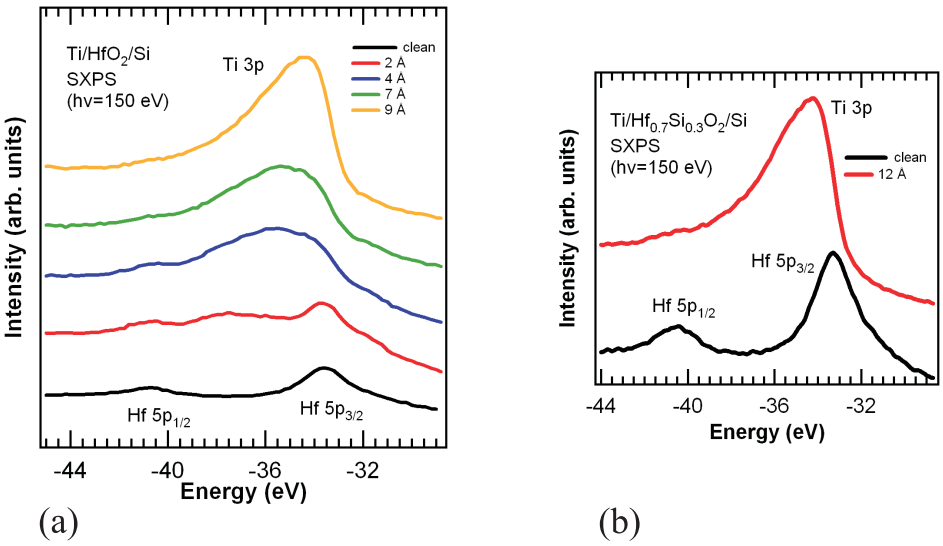

Figure 4.26: SXPS measurement of Ti 3p level from (a)HfO_2/Si and (b)$Hf_{0.7}Si_{0.3}O_2$/Si metallized with Ti.

By this interpretation, the interfaces between the Ti-O_x alloys and underlying oxide films are chemically abrupt. These chemically abrupt interfaces can be correlated with a trend of good agreement between the experimental and IGS CBO values. Thus, through the correlations we observe for the Ru/oxide, Al/oxide and Ti/oxide systems, we can draw the conclusion that the IGS model is a good predictor of the metal-oxide CBO values for cases where there is a chemically abrupt metal/oxide or metal rich alloy/oxide interface.

4.10 Effect of Metal Overlayers on the Composition of Oxide and Interfacial SiO_2 layers

The evolution of the core level lineshapes from constituents of the underlying oxide film and interfacial SiO_2 layers that occurs during sequential metallization provides

additional insight into the movement of O within the stack. We were able to observe the Si $2p$ core level spectra from Si in the interfacial layer (IL) in SXPS spectra of samples where the oxide overlayers were 20 Å or less in thickness. For samples where the oxide overlayer was 25 Å or greater, the Si $2p$ core level from the IL was too strongly attenuated to be analyzed.

We concluded in the previous section that the Ru overlayer is metallic. Thus, we do not expect the HfO_2 film on which it is deposited to be reduced by the metal overlayer. This expectation is confirmed by the spectra of Hf $4f$ levels from clean HfO_2/Si and from Ru(10 Å)/HfO_2/Si, shown in Fig. 4.27(a). In this graph, the spectrum from the Ru covered surface has been shifted by -0.5 eV to align the core levels in each spectrum. The Hf $4f$ levels do not change shape after the Ru has been deposited, indicating that the stoichiometry of the HfO_2 film is not altered by the Ru layer. Fig. 4.27(b) shows the SXPS spectrum of the Si $2p$ level from the IL for various coverages of Ru. A linear approximation to the background has been subtracted from these spectra, they have been normalized with respect to the maximum peak intensity, and they have be shifted in order to align the peaks. Though it is not shown in this graph, it is interesting to note that the Si $2p$ feature shifts upwards in energy by 0.8 eV with Ru metallization, which is greater than the upward shift in energy of 0.5 eV that the Hf levels undergo. Fig. 4.27(b) shows that the Si $2p$ core level does not change shape with increasing Ru coverage, from which we conclude that the stoichiometry of the IL is not changed by the Ru metal overlayer.

While the Ru overlayer does not reduce the HfO_2 layer, it does cause partial reduction of the SiO_2 and Al_2O_3 thin films. Fig. 4.27(c) and (d) show the Si $2p$ core level from Ru/SiO_2/Si and the Al $2p$ core level from Ru/Al_2O_3/Si, respectively, where a linear approximation to the background has been subtracted and the spectra have been shifted to align the peaks of the core levels. The Si $2p$ core level from SiO_2, can be seen to broaden on the low binding energy side as the thickness of Ru the layer on SiO_2/Si increases, indicating some reduction of the SiO_2 layer. By subtracting the Si $2p$ lineshape for the clean surface from that for the 13 Å Ru covered surface, we find that 10 % of the Si in SiO_2 sampled by the measurement is in an oxidation state lower

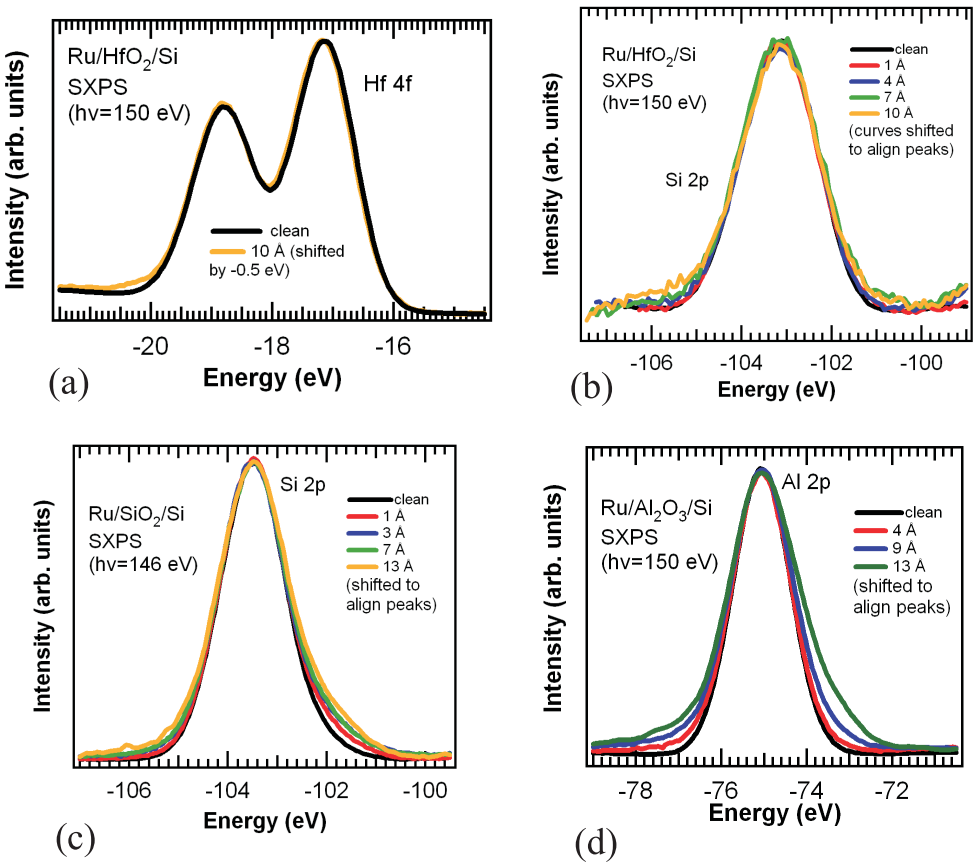

Figure 4.27: SXPS measurement of the (a)Hf 4f and (b)Si 2p levels from HfO_2/Si metallized with Ru, the (c)Si 2p level from SiO_2/Si metallized with Ru, and the (d)Al 2p level from Al_2O_3/Si metallized with Ru.

than 4+. Based on the observation by Rochet *et al.* that the oxidation states of the Si 2p core level between 4+ and 0 are all approximately 0.9 eV apart, our analysis shows that the 10 % of the Si in the SiO_2 is either in the 3+ or 2+ oxidation states.[93] The partial reduction of the SiO_2 is presumably due to movement of O into the Ru film. This movement of oxygen into the Ru film does not significantly change the shape of the Ru 4p feature, however, reinforcing the minimal nature of the reduction of the oxide. Thus, the Ru/SiO_2 interface can still be considered a chemically abrupt metal-oxide interface.

The Ru layer also partially reduces the Al_2O_3, as can be seen in the change in shape of the Al 2p core level in Fig. 4.27(d). Subtracting the Al 2p lineshape for the clean surface from that for the 13 Å covered surface shows that 18 % of the Al_2O_3 sampled

has been reduced from the 3+ oxidation state. Assuming that the oxidation states of the Al $2p$ core level between 3+ and 0 are equally spaced in energy, 18 % of the Al in the Al_2O_3 layer is in the 2+ and 1+ oxidation states. As with the Ru/SiO_2 interface, the shape of the Ru $4p$ feature for $Ru/Al_2O_3/Si$ does not noticeably change with increasing Ru thickness, suggesting a small degree of O transfer into the Ru film. Thus, we hold to the conclusion that, to a good approximation, the Ru/Al_2O_3 is a chemically abrupt metal-oxide interface.

For systems with Al overlayers, the clear oxidation of the Al overlayer, as shown in Fig. 4.24(a), (b) and (c), raises the question of the source of the O in the Al overlayer. The Al evaporation sources were thoroughly outgassed the vacuum chambers at Rutgers and the NSLS so that the pressure during Al deposition was less than 3×10^{-9} T in both vacuum chambers. Fig. 4.28 shows the Auger electron spectroscopy (AES) spectra from clean and Al covered Si. In the AES spectrum from Al/Si, the Al LVV signal can be seen at an energy of ~70 eV. A small O signal, due to the KVV Auger decay, can also be seen at an energy of ~505 eV. The small intensity of the O signal shows that the Al source deposited mostly pure Al, with a trace of O contamination. It should be noted that the the AES sensitivity of the O decay is greater than that of the Al decay, and that AES measurement itself also contributes some O to the surface. The high level of purity of the Al source suggests that the O in the Al layer must have come from the either oxide overlayer or the IL.

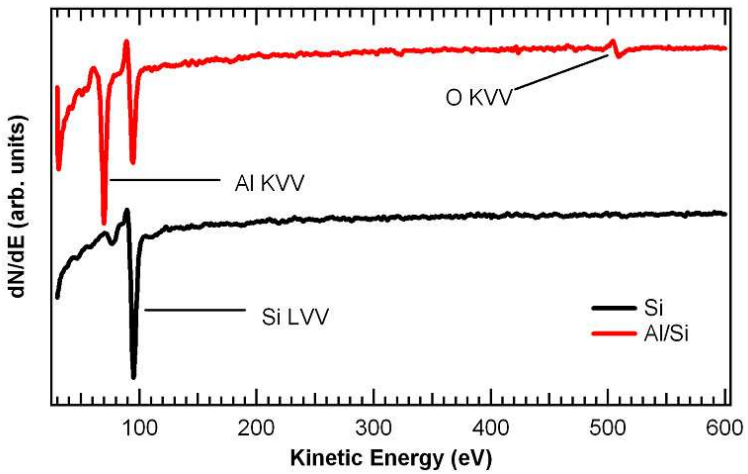

Figure 4.28: AES spectrum from Si and Al/Si.

The SXPS spectrum of the Hf $4f$ core level from Al/HfO_2/Si, shown in Fig. 4.29(a), demonstrates that the shape of this feature does not change greatly with increasing Al coverage. A small increase in intensity can be observed, however, between -16 eV and -17 eV, indicating that a small fraction ($\sim$ 1%) of Hf has been reduced. Fig. 4.29(b) shows the Si $2p$ core level from the IL. It is clear that this feature becomes broader for higher coverages of Al, with greater intensity occurring at lower binding energies. The evolution of the Si $2p$ core level is a clear indication of the reduction of the SiO_2 in the IL. The feature centered at $\sim$-99 eV in Fig. 4.29(b) shows that some Si was reduced to the Si 0+ oxidation state.[64, 93] These observations lead to the conclusion that the IL was the major source of O contributing to the formation of the Al_2O_3 interfacial layer.

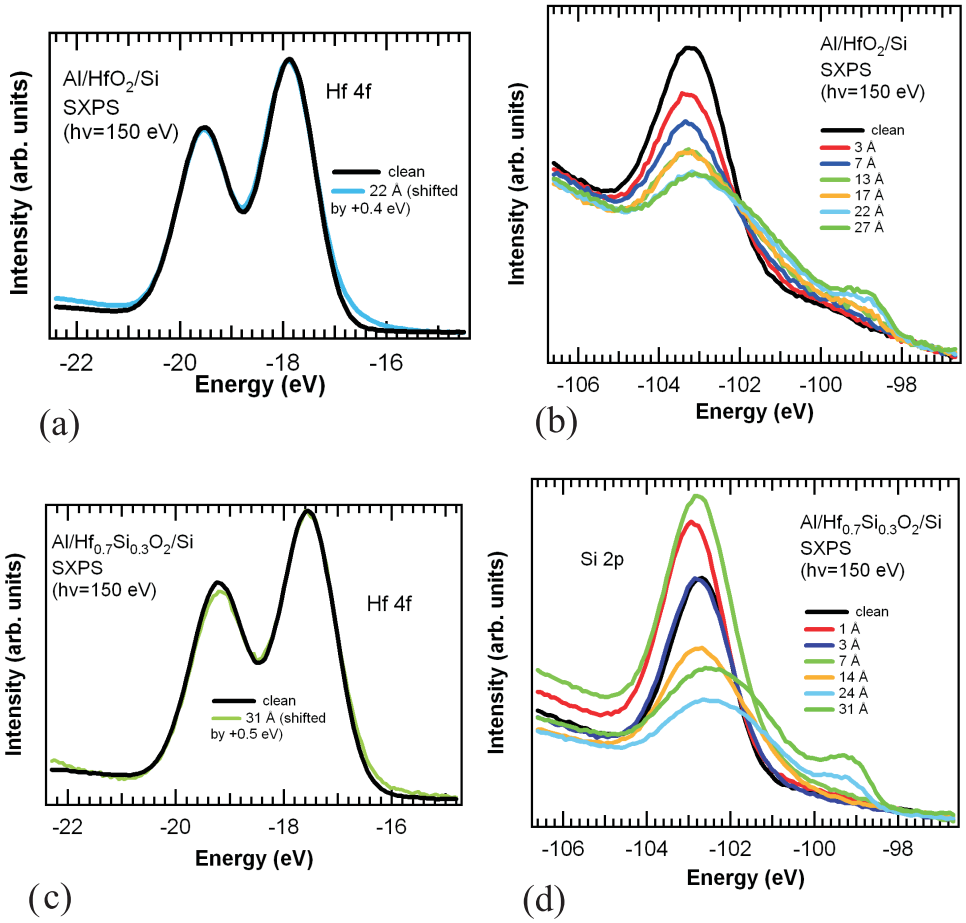

Figure 4.29: SXPS measurement of the (a)Hf $4f$ and (b)Si $2p$ core levels from HfO_2/Si metallized with Al. SXPS measurement of the (c)Hf $4f$ and (d)Si $2p$ core levels from $Hf_{0.7}Si_{0.3}O_2$/Si metallized with Al.

The analysis of O movement is similar for Al/$Hf_{0.7}Si_{0.3}O_2$/Si. The SXPS spectra of the Hf $4f$ level from Al/$Hf_{0.7}Si_{0.3}O_2$/Si, displayed in Fig. 4.29(c), show that the $Hf_{0.7}Si_{0.3}O_2$ is not reduced greatly by the Al overlayer, though the percentage of the Hf that is reduced is slightly higher (∼2-3 %) than it was for the HfO_2 in the Al/HfO_2/Si. The Si $2p$ core level spectra from Al/$Hf_{0.7}Si_{0.3}O_2$/Si, shown in Fig.4.29(d), indicate by the change in shape that occurs with increasing Al coverage that the SiO_2 in the IL was significantly reduced. This reduction, in turn, provides O to the Al overlayer.

Ti is similar to Al in that it is a low work function metal that is highly reactive, with a high tendency to give up electrons to oxidizing constituents. In this sense, it is interesting to compare the spectra from Al and Ti overlayers on nominally identical samples. From the analysis of the Al $2p$ and Ti $3p$ core levels from each of these metals on HfO_2/Si, we observed that the an interfacial Al_2O_3 layer formed between the Al and HfO_2 in the Al/HfO_2/Si system, while a dilute Ti-O_x alloy formed above the HfO_2 layer in the Ti/HfO_2/Si system.

The SXPS spectra of Hf $4f$ levels from the clean and 9 Å Ti covered HfO_2/Si system are shown in Fig. 4.30(a). The similar shape of the core levels in these spectra indicate that there is negligible reduction of the HfO_2 layer by the Ti overlayer. In contrast, the SXPS spectra of the Si $2p$ level from the IL, shown in Fig. 4.30(b), reveal that the composition of the IL is significantly altered as the Ti coverage increases. The first observation that can be made from these spectra is that the Si $2p$ peak shifts upwards in energy with increasing Ti coverage. This shift may be electrostatic in nature, as the shape of the feature is relatively consistent. This shift is also consistent, however, with reduction of the IL. A third possible explanation is that the shift has both electrostatic and chemical origins. For the highest coverage of Ti, it is clear from the low binding energy intensity in the Si 2p core level that the SiO_2 IL is strongly reduced. Thus, as with the Al overlayer in Al/HfO_2/Si, the Ti overlayer has the effect of reducing the SiO_2 IL in Ti/HfO_2/Si. The difference, however, is that the O from the SiO_2 layer contributes to the formation of an Al_2O_3 interfacial layer in Al/HfO_2/Si, whereas it goes into a Ti-O_x alloy in Ti/HfO_2/Si.

The analysis of the SXPS spectra of the Hf $4f$ and Si $2p$ core levels from the

$Ti/Hf_{0.7}Si_{0.3}O_2/Si$ sample, shown in Fig. 4.30(c) and (d), respectively, is similar to that for the core levels from $Ti/HfO_2/Si$. The Hf $4f$ core levels from clean and 12 Å Ti covered surfaces show a strong similarity in shape, indicating a relatively unchanged stoichiometry of the $Hf_{0.7}Si_{0.3}O_2$ film. A minor change in shape between these two spectra in the region of -17 eV to -15 eV, however, show a low level of reduction in the Ti covered film. Again, the Si $2p$ core level is greatly broadened by the deposition of the Ti overlayer, indicating the reduction of the IL. The O from the interfacial layer is presumably taken into the metal overlayer. Though we only deposited one, thicker Ti layer on $Hf_{0.7}Si_{0.3}O_2/Si$, the similarity of the Ti $3p$ spectra from Ti(9 Å)/HfO_2/Si and Ti(12 Å)/$Hf_{0.7}Si_{0.3}O_2$/Si, shown in Fig. 4.26(a) and (b), respectively, suggest the formation of a Ti-O_x alloy in both systems.

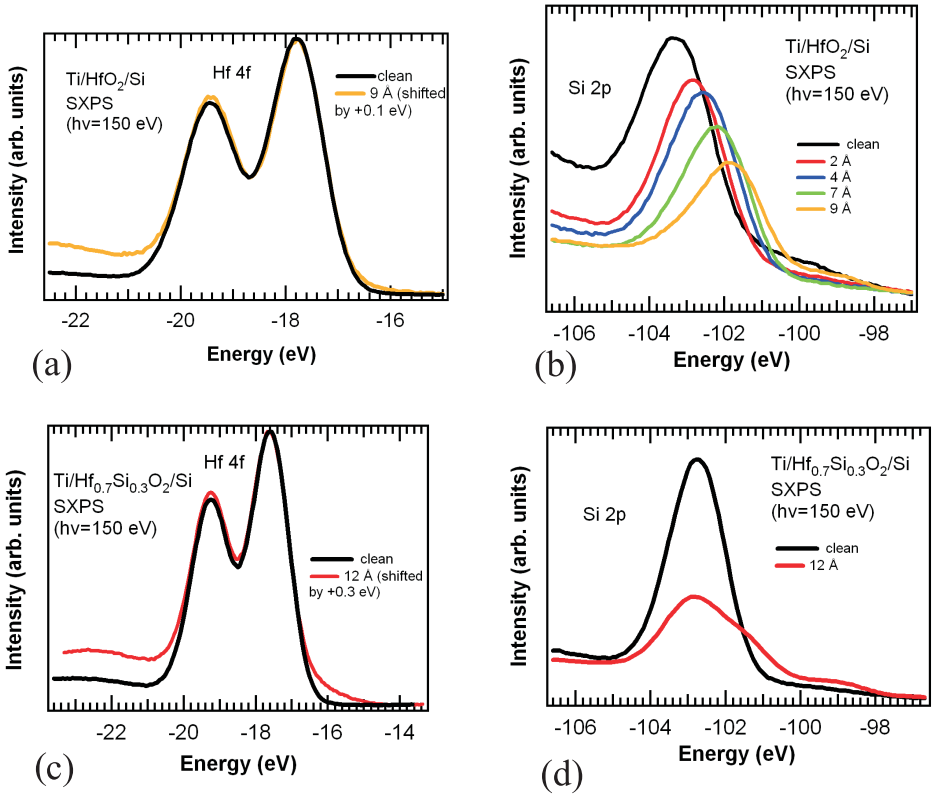

Figure 4.30: SXPS measurement of (a)Hf $4f$ and (b)Si $2p$ core levels from HfO_2/Si metallized with Ti. SXPS measurement of (a)Hf $4f$ and (b)Si $2p$ core levels from $Hf_{0.7}Si_{0.3}O_2/Si$ metallized with Ti.

4.11 Discussion of IL Reduction in Al/HfO_2/Si and Ti/HfO_2/Si

Two investigations of the reduction of the SiO_2 IL in Ti/HfO_2/Si stacks have been reported. The first study, performed by Stemmer *et al.*, involved preparing M/HfO_2/Si stacks, where the HfO_2 layers were 36 Å thick, and the metal (M) layers were Pt, Ti and Al.[91] These samples were annealed at 300°C for 30 min. in an environment of 96% N_2 and 4 % H_2. Transmission electron microscopy (TEM) was used to image cross sections of these samples to observe the composition of layers. The TEM images showed that the IL layer was made much thinner, if not removed completely, for a Ti/HfO_2/Si stack. For the Al/HfO_2/Si and Pt/HfO_2/Si stacks, the IL thickness appeared to be the same.

The results of this study agree with the results we found for Ti/HfO_2/Si system in that we also observed the reduction of the SiO_2 IL. The results for the Al/HfO_2/Si system from Stemmer *et al.* differ from ours in that we observe reduction of the SiO_2 IL and they do not. The spatial resolution of the TEM images (2.4 Å) taken by Stemmer *et al.* makes it difficult to conclude with certainty, however, that the SiO_2 IL is not reduced at all for the Al/HfO_2/Si stack. Also, the thinner HfO_2 films in used in our study (15 Å), may cause the SiO_2 IL to be more readily reduced by an Al overlayer.

Stemmer *et al.* also performed capacitance-voltage (C-V) and gate leakage current-voltage (I-V) measurements on the MOS stacks. From the C-V measurements they found that the Al/HfO_2/Si stack had the lowest capacitance and the Ti/HfO_2/si stack had the highest capacitance *eot*. The low capacitance of the Al/HfO_2/Si stack is consistent with the existence of both Al_2O_3 and SiO_2 interfacial layers. The high capacitance of the Ti/HfO_2/Si stack is consistent with the reduction of the SiO_2 interfacial oxide. The I-V measurements, where the stack was biased for electron injection from the metal, showed that the Al/HfO_2/Si stack had a lower leakage current across the oxide for a given voltage than did Ti/HfO_2/Si. This is also consistent with the existence of Al_2O_3 and SiO_2 interfacial layers in the Al/HfO_2/Si stack, as both of these layers have large band gaps and would help to resist the flow of current. The stack with the Pt gate had the lowest current at a given voltage due to a greater metal-oxide CBO.

A second study of the reduction of the SiO_2 IL in Ti/HfO_2/Si was performed by Goncharova *et al.*[98] This study involved depositing Ti on HfO_2/Si samples and determining the depth profile of the stack by medium energy ion scattering (MEIS). The authors report that the SiO_2 IL was not significantly reduced by Ti before the sample was annealed. Annealing to ∼300°C in vacuum, however, resulted in the reduction of the IL, as well as incorporation of Si into the lower region of the HfO_2 film and incorporation of O into the Ti overlayer. Our results differ from these results in that we observe IL reduction for a Ti/HfO_2/Si stack before it has been annealed. This difference in results may be attributed to a difference in the thickness of the HfO_2 layers used in our respective measurements, as the HfO_2 films measured by Goncharova *et al.* were 30 Å thick and those that we measured were 15 Å thick.

4.12 Metal-Oxide Band Offset Results from the Literature

In this section, I will compare metal-oxide CBO values from the literature to the CBO values that we measured and discuss the comparison. A major technique used to measure the metal-oxide CBO is internal photoemission (IntPE). In this technique, monochromatic light is incident on an MOS stack that has a voltage applied across it. The energy of the photon beam is varied, and the current is measured as a function of photon energy. To a good approximation, the photon energy of the onset of current corresponds to the energy of the barrier height for electrons. In order to measure the CBO for the metal-oxide interface, the metal should be negatively biased with respect to the semiconductor.

Afanas'ev *et al.* have measured the metal-oxide band offsets with IntPE for a number of metal-oxide combinations on Si substrates, though the only metal they used in common with us was Al.[99] Four of their reported CBO values are shown in Table 4.2, along with CBO values reported in this chapter for the same systems, as well as the CBO values calculated with the IGS model. A trend can be observed that, with the exception of the CBO for Al/SiO_2, the CBO values determined by IntPE are greater than those that we measured and those calculated with the IGS model, in some cases by 1.0 eV or more.

metal/oxide	CBO (eV) (IntPE)	CBO (eV) (this work)	CBO(eV) (IGS model)
Al/HfO_2	2.5	1.5	1.9
Al/SiO_2	3.2	3.5	3.0
Al/Al_2O_3	2.9	2.0	2.0
Au/HfO_2	3.7	—	2.4

Table 4.2: Experimental and theoretical values for the metal-oxide CBO.

In the work of Afanas'ev *et al.*, no reference is made to the difference between the values that they measure and the values predicted by the IGS model.[99] As was discussed above, the IGS model should not be expected to accurately predict CBO values for systems that do not have a chemically abrupt interface such as Al/HfO_2 and Al/SiO_2, so the discrepancy between the IGS CBO values for these systems and the IntPE CBO results is not a striking result. The difference of 0.9 eV between the IGS and IntPE results for Al/Al_2O_3, and the difference of 1.3 eV between the IGS and IntPE results for Au/Al_2O_3, however, are in indication that IntPE measures CBO values that are overly large.

Another technique that has been used to determine metal-oxide CBO values is the capacitance-voltage (C-V) measurement. The traditional way to use C-V measurements to determine the metal-oxide band offsets in MOS stacks with SiO_2 gate oxides is to measure the C-V curve for a number of stacks that are identical except for the thickness of the SiO_2 layer. The flatband voltage (V_{fb}) can be extracted from each of these measurements and plotted vs. the thickness of the SiO_2 layer (t), according to the equation for the flatband voltage, equation 4.3. In this equation, Φ_{ms} is the metal-semiconductor work function difference, Q is the density of fixed charge at the SiO_2/Si interface and ε is the dielectric constant of SiO_2. It is common to omit the term for the bulk charge density from this expression based on the assumption that the bulk charge density is low and does not contribute strongly to the flatband voltage.

$$V_{fb} = \Phi_{ms} - \frac{Q}{\varepsilon}t \tag{4.3}$$

By performing a linear fit on the V_{fb} vs. t data points and extrapolating to t=0, a value for the metal-semiconductor work function difference is found, from which the

metal work function can be determined using the value of the semiconductor work function. This value of the metal work function can be considered an effective work function, as defined in the IGS model discussion given Chapter 1, Section 6, because it includes the effect of the interface. Subtracting the electron affinity from the effective work function gives the metal-oxide CBO.

The traditional C-V method of finding the metal-oxide CBO is more prone to error when applied to MOS stacks with high-κ oxides because the flatband equation becomes more complicated. The full method for finding the metal-oxide band offsets from a high-κ MOS stack is given by Rashmi *et al.*[89] In general, this method involves performing C-V measurements on two sets of high-κ MOS stacks: one in which only the thickness of the high-κ layer varies, and the other in which only the thickness of the SiO_2 IL varies. Rashmi *et al.* have used this method to find the effective work function of 4.5 eV for a Ru_xTa_{1-x} (x$\geq$0.5) alloy.[89]

One expression for the flatband voltage of a high-κ MOS stack is given in equation 4.4. In this equation, Q_1 and Q_2 are the fixed charge densities at the high-κ/SiO_2 and SiO_2/Si interfaces, respectively, and ε is the dielectric constant of SiO_2. The term *eot* stands for effective oxide thickness, which was also discussed in Chapter 1, Section 1. The *eot* of a high-κ layer is the thickness that an SiO_2 would have to have to give the same capacitance. In equation 4.4, *eot1* is the effective oxide thickness of the high-κ layer and *eot* is the total effective oxide thickness of the stack. It should be noted that the terms for the fixed charge in the bulk of the oxide layers are neglected in this equation.

$$V_{fb} = \Phi_{ms} + \frac{Q_1}{\varepsilon} eot_1 - \frac{(Q_1 + Q_2)}{\varepsilon} eot \tag{4.4}$$

Of the terms in this equation, the flatband voltage and *eot* are both known from the C-V measurements, and the eot_1 can be found from a measured value of the thickness of that layer and a previously measured dielectric constant. Similar to the traditional C-V method for finding the metal-oxide CBO, the flatband voltage is plotted vs. the *eot* for each sample. Making one further assumption, where $Q_1 \gg Q_2$, allows a value for Q_1 to be extracted from the the slope of a linear fit to the V_{fb} vs. *eot* points. Once a

value for Q_1 is known, it can be used to calculate Φ_{ms}. As discussed above, this value can be used to find the effective metal work function, which, in turn yields a value for the metal-oxide CBO once the oxide electron affinity is subtracted from it.[100]

Using the traditional C-V method, Misra *et al.* found an effective work function for Ru of 5.0 eV for the Ru/HfO_2/Si system. Subtracting the HfO_2 electron affinity that we measured (2.5 eV) from this effective work function gives an Ru/HfO_2 CBO of 2.5 eV, which differs the value we measured (2.4 eV) by only 0.1 eV. Using the more advanced C-V method for high-κ MOS stacks, Majhi *et al.* found an effective work function of 4.6 eV for Ru in the Ru/$HfSiO_2$ system.[101] Using the electron affinity that we measured for $Hf_{0.7}Si_{0.3}O_2$ of 2.8 eV, the CBO is 1.8 eV, which is 0.6 eV lower than the CBO value we measured for Ru/$Hf_{0.7}Si_{0.3}O_2$. Yang *et al.* used both the traditional and advanced C-V methods to find effective work functions for Ti in Ti/HfO_2/Si. They measured an effective work function of 4.2 eV by the traditional method and an effective work function of 4.4 eV by the advanced method.[100] The former of these values corresponds to a Ti/HfO_2 CBO of 1.7 eV and the latter corresponds to a Ti/HfO_2 CBO of 1.9 eV, both in excellent agreement with the value we measured (1.8 eV). Thus, metal-oxide CBO's determined from the C-V method agree well with the values we measured for the cases of Ru/HfO_2 and Ti/HfO_2, but not for Ru/$Hf_{0.7}Si_{0.3}O_2$.

4.13 Conclusions

We have measured the metal-oxide CBO for various metal-oxide combinations on Si through UPS, IPS and SXPS spectroscopy. The metal-oxide CBO values we measured compare well with CBO values calculated with the IGS model for samples metallized with Ru and Ti, but not for samples metallized with Al. We have correlated the good agreement between experimental and theoretical CBO values with abrupt metal-oxide interfaces. In contrast, the poorer experimental and theoretical agreement occurs for samples where an Al_2O_3 interface layer forms between the Al layer and the original oxide overlayer, which undermines the validity of the IGS value. A comparison with literature values for metal-oxide CBO's shows that our experimental values are smaller, in general, than those determined by internal photoemission, and are in agreement with

those determined by the C-V method in 2 of 3 cases. We have also observed that the deposition of an Al or a Ti layer has the effect of reducing the SiO_2 interfacial layer for HfO_2(15 Å)/Si and $Hf_{0.7}Si_{0.3}O_2$(20 Å)/Si samples, while having a minimal chemical effect on the high-κ oxide layers.

Chapter 5

Energy Level Alignment of Organic Dye/Oxide Systems

5.1 Introduction: Solar Cells

Solar cells, devices that convert sunlight into electricity, have been the subject of intense study in recent years due to worldwide efforts to find energy sources that are renewable and do not add greenhouse gases to the atmosphere. The core of a traditional solar cell is a Si p-n junction, the band diagram of which is shown in Fig. 5.1. When an electron near the junction absorbs a photon, an electron-hole pair is created, and the electron and hole are separated by the electric field in the region of the junction, as indicated in Fig. 5.1. The electric current is the result of electrons and holes moving through the electric circuit to recombine.

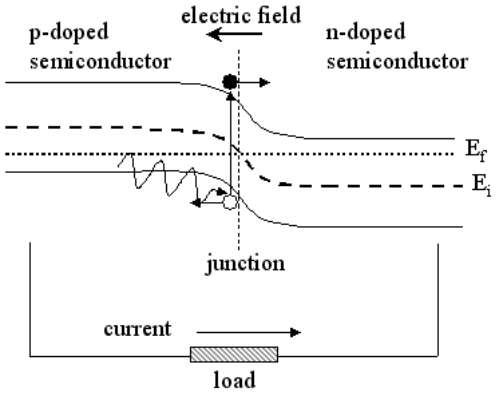

Figure 5.1: Band diagram of Si pn junction solar cell.

The major criterion on which solar cells are evaluated is efficiency (η). A general expression for the efficiency of a solar cell is given in equation 5.1, where P is electrical power of the solar cell, I is the irradiance of incident light ($\frac{W}{m^2}$), and A is the surface area of the cell. Si solar cells can be made of either single crystal, polycrystalline or amorphous Si, which have demonstrated efficiencies up to 25%, 18% and 13%,

respectively.[102] The widespread use of Si solar cells, however, is limited by high costs of production, particularly for single crystal and polycrystalline solar cells. Dye sensitized solar cells (DSSC's) are a lower cost alternative to Si solar cells. DSSC's have shown efficiencies as high as 10%, making them an attractive alternative to Si solar cells when their reduced cost is taken into account.[103]

$$\eta = \frac{P}{IA} \tag{5.1}$$

5.2 Introduction: Dye Sensitized Solar Cells

The essential difference between a traditional solar cell and a DSSC is that in the former, the electron-hole pair is created and separated within the semiconductor, and in the latter, the electron-hole pair is created on a dye molecule that is adsorbed on the surface of a semiconductor, and the electron is injected into the semiconductor. The following description of a DSSC will expand on this brief description.

The body of a DSSC is a multi-layer structure, as shown in Fig. 5.2. The bottom layer consists of glass plate coated with a transparent conducting oxide (TCO), which is typically F-doped SnO_2. On top of this is a semi-porous layer of TiO_2 nanoparticles, known as the electrode. The TiO_2 nanoparticles are coated on the majority of exposed surfaces with a mono-layer of dye molecules, and immersed in an electrolyte solution, which is contained in a sealed compartment. The top layer of the body of a DSSC is another glass plate, the underside of which is coated with TCO and a layer of Pt. The Pt layer, which is in contact the electrolyte, is known as the counter electrode. The electrode and counter electrode are connected to an electrical circuit.

A DSSC converts light into electricity by, first, allowing photons in the visible (1.5-3.0 eV) and near UV range to enter the body of the cell through the TCO covered glass substrate, as shown in Fig. 5.2. These materials, along with TiO_2, do not absorb light in this energy range due to their large band gaps, as shown in the band diagram of a DSSC in Fig. 5.3. If a photon encounters a dye molecule, it may be absorbed if its energy equals the energy difference between the highest occupied molecular orbital

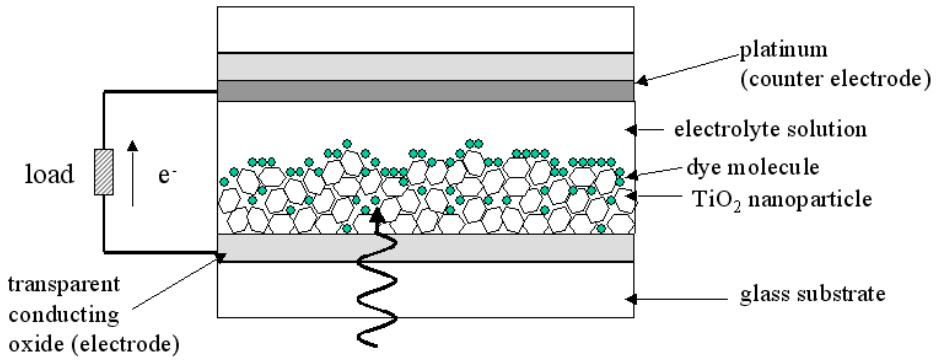

Figure 5.2: Schematic diagram of a dye sensitized solar cell.

(HOMO) and the lowest unoccupied molecular orbital (LUMO) of the dye molecule, the HOMO-LUMO gap. In reality, the HOMO and the LUMO are not sharp states, but have some energy width, which makes for a broad maximum in the optical absorption spectrum of commonly used dye molecules.[104, 105, 106]

Absorption of a photon by a dye molecule results in the creation of an electron-hole pair. The excited electron is transferred into the TiO_2 conduction band, and the hole is filled with an electron from an anion in the electrolyte solution. The electronic level alignment between the TiO_2, the dye molecule and the electrolyte is critical to both of these events. The LUMO of the dye molecule must be above the TiO_2 conduction band minimum (CBM), as shown in Fig. 5.3, for the electron to make the transition to the TiO_2 conduction band. Also, the ionization potential of the electrolyte redox couple (I_3^-/I^-) must be above the HOMO of the dye molecule for an electron from an anion in the electrolyte to spontaneously fill the hole in the dye molecule.

The transfer of the electron from the dye LUMO to the TiO_2 conduction band, and the filling of the hole in the dye HOMO by the electrolyte both take place on the order of femtoseconds, which is essential for attaining low levels of electron-hole recombination.[107, 108] The electron in the TiO_2 will then move to the TCO and through the circuit to the counter electrode, where it is donated back to an oxidized anion in the electrolyte solution. The chemical reaction for the redox couple (I^-/I_3^-) to donate electrons to the dye molecule is $I_3^- + 2e^- \rightarrow 3I^-$, and to receive electrons back from the counter electrode is $3I^- + 2h^+ \rightarrow I_3^-$.[103]

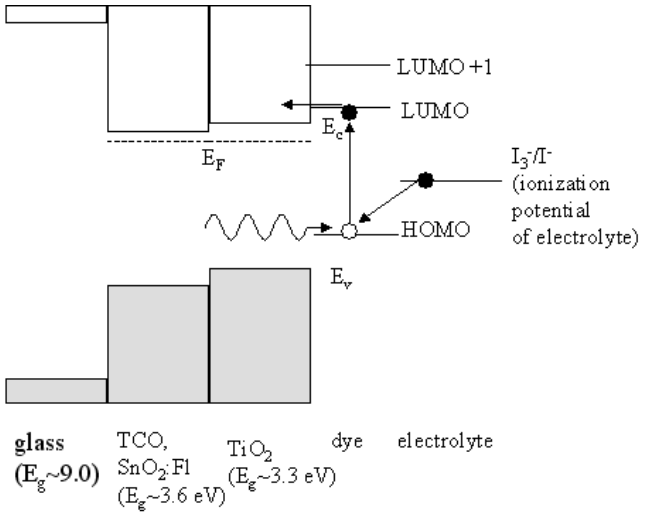

Figure 5.3: Band diagram of a dye sensitized solar cell.

As we demonstrated in our studies of MOS structures in Chapters 3 and 4, we can use UV photoemission spectroscopy (UPS) and inverse photoemission spectroscopy (IPS) in the same vacuum chamber to measure the energies of the electronic levels in the band diagram. For the dye/TiO_2 system, we have measured the TiO_2 band gap, the HOMO-LUMO gap of the adsorbed dye molecule, the energy difference between the HOMO and the TiO_2 valence band maximum (VBM), as well as that between the the LUMO and the TiO_2 CBM. Thus, we have fully characterized the electronic structure of the dye/TiO_2 system.

5.3 Properties of the TiO_2 Film and Dye Molecule

The primary purpose for using a TiO_2 film composed of nanoparticles is that it has a semi-porous structure with a high surface area. The semi-porous structure allows far more dye molecules to be absorbed than would be adsorbed on a flat film. The thickness of the TiO_2 film is typically ~10-15 μm, which can support enough dye to absorb all of the photons of a sufficient energy that enter it. TiO_2 films are commonly composed of 20-40 nm anatase nanoparticles that are sintered together with neighboring nanoparticles. [103, 109] These sintered nanoparticles also scatter light, giving it a longer path length within the film, and thus, a higher probability of being adsorbed.

The TiO_2 film can be deposited by screen printing a nanoparticle-containing paste

or spin coating a nanoparticle-containing gel onto the TCO covered glass substrate. The paste or gel must then be heated to $\sim 450^{\circ}$ for 30 minutes to drive off the volatile components and stabilize the nanoparticle structure.[110] In the early development of DSSCs it was thought that nanoparticles would not be an effective electrode due to the relatively low conductivity of the film. This has proven to be false, however, for reasons that are not completely understood.[103] ZnO has also been investigated as the oxide film in DSSC's due to the high mobility of electrons in the conduction band. Efficiencies in these cells, however, are lower than those of cells with TiO_2 films.[111] ZnO nanorods have been identified as a promising form of oxide support for dye molecules because they offer high surface area and high electron conductivity due to a well ordered crystal structure.[112]

The ideal dye molecule for use in a DSSC would have a HOMO-LUMO energy gap of 1.4 eV. This energy gap would allow for the absorption of the majority of the solar spectrum, while not lowering the open circuit voltage of the DSSC, which is the potential difference between the TiO_2 CBM and the ionization potential of the electrolyte. Another important property of the dye molecule is that it should not break down during prolonged exposure to sunlight. Through the synthesizing and testing of many molecules, a highly stable molecule with a relatively small HOMO-LUMO gap was found. This molecule, known as N3, is cis-$RuL_2(NCS)_2$, where L is 2,2'-bipyridil-4,4'-dicarboxylic acid. The structure of N3 schematically shown in Fig. 5.4(a). Several studies of the bonding of N3 to TiO_2 agree that the most likely bonding configuration is one in which N3 bonds through two carboxylic acid (COOH) groups.[3, 5, 4] In bonding to the TiO_2 surface, the carboxylic acid groups lose a H atom and bond to Ti atoms of the TiO_2 surface in one of several possible configurations. The majority configuration is thought to be one where each O in the carboxylic acid group bonds to a Ti atom in what is known as a bidentate bridging configuration, shown in Fig. 5.4(b). [3] The carboxylic acid groups can also bond to the Ti atoms in a bidentate chelating configuration, as shown in Fig. 5.4(c), or in a monodentate configuration, as shown in Fig. 5.4(d).

Dye molecules such as N3 cannot be deposited onto a substrate by evaporation in

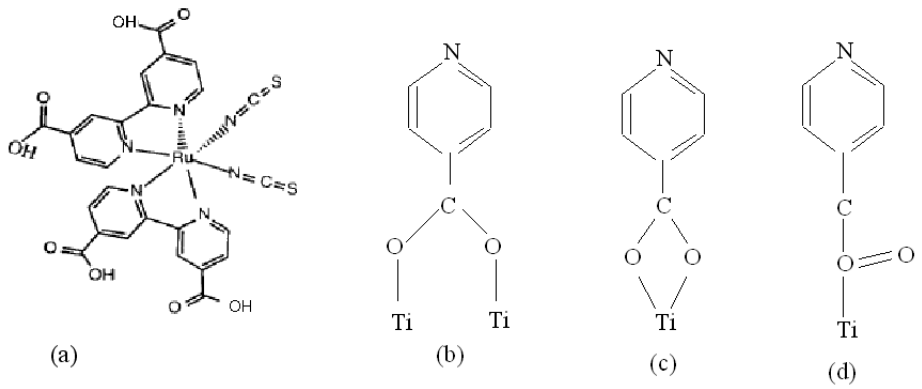

Figure 5.4: (a)Model of the N3 molecule. (b)Bidentate bridging (c)bidentate chelating and (d) monodentate bonding of N3 ligand to TiO_2.

vacuum because they are large molecules that decompose at temperatures only slightly elevated above room temperature. Therefore, they are deposited on a substrate by immersing the substrate in a solution of dye dissolved in anhydrous ethanol or acetonitrile. A nanoparticle film substrate should be left in the solution for several hours for dye molecules to adsorb on the majority of the internal surface of the semi-porous TiO_2. It is thought that the bonding of N3 to TiO_2 is self-limiting at one monolayer.[5]

5.4 Improvement of DSSCs: Dye-TiO_2 Interface

The interface between the dye molecules and the TiO_2 electrode has a great effect on the performance of a solar cell. One example of this is the recombination that occurs when an excited electron in the TiO_2 moves back across the interface and is absorbed by oxidized anion (I_3^-). This recombination is a one of the main limiting factors in DSSCs. [113] A greater understanding of the interface through detailed physical characterization will be useful in tailoring the interface to improve DSSC performance.

A strategy that has been used to inhibit recombination from the TiO_2 to the oxidized anion is to include an additive in the solution which deposits the dye. Such an additive, t-butylpyridine (TPB), has been shown to to reduce the recombination current.[108] This is attributed to occupation of bare sites on the TiO_2 surface by TBP, limiting the contact between the TiO_2 and the electrolyte. Another approach was to expose a dye covered TiO_2 film to a vapor of methylsiloxane (CH_3SiCl_3) to cover the exposed

patches of TiO_2. This treatment also reduced the rate of recombination.[114]

In an effort to study a well-controlled dye-TiO_2 interface, we have used a model substrate, single crystal rutile $TiO_2(110)$. The $TiO_2(110)$ surface has been thoroughly studied and can be prepared in a well characterized way in ultra high vacuum (UHV).[97] It has also been shown that the $TiO_2(110)$ surface can be passivated in the UHV environment by exposure to pivalic acid.[3] This passivation keeps it free from atmospheric contamination as it is transferred through the atmosphere to the dye solution. In principle, a passivated surface will allow only dye molecules to bond to it, resulting in a high quality dye-TiO_2 interface.

The following discussion briefly describes and gives some background for the work of Sasahara *et al.*, who first showed that pivalic acid could be used to successfully passivate the $TiO_2(110)$ surface, that we have followed.[3] First, a clean, well-ordered $TiO_2(110)$ is prepared by several cycles of sputtering and annealing in UHV. The model for a clean, well-ordered rutile $TiO_2(110)$ surface is shown in Fig. 5.5(a). This surface has a (1×1) structure with rows of O and Ti atoms along the [001] direction. The STM image of a $TiO_2(110)$ shown in in Fig.5.5(b), taken by Sasahara *et al.*, conforms to the structure of the model surface. In this image, the bright spots represent Ti atoms, and they form rows along the [001] direction.[3] The Ti atoms are imaged in this measurement because the tip is biased negatively with respect to the sample causing electrons to tunnel into the sample. As the low energy region of the TiO_2 conduction band is dominated by Ti $3d$ states, they are the locations where tunneling occurs.

Then, the $TiO_2(110)$ surface with pivalic acid ($(CH_3)_3CCOOH$) by exposing the prepared $TiO_2(110)$ surface to a pressure of pivalic acid gas molecules. A model of a pivalic acid molecule is shown in Fig. 5.5(c). Pivalic acid adsorbs dissociatively on the the TiO_2 surface by releasing an H atom and adsorbing as a pivalate ion ($(CH_3)_3CCOO^-$) on two Ti atoms in a bidentate bridging configuration through the carboxylic acid group, as described above for N3. The pivalate ions bond along the Ti rows in the [001] direction, as shown in Fig. 5.5(d). After they are bonded, the three methyl groups of the pivalate ions are oriented upward, away from the TiO_2 surface, where they present an unreactive shield to most other molecules.

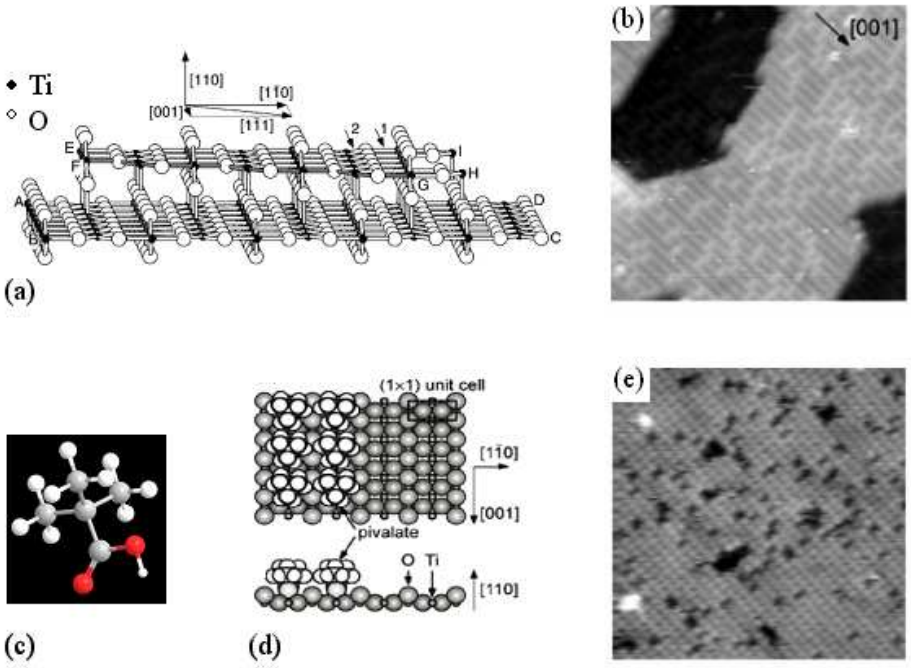

Figure 5.5: (a)Model and 20×20 nm STM image of TiO_2(110) surface. (c) Ball and stick model of pivalic acid mocule. (d)Model and (e)STM image of pivalate/TiO_2(110). (after Sasahara *et al.*[3])

Using scanning tunneling microscopy (STM), Sasahara *et al.* have shown that exposing a clean, well-ordered rutile TiO_2(110) surface to pivalic acid results in a well-ordered pivalate monolayer that matches the morphology of the TiO_2(110) surface.[3] The STM image shown in Fig. 5.5(e) is from a pivalate covered TiO_2(110) surface, where the white spots represent pivalate ions. By comparing the STM images in Figs. 5.5(b) and (e), which are both from the work Sasahara, *et al.*, it can be seen that the pivalate ions adsorb in a pattern that follows the morphology of the TiO_2(110) surface. Sasahara *et al.* have also shown that exposing the pivalate covered TiO_2(110) to the atmosphere or to pure acetonitrile solution does not significantly alter the surface. By exposing the pivalate covered TiO_2 surface to a dilute solution of N3 in acetonitrile, they were also able to image individual dye molecules on the TiO_2(110) surface.[3]

Another approach to gaining a better understanding the N3-TiO_2 interface is to investigate a simpler molecule which is representative of a key part of N3: the pyridine/carboxylic acid ligand. As mentioned earlier, the carboxylic acid ligand is thought be the linker through which N3 bonds to TiO_2.[5] It has also been shown, through

density functional calculations, that the LUMO of N3 is localized on one of the pyridine/carboxylic acid ligand that bonds to TiO_2. Fig. 5.6(a) and (b) are representations of the minimum energy structure of an N3 molecule bonded to an anatase TiO_2 cluster, as determined by the calculations of Persson *et al.*[4] The white and blue shapes represent constant energy density contours of molecular orbitals of interest. As shown in Fig. 5.6(a), the HOMO of N3 is localized on the Ru atom and on one thiocyanate (NCS) group. Fig. 5.6(b) shows that the N3 LUMO occurs along one of the pyridine/carboxylic acid ligands that bonds to TiO_2. A molecule known as isonicotinc acid (INA) consists solely of a pyridine group and a carboxylic acid group. While the properties of this molecule are not expected to be exactly the same as those of the pyridine/carboxylic acid complex in an N3 molecule, it may have similar bonding and unoccupied electronic properties. We have measured the electronic properties of INA adsorbed on two different substrates in order to compare them with the properties of N3 adsorbed on the same substrates.

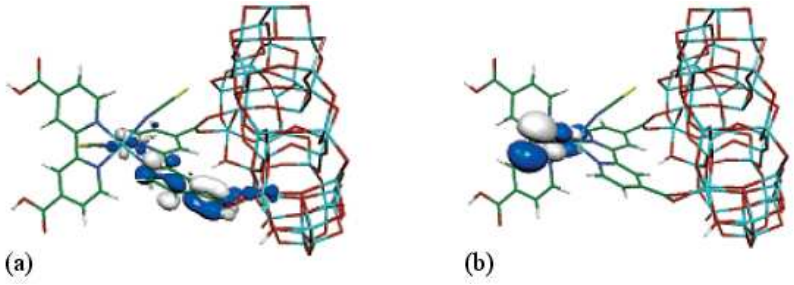

Figure 5.6: Calculated spatial distribution of the N3 (a)HOMO and (b)LUMO bonded to anatase TiO_2(101).[4]

5.5 Measurement of Energy Level Alignment

Though the energy level alignment of the N3-TiO_2 system is an important property that underlies the performance of a DSSC, this property is difficult set of quantities to measure. One approach to measuring the electronic level alignment is to use a combination of UV photoemisssion spectroscopy (UPS) and optical measurements of the HOMO-LUMO gap and the TiO_2 band gap, as employed by Snook *et al.*[106] Snook *et al.* measured the valence band spectrum of an anatase TiO_2 nanoparticle surface,

where a negative bias was applied to the sample so that the low kinetic energy edge of the spectrum could be observed, from which the vacuum level could be found. This type of UPS measurement was described earlier in Chapter 2, Section 3. Then Snook *et al.* measured the valence band spectrum from a biased N3/TiO_2 sample. In order to have a common energy scale for these two spectra, they used the assumption that the vacuum levels of these two spectra were equal. With a common energy scale, they were able to determine the alignment between the N3 HOMO (from the spectrum of N3/TiO_2) and TiO_2 VBM (from the spectrum of TiO_2). The assumption that the vacuum levels are equal for the TiO_2 surface and for the N3 surface are equal is questionable, however, as it has often been shown that adsorption of molecules on a surface changes work function of a surface.[115]

Snook *et al.* were not able to measure the unoccupied states directly, so in order to find the alignment between the N3 LUMO and the TiO_2 CBM, they added an energy gap for N3 that they measured to the energy of the HOMO, and they added a band gap taken from the literature to the energy of the TiO_2 VBM. For N3 dye, they used an optical band gap of 2.3 eV, which they measured using optical absoprtion from an N3/TiO_2 sample. For anatase TiO_2, they used an optically measured band gap of 3.2 eV.

Optical absorption band gap measurements are performed by sending monochromatic light with an energy lower than the energy gap into a sample and increasing the energy. The energy at which the material begins to absorb the light corresponds to the band gap of the material. A factor that must be considered in this type of measurement is that an electron that is excited into a low lying unoccupied state is still bound to the hole that was created with its excitation. This bound electron-hole pair is called an exciton, and the binding energy between them is the exciton binding energy.

In contrast to an optically measured band gap (optical gap), a so-called transport gap is the energy gap between the highest occupied and lowest unoccupied electronic level in a material in the absence of exciton binding energy. The relationship between the optical gap and the transport gap is that the transport gap equals the optical gap plus the exciton binding energy.[116] Thus, even if their alignment between the N3

HOMO and TiO_2 VBM were correct, their method of find the alignment between the LUMO and the CBM is prone to two criticisms. The exciton binding energies for solids are, in general, different from those of molecules, so that the alignment between the N3 LUMO and the TiO_2 CBM determined from adding the optical band gaps to the HOMO and VBM energies will, most likely, be inaccurate.[116] A second criticism is that literature value for the band gap of TiO_2 that they use may not be the same as the band gap for their sample, as the band gap for TiO_2 may be sensitive to different growth and processing conditions, as it is for high-κ oxides.

Hagfeldt *et al.* used an approach similar to Snook *et al.* to measure the energy level alignment of the N3-TiO_2 anatase nanoparticle system.[5] Rather than measuring the valence band spectrum from both a TiO_2 surface and an N3/TiO_2 surface, however, they only measured the valence band spectrum from N3/TiO_2 with UPS. From this spectrum they found the energy of the HOMO peak and estimated the energy of the VBM of the TiO_2 substrate at a point where the photoemission intensity began to increase steadily on the high binding energy side of the HOMO. This estimation is rather arbitrary. It is also prone to error on the grounds that the N3 layer may contribute states in the region of the TiO_2 VBM, which makes the estimation of the TiO_2 VBM from a spectrum of the N3/TiO_2 surface difficult.

As with Snook *et al.*, Hagfeldt *et al.* do not measure the unoccupied states directly. In lieu of this, they added a TiO_2 band gap from the literature to the VBM of TiO_2 that they estimated in order to find the CBM. To find the energy of the LUMO they measured the HOMO-LUMO gap and added it to their measured energy of the HOMO. Hagfeldt *et al.* measured the N3 HOMO-LUMO gap by determining the Incident Photon to Current Efficiency (IPCE) as a function of photon energy.[5]

In the IPCE measurement, monochromatic light is incident on a DSSC with N3 dye and a TiO_2 substrate. The energy of the light is gradually increased, and the current in the DSSC is measured as a function of photon energy. The IPCE measurements for a DSSC with N3 dye, and one for a DSSC with the so-called black dye, are shown in Fig. 5.7. Hagfeldt *et al.* interpret the peak of the IPCE curve as the energy of the peak-to-peak HOMO-LUMO gap. Another feature of the the IPCE curve is the long

wavelength (low energy) edge, which gives the energy difference between the leading edge of the HOMO and the TiO_2 CBM, as this difference defines the lowest energy photon that can cause current be generated, as long as part of the LUMO is below the TiO_2 CBM.

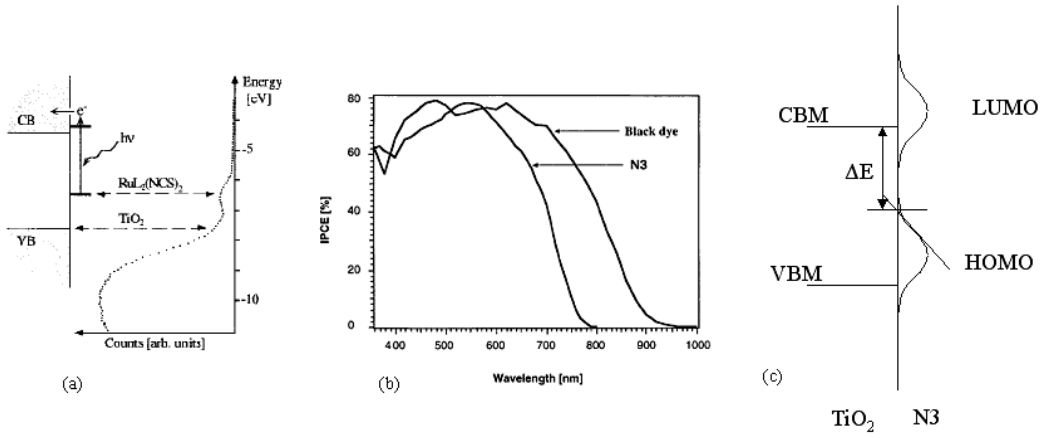

Figure 5.7: (a)UPS spectrum of N3/TiO_2. (b)IPCE vs. photon energy for a DSSC with N3 and black dye. (c)Energy diagram showing minimum photon energy needed to induce current. [5]

As shown in the two studies discussed above, photoemission can be used to directly measure the occupied density of states (DOS) of the N3/TiO_2 system. Direct measurements of the unoccupied states of materials are less commonly reported. One technique that can directly measure the unoccupied DOS of a system is X-ray absorption spectroscopy (XAS). XAS, as described in Chapter 2, Section 7, has not been used to measure the unoccupied states of N3 dye adsorbed on TiO_2, however, due to the lack of a sharp core level to serve as the absorbtion edge. Alternatively, XAS has been used in conjunction with X-ray photoemission spectroscopy (XPS) to measure both the occupied and unoccupied density of states of prototype molecules of N3 dye, isonicotinic acid (INA) and bi-isonicotinic acid (b-INA), adsorbed on rutile TiO_2(110) substrates. These molecules are thought to have similar unoccupied electronic structures to N3.[6]

A drawback of XAS is that a core hole is created when an electron is excited from the absorption edge into the conduction band. The core hole causes all of the electronic states of the molecule to relax, which lowers the energies of the states from their ground state energies, and can alter the shape of the unoccupied DOS from its ground state

shape. In the XAS measurements of Schnadt *et al.* on INA/TiO_2(110), it is clear that the energy level alignment between the LUMO of INA and the TiO_2 CBM is inaccurate, as the peak of the LUMO is nearly 1 eV below the CBM of TiO_2.[6] It is still worthwhile, however, to consider the shape of the XAS spectrum as an approximation to the ground state unoccupied DOS. The XAS spectrum for INA/TiO_2(110), reported by Schnadt *et al.*, is shown in Fig. 5.8. It has a 3 peak structure, where the low energy peak is identified as the LUMO of INA, the next highest energy peak, which has a low intensity, is identified as the LUMO+1, and the highest energy peak in the spectrum is identified as the LUMO+2.

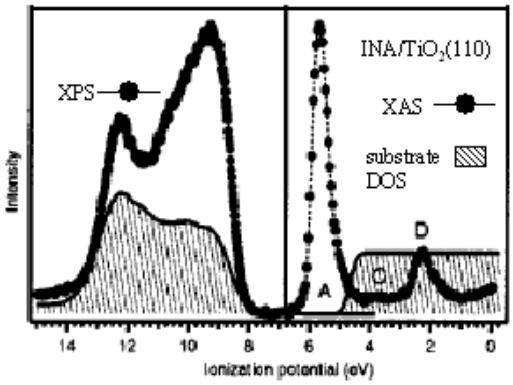

Figure 5.8: (a)XPS and XAS measurements of INA/TiO_2(110). [6]

We have used a combination of UPS and inverse photoemission spectroscopy (IPS) in the same vacuum chamber to measure the energy level alignment of the N3/TiO_2 system. By this combination of measurements, we have a direct measurement of both the occupied and unoccupied density of states of the system. As will be described in more detail later, we measured the UPS and IPS spectrum for the clean TiO_2 and the N3/TiO_2 surfaces. These spectra are initially aligned with respect to the Fermi level of each spectrum, and then, in some cases, shifted to align sharp spectral features which are indicative of band bending in the oxide substrate. Then, through a simple analysis of the UPS and IPS spectra from the clean and dye covered TiO_2 surfaces, we can extract the occupied and unoccupied DOS of the dye molecule with respect to those of the TiO_2 substrate, which gives the complete energy level alignment of the dye/TiO_2 system.

This method has several advantages over the other methods previously discussed. First, we align the energy levels from the spectra from the clean and dye covered TiO_2 surfaces with respect to the Fermi level, which is a well-defined level for both samples. Thus, we avoid the problem faced by Snook *et al.* of having to align two UPS spectra with respect to the vacuum level, a less well-defined reference level. Second, we do not have to use a TiO_2 band gap from the literature, as we can directly measure the occupied DOS. Third, we do not have to estimate the TiO_2 VBM from the UPS spectrum in an arbitrary way, as was done by Hagfeldt *et al.*, because we can refer to the spectrum from the clean oxide surface. Last, we avoid the problem inherent to XAS of introducing a core hole. A concern with IPS is that it adds an extra electron to the system. This does not have a strong effect the electronic structure of the sample, however, as long as it is drained away to ground efficiently. We observed no indication of charging in the IPS measurements from the clean and N3 covered oxide samples. Thus, our measurements of the energy level alignment of the N3/TiO_2 and N3/ZnO systems are the most complete and reliable that have been performed to date.

5.6 Experimental Details

In order to measure the alignment between adsorbate and substrate energy levels, both the clean and the adsorbate covered oxide surfaces must be measured with UPS and IPS. We measured several different adsorbate/substrate combinations. Three substrates were used: single crystal rutile $TiO_2(110)$, anatase TiO_2 nanoparticle films on FTO covered glass, and ZnO$(11\bar{2}0)$ epitaxial films grown on r-sapphire. The single crystal $TiO_2(110)$ was a model substrate that could be prepared in a controlled way and compared to results from the nanoparticle film, which is a more relevant substrate for actual DSSC's. The ZnO substrate was used for the purpose of comparison with results from TiO_2 substrates, and to take advantage of the featurelessness and low cross section of its conduction band states, as will be discussed below. The TiO_2 nanoparticle films were grown by spin coating a nanoparticle containing gel onto a FTO/glass substrate and heating at $\sim 450^\circ$ for 30 minutes. The films were $\sim$20 nm thick and composed of particles $\sim$10 nm in diameter.[117] These samples were grown by the group of D. Birnie

at Rutgers. The ZnO films were grown by MOCVD using diethyl zinc and O_2 precursors by the group of Y. Lu at Rutgers.[118]

There were two UHV chambers in which measurements were made. One chamber contained the UPS and IPS systems to measure the electronic structure, and the other housed an STM to image the surfaces. The ordered substrates, rutile $TiO_2(110)$ and $ZnO(11\bar{2}0)$/r-sapphire, were prepared in either chamber by multiple cycles of sputtering with 1 kV Ar^+ ions for 20 min., and annealing at ∼630-680°C for 10 min. The cleanliness of the samples was evaluated by Auger electron spectroscopy (AES) in both vacuum chambers, and the order of the surfaces by evaluated by low energy electron diffraction (LEED) in both chambers, as well. The nanoparticle TiO_2 substrate was prepared in UHV by annealing at 200°C for 1 hour to remove water vapor from the film.

The passivation of the surface was performed on the $TiO_2(110)$ and ZnO samples in the STM chamber. To passivate the surface, a sputtered and annealed sample was brought into a preparation chamber attached to the STM chamber, which had a base pressure of 2×10^{-9} Torr. In this chamber the sample was exposed to 1 $\times10^{-6}$ Torr of pivalic acid for 100 seconds to cover the clean surface with a layer of pivalate ions. Prior to introduction into the preparation chamber, the pivalic acid was cleaned by several freeze-thaw-pump cycles. The sample could then be returned to the main part of the STM chamber and imaged with STM to evaluate the order of the pivalate layer on the surface.

The passivated surface was then removed from the vacuum and one of two adsorbates, N3 dye or INA, was deposited by placing the substrate in an acetonitrile solution containing the adsorbate for 10 min. After this time, the sample was removed from the solution, rinsed in acetonitrile, allowed to dry and then placed in either the UPS/IPS or STM chamber for further measurement. The UPS spectra were taken with a photon energy of 40.8 eV, and the IPS spectra were taken at an electron energy of 20.3 eV. The details of these measurements are described in Chapter 2, Sections 3 and 4, respectively.

5.7 STM Imaging of N3/TiO_2(110) Surface Preparation

We used STM imaging to monitor the preparation of N3/TiO_2(110) surface. Briefly, an STM images the surface of a sample by scanning a sharp metal tip over a region of the surface while current tunnels from the tip to the sample or vice versa. We imaged the surfaces in constant current mode, where the distance between the tip and the surface is varied as the tip is scanned in order to maintain a constant tunneling current, thereby mapping the contour of the surface. The STM images shown in Fig. 5.9(a)-(c) were taken at a tip bias of -1.82 V, and a constant current between 0.5 nA and 1.0 nA. This tip bias corresponds to tunneling into the unoccupied states of the sample.

Fig. 5.9(a) shows an STM image of the TiO_2(110) surface where the bright spots represent Ti atoms that form rows along the [001] direction. This image shows a well-ordered surface that is in keeping with the model TiO_2(110) surface and with previously reported STM images of TiO_2(110).[3, 97] The surface was then passivated with pivalate ions as described above, and imaged again, as shown in Fig. 5.9(b). The bright spots in this image represent pivalate ions that form a monolayer which fully covers the TiO_2(110) surface. By comparing the images in Fig. 5.9(a) and Fig. 5.9(b), it can also be observed that the structure of the pivalate layer conforms to the structure of the substrate, in agreement with with work of Sasahara *et al.*[3] The pivalate covered TiO_2(110) sample was then removed from the vacuum and immersed in an N3/acetonitrile solution for 1 min, rinsed in pure acetonitrile, allowed to dry and reinserted in the vacuum, where it was imaged again. This image, shown in Fig. 5.9(c) shows a high coverage of dye molecules. It can also be determined from this image, based on step heights and terrace widths, that the morphology of the substrate was not altered significantly by the exposure to the atmosphere and to the solution. Thus, the passivation was effective in preserving the TiO_2(110) surface during the dye sensitization.

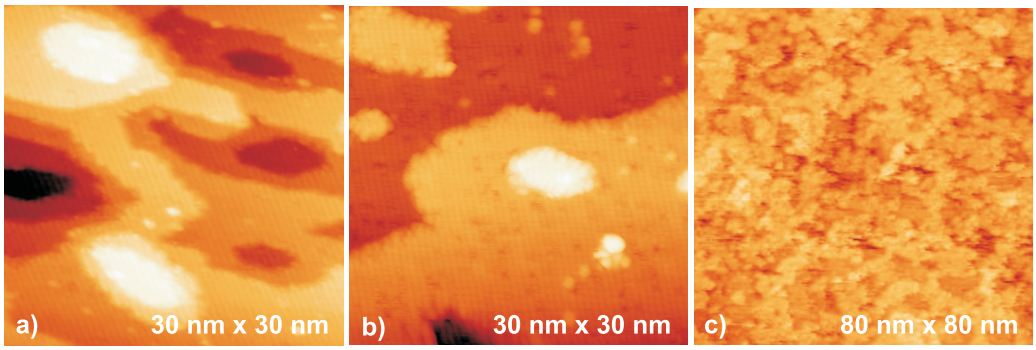

Figure 5.9: Scanning tunneling microscope images of (a)clean and (b)pivalate covered and (c)dye covered rutile TiO_2(110).

5.8 Energy Level Alignment: N3/rutile TiO_2(110)

The energy level alignment of the N3/rutile TiO_2(110) system, prepared as described above with pivalic acid passivation, is determined from the UPS and IPS spectra from a clean and N3 covered TiO_2(110) surface. Fig. 5.10 shows a UPS and an IPS spectrum from clean TiO_2(110) (black curves) and N3/TiO_2(110) (red curves). These spectra were normalized so that the maximum intensity of each spectrum was equal. The valence band of TiO_2 is composed of O $2p$ states, and the conduction band is mostly Ti $3d$ states with a small admixture of O $2p$ states, as is characteristic of a transition metal oxide. The TiO_2 VBM and CBM were determined by linearly fitting the band edges with respect to the zero intensity line, as shown in Fig. 5.10, from which we find a VBM of -3.4 eV, a CBM of 0.2 eV and a band gap of 3.6 eV for TiO_2(110). The band gap we measure for rutile TiO_2 is larger than the one typically quoted in the literature, which is an optically measured gap of 3.0 eV. [15] This difference may be attributed to the fact that the band gap we measure is a transport gap in that the measurements of energy of the VBM and the CBM do not inherently involve the creation of excitons. Excitons are inherently created in the optical measurement of the TiO_2 band gap, however, which lower the value of the band gap measured in this way.

The UPS and IPS spectra from the N3/TiO_2(110) surface both show large differences from the spectra from the clean surface. A new feature appears in the UPS spectrum of the dye covered surface in the TiO_2 band gap region, the peak of which occurs at -1.9 eV. This feature is identified as the HOMO of the dye molecule. A comparison

between the IPS spectrum from the $TiO_2(110)$ and $N3/TiO_2(110)$ surfaces shows that the latter appears to shifted upward in energy. This shift can be seen most clearly in the Ti $3d$ feature, which has a peak at 2 eV in the IPS spectrum from the clean surface, but has a peak at 2.7 eV in that of the N3 covered surface. We attribute this upward shift in energy to band bending in the surface region of TiO_2, which is a response to the bonding between N3 and TiO_2, where charge is transferred to the N3 molecules.

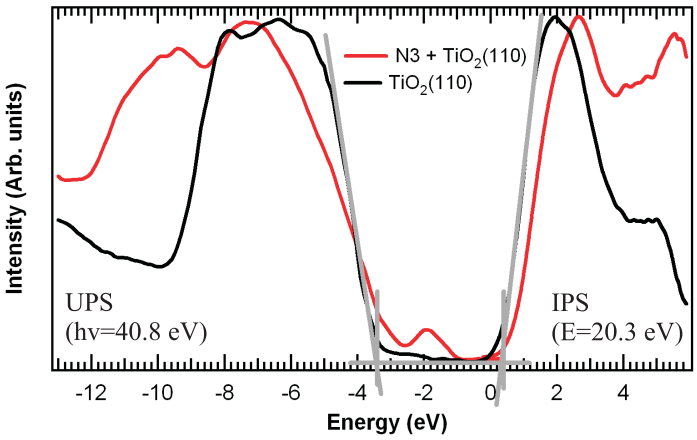

Figure 5.10: UPS and IPS spectra of the clean and N3 covered $TiO_2(110)$ surfaces.

We find that by shifting the IPS spectra from the clean surface up in energy by 0.6 eV, the best alignment between the Ti $3d$ features of clean and N3 covered surfaces is obtained. As this is an electrostatic shift, both the UPS and IPS spectra from the clean surface were shifted upwards by 0.6 eV, as shown in Fig. 5.11, to accurately represent the alignment between the TiO_2 and N3 electronic levels. After the IPS spectrum from the clean surface has been shifted, differences between the shape of the Ti $3d$ feature from the clean surface and the dye covered surfaces can be observed. The most notable of these differences is an increase in intensity in the region between 0 eV and 2 eV in the spectrum from $N3/TiO_2(110)$. As it is expected that the dye LUMO will occur near the TiO_2 CBM, where it would be obscured by the strong Ti $3d$ feature, it was necessary to investigate the differences between the two IPS spectra further.

In order to estimate the unoccupied density of states of the N3 layer, we subtracted a scaled IPS spectrum of the clean surface from that of the dye covered surface. The purpose of scaling the spectrum from the clean surface was to take into account the

attenuation of TiO_2 contribution to the N3/TiO_2 spectrum. As a maximum estimate of the TiO_2 contribution, we scaled the clean surface spectrum so that it did not exceed the spectrum from the N3 covered surface at any point. This method resulted in a scaling of the clean surface spectrum by 0.95. The result of the subtraction of the scaled clean surface spectrum from that of the N3/TiO_2(110) surface is the difference spectrum, shown as a solid blue line in Fig. 5.11. In this difference spectrum, a feature with a peak at 1.3 eV can be observed, which we identify as the N3 LUMO. A second, small feature can also be identified, between 2 eV and 3 eV, which can tentatively be identified as a LUMO+1, in keeping with the feature labeling of Schnadt *et al* discussed in Section 5.[6] The assignment of the LUMO+1 identification to the second features is tentative, however, because taking the difference between two rapidly varying curves may result in small features that are artifacts of the subtraction. A third characteristic of the difference spectrum is a broad feature in the higher energy region (3-6 eV).

Another approach to estimating the scaling factor for the IPS spectrum for the clean TiO_2 surface before the subtraction is to use equation 5.2. This equation gives the attenuation factor of the spectral intensity of a substrate by an overlayer. In this equation, I represents the spectral intensity after attenuation, $I_\circ$ represents the spectral intensity before attenuation, λ stands for electron attenuation length and d stands for depth below the surface. By using a value of 10 Å for the depth of the N3/TiO_2 interface below the surface, which corresponds to the diameter of an N3 molecule[5], and an electron attenuation length of 20 Å, which is typical for an organic molecule[119], a scaling factor of 0.6 is found for the intensity from the substrate.

A compromise between the the scaling factor which gives a high estimate to the contribution from the substrate (0.95) and one that gives a lower estimate to the contribution from the substrate (0.6) was also used to find the difference spectrum and estimate the unoccupied DOS of N3. By using a scaling factor of 0.8, the difference spectrum, shown as a blue dotted line in Fig. 5.11, was found. In this difference spectrum, the energy of the peak of the LUMO is 0.2 eV higher than what it was in the difference spectrum determined from the high estimate for the substrate contribution, but the shape of the LUMO does not change greatly. The most noticeable change

between the two difference spectra is that the LUMO+1 peak is more intense when a lower estimate to the substrate contribution is used.

Besides the difficulty in determining the scaling factor for the clean surface spectrum, it should be acknowledged that subtracting the IPS spectrum of the clean surface from that of N3/TiO_2(110) may result in some inaccuracy from the possibility that the unoccupied DOS of TiO_2(110) may be altered by the adsorption of the N3 molecules.

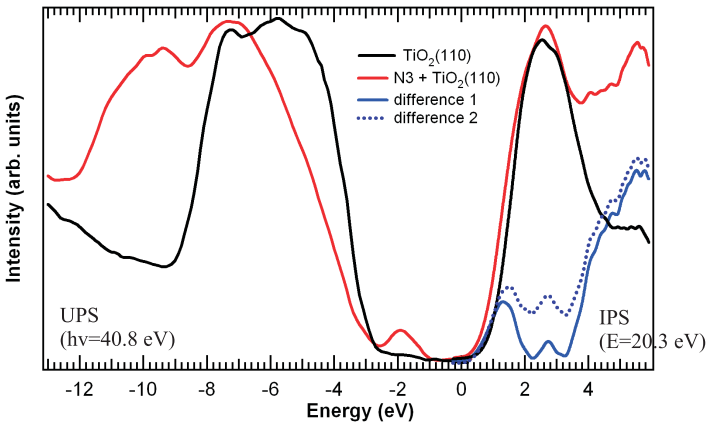

Figure 5.11: UPS and IPS of clean and dye/TiO_2 surfaces, where the clean surface spectra have been shifted and scaled. The two difference spectra were obtained using different estimates to the contribution from the substrate.

$$I = I_\circ \exp^{\frac{-d}{\lambda}} \tag{5.2}$$

The information gained from the UPS and IPS spectra from clean and N3 covered surfaces is summarized in the energy level diagram in Fig. 5.12(a) and (b). Using the peak energies of the HOMO and the LUMO (found from difference spectrum using higher scaling factor), and the energies of the TiO_2 VBM and CBM after shifting, we find that the the HOMO is 0.9 eV above the TiO_2 VBM, and the LUMO is 0.5 eV above the TiO_2 CBM, as shown in Fig. 5.12(a). The peak-to-peak HOMO-LUMO gap is 3.2 eV. Another way to characterize the HOMO and LUMO are by their edges on the side of the Fermi level, which will be referred to as the HOMO maximum and LUMO minimum. These quantities, which are analogous to the VBM and CBM of band gap materials, are determined by linear extrapolations of the HOMO and LUMO leading edges to the zero intensity line, as represented schematically in Fig. 5.12b. We find

that the maximum of the HOMO is 1.8 eV above the TiO_2 VBM and the minimum of the LUMO is 0.4 eV below the TiO_2 CBM. The gap between the HOMO maximum and LUMO minimum, which will be referred to as the minimum HOMO-LUMO gap, is 1.4 eV. As no other studies of the electronic structure of N3/TiO_2(110) have been reported, I will reserve comparison with literature results for a later section.

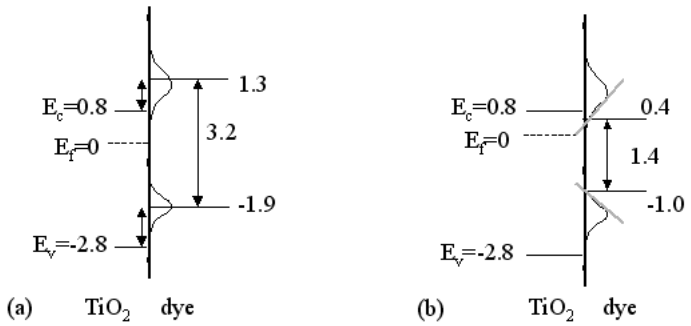

Figure 5.12: Energy level alignment between the (a)peaks and (b)edges of the HOMO and LUMO and the rutile TiO_2(110) VBM and CBM. Energies are given in eV.

As described earlier, there are a number of steps in preparing the N3/TiO_2(110) surface. To ensure that the features that we attribute to N3 were not induced by one or more of these steps, we performed a UPS and IPS spectrum on the rutile TiO_2(110) surface at each stage of the preparation of the N3/TiO_2(110) surface. Fig. 5.13 shows the UPS and IPS spectra of clean TiO_2(110), clean TiO_2(110) exposed to the atmosphere, clean TiO_2(110) exposed to pivalic acid, and a pivalate covered TiO_2(110) surface that was immersed in acetonitrile. Three important observations can be made from these spectra. The first is that none of the UPS spectra show emission in the band gap region, as the UPS spectrum from N3/TiO_2 does. Second, the IPS spectra do not differ significantly in the region of the Ti $3d$ level, or in the higher energy region. Third, the band edges in both the UPS and IPS spectra are not shifted from their clean surface energies. From these observations, we conclude that the features we attribute to N3 are accurately attributed, and that the energy shift in the TiO_2 states is due to the N3 layer.

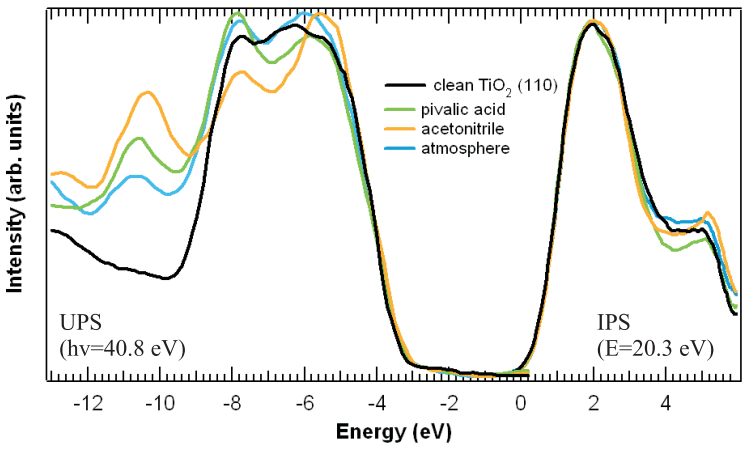

Figure 5.13: Comparison of UPS and IPS of clean $TiO_2(110)$ and $TiO_2(110)$ exposed to pivalic acid, acetonitrile, and atmosphere.

5.9 Energy Level Alignment: N3/TiO_2 nanoparticle film

By the same method as that used for N3/$TiO_2(110)$, we have also determined the energy level alignment of the N3/anatase TiO_2 nanoparticle film system. It should be noted that this sample was not passivated with pivalic acid before being dye sensitized. Fig. 5.14(a) shows UPS and IPS spectra from the clean and N3 covered anatase TiO_2 nanoparticle surfaces. As in the previous analysis, the spectra of the clean surface have been shifted to align the Ti $3d$ conduction band features. The shift for the spectra from the clean surface in this case was 0.1 eV, which is considerably smaller than it was for the spectra from the $TiO_2(110)$ surface (0.6 eV). The difference in shift is attributed to the nanoparticle size of 10-20 nm. The band bending in the $TiO_2(110)$ takes place over a region that is on the order of 100 nm wide. Thus, in the nanoparticles there is not sufficient width for the charge carriers in the TiO_2 to rearrange and fully bend the bands upward.[45]

After shifting, the TiO_2 VBM and CBM are found from the UPS and IPS spectra from the clean surface to be -3.2 and 0.6 eV, respectively. This gives a band gap of 3.8 eV. The band gap for the anatase nanoparticles is larger by 0.2 eV than the one we measured for rutile $TiO_2(110)$, which agrees with a report in the literature.[15] As with rutile TiO_2, the band gap that we measure for anatase TiO_2 is 0.6 eV larger than

the the value typically reported. Again, we attribute this difference to the fact that the typically reported value is an optical gap and we measure a transport gap. The optical gap is expected to be lower than the transport gap by the exciton binding energy.

The N3 HOMO can be observed in the UPS spectrum of N3/TiO_2, shown in Fig. 5.14, with a peak at -1.8 eV. In order to estimate the unoccupied DOS of N3 on TiO_2, the spectrum from the clean TiO_2 surface, which was scaled by 0.97, was subtracted from that for N3/TiO_2. In the difference spectrum, shown in Fig. 5.14 as the blue solid line, the feature with a peak at 1.3 eV is identified as the N3 LUMO. The broad feature in the 3-6 eV energy range is also attributed to N3. As in the case of N3/TiO_2(110), a lower scaling factor for the TiO_2 spectrum (0.8) was also used to calculate a second difference spectrum. This spectrum is shown as a blue dotted line in Fig. 5.14. The shape of the second difference spectrum is distinct from that of the first in that there is increased intensity between 2 eV and 3 eV. It may be that there are a LUMO and a LUMO+1 in the second difference spectrum, but that they are broad and overlap each other. Broadened spectral features for N3 in the N3/TiO_2 nanoparticle system could be explained by a rougher surface than that of TiO_2(110) surface, which would give rise to many non-equivalent bonding sites for N3, and result in inhomogeneous broadening of the LUMO and LUMO+1.

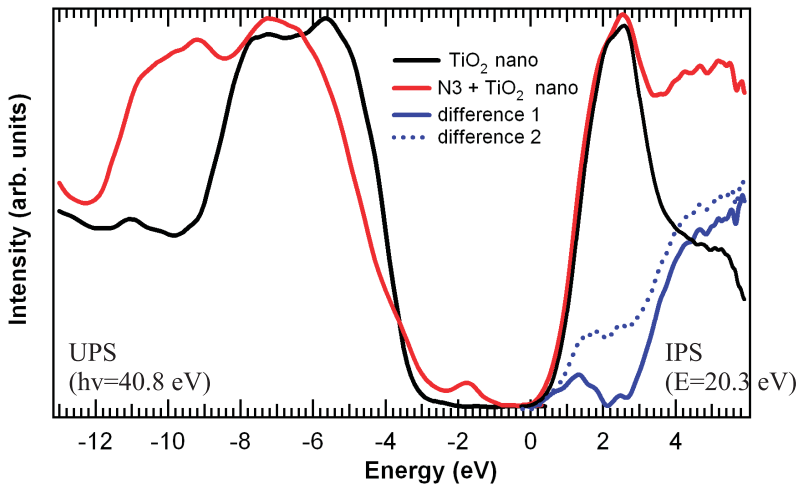

Figure 5.14: UPS and IPS of clean and N3/anatase TiO_2 nanoparticle surfaces, where the clean surface spectra have been shifted and scaled.

Fig. 5.15(a) and (b) show the energy level alignment as determined from the UPS and IPS spectra. In Fig. 5.15(a), the peak of the HOMO is 1.4 eV above the TiO_2 VBM, the peak of the LUMO is 0.7 eV above the TiO_2 CBM, and the peak-to-peak HOMO-LUMO gap is 3.1 eV. In Fig. 5.15(b), the HOMO maximum is 2.4 eV above the TiO_2 VBM and the LUMO minimum is 0.4 eV below the TiO_2 CBM, and the minimum HOMO-LUMO gap is 1.1 eV. A comparison between the energy level alignment for N3/TiO_2(110) and that for N3/TiO_2 nanoparticles reveals that LUMO-CBM difference is 0.2 eV larger and the HOMO-VBM difference is 0.5 eV larger in the case of the nanoparticle system. The peak-to-peak HOMO-LUMO gap is nearly the same in each case.

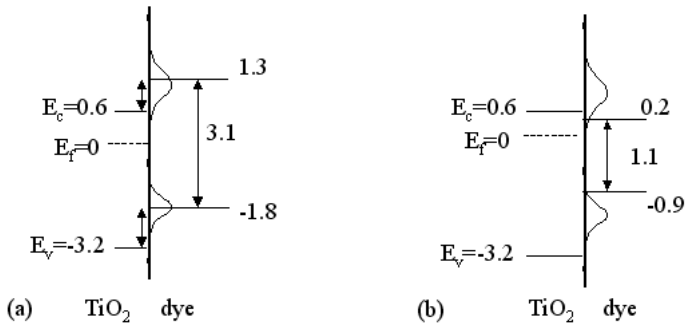

Figure 5.15: Energy level alignment between the (a)peaks and (b)edges of the HOMO and LUMO and the anatanse TiO_2 nanoparticle VBM and CBM. Energies are given in eV.

Comparisons with the literature can be made with our results from the N3/TiO_2 nanoparticle system. Snook *et al.* and Hagfeldt *et al.* found a HOMO-VBM differences of 0.5 eV and 1.2 eV, respectively, whereas we determined HOMO-VBM difference of 1.4 eV.[106, 5] The optical measurement of the peak-to-peak HOMO-LUMO gap of Snook *et al* of 2.3 eV is smaller than the value we measure of 3.1 eV.[106] As with the TiO_2 band gap, the difference between these band gaps can be attributed to the exciton binding energy that lowers the value of the optically measure gap. It is expected that the exciton binding energy should be even larger for an organic molecule than it is for a solid oxide.[116]

It is more difficult, however to reconcile our peak-to-peak HOMO-LUMO gap with that measured by Hagfeldt *et al.* from the maximum of IPCE measurement, from

which they find a value of 2.3 eV. Strictly speaking, however, this is not a direct measure of the density of states of N3. Other factors may affect the current efficiency for different photon energies. An example of this is that the transition probability from the dye into the TiO_2 may vary as a function of energy above the TiO_2 CBM. A clearer comparison between our energy level alignment and the IPCE measurement can be made by considering the the minimum photon energy that contributes to the current in the IPCE measurement. This energy, which can be observed from the IPCE curve in Fig. 5.7(b), is ∼1.7 eV. The minimum photon energy that produces a current corresponds to the difference between the TiO_2 CBM and the HOMO maximum. We find this energy to be 1.5 eV, as can be seen in Fig. 5.15(b), which agrees well with between our results the value from the IPCE measurement.

5.10 Energy Level Alignment: N3/$ZnO_2(11\bar{2}0)$ epitaxial film

Fig. 5.16 shows the UPS and IPS spectra for the clean and dye sensitized ZnO($11\bar{2}0$) surfaces, where the ZnO surface was passivated before sensitization. The UPS spectrum from the clean ZnO surface has a Zn $3d$ core level at -11 eV, and a valence band consisting mostly of O $2p$ states. The IPS spectrum from clean ZnO does not have any sharp features, as the conduction band is dominated by Zn $4s$ and $4p$ states. The featurelessness of the ZnO conduction band, as well its low cross section, made ZnO a good substrate for the purpose of observing the LUMO directly in the IPS spectrum from N3/ZnO.

For the clean ZnO surface, we find a ZnO VBM of -3.1 eV and a CBM of 0.6 eV, which gives a band gap of 3.7 eV. The spectra from the clean surface of this sample were not shifted in determining the energy level alignment, as there was no clear feature that could be used to align the clean surface spectra with those from N3/ZnO. The good match between the IPS spectra from the clean and N3 covered surfaces suggests that the shift in the oxide states due to the N3 layer is negligible, in contrast to the N3/TiO_2(110) system, where the shift in the oxide states due to the N3 layer was appreciable. In the UPS spectrum from the N3/ZnO surface, shown in Fig. 5.16, there is a feature which we attribute to the N3 HOMO. This feature has a peak at -1.9 eV, similar to its energy

in the the N3/TiO_2 systems. A key characteristic of the IPS spectrum from N3/ZnO, also shown in Fig. 5.16, is that there is a feature in the region of 1-4 eV, which we attribute to the dye LUMO. This is an important result for N3/ZnO, as the N3 LUMO for N3/TiO_2 could only be identified clearly in the difference spectra.

Despite being able to identify the LUMO in the IPS spectrum from N3/ZnO, we determined two difference spectra for N3/ZnO in order to estimate the unoccupied DOS of N3 on ZnO. The curve shown as a solid blue line in Fig. 5.16 and labeled "difference 1" was calculated using clean surface spectrum that was not scaled. In the same, way the curve shown in Fig. 5.16 with a blue, dotted line and labeled "difference 2" was calculated with a clean surface spectrum that was scaled by 0.8. The two difference spectra show a similar shape for the LUMO, which has a peak at 2.5 eV in the "difference 1" spectrum and a peak at 2.7 eV in the "difference 2" spectrum.

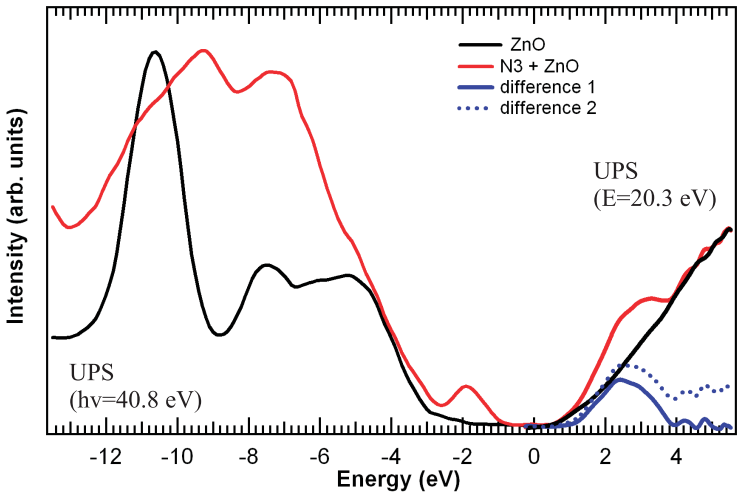

Figure 5.16: UPS and IPS of clean and dye/ZnO(11$\bar{2}$0) surface.

Fig. 5.17(a) and (b) represents the alignment between the N3 HOMO and LUMO and the ZnO VBM and CBM. The center of the dye HOMO is 1.2 eV above the ZnO VBM, the center of the dye LUMO is 1.9 eV above the ZnO CBM, and the peak-to-peak HOMO-LUMO gap is 4.4 eV. Fig. 5.17(b) shows that the HOMO maximum is 2.2 eV above the ZnO VBM, the LUMO minimum is 0.5 eV above the ZnO CBM, and the minimum HOMO-LUMO gap is 2.0 eV. We note that the peak-to-peak HOMO-LUMO gap for N3 on ZnO is over 1 eV larger than the equivalent HOMO-LUMO gap for N3

on the TiO_2 substrates. With regards to the minimum HOMO-LUMO gap for N3 on ZnO (2.0 eV), it is also larger that than that for N3/TiO_2(110) (1.4 eV) and N3/TiO_2 nanoparticles (1.1 eV).

With regards to the comparisons, it should also be noted that there are significant differences in shape between the unoccupied DOS for N3 on ZnO and that for N3 on either of the TiO_2 substrates. One difference is that the LUMO for N3 on ZnO (full width at half maximum (FWHM) $\sim$ 1.5 eV) is broader than it is for N3 on TiO_2 (FWHM $\sim$ 1.0 eV). This could be because the LUMO is broader for N3 on ZnO, or because the LUMO and LUMO+1 overlap. Another distinction between the difference spectra for N3 on ZnO and those for N3 on TiO_2 is that the rise in intensity above 3 eV is greatly diminished for the N3/ZnO system. It is interesting to observe that the HOMO for N3/ZnO is very similar to those for N3/TiO_2, but the LUMO's are different. The similar HOMO shapes may be accounted for in that the HOMO is localized on the center of the N3 molecule and does not strongly interact with the substrate. In contrast, the LUMO is thought to overlap with substrate.[4] Thus, the different orbital character of the TiO_2 and ZnO conduction bands may give rise to differences in the LUMO of N3 molecules adsorbed on each of these substrates. The differing N3-substrate interactions may also account for the differing shifts in the oxide states that are observed for the N3/TiO_2(110) and N3/ZnO systems, which correspond to different amounts of charge transfer between the oxide and the dye molecules.

In a study that measured the IPCE curves for DSSC's using N3/ZnO nanoparticles and N3/TiO_2 nanoparticles, the minimum photon energy for current production for both systems was found to be 1.7 eV.[111] This study also found that the maxima of the IPCE curves for the respective systems were both $\sim$2.4 eV. The value for minimum photon energy to produce current can be compared to measured energy level alignment shown in Fig. 5.17(b), where the lowest energy photon that would produce current corresponds to the energy between the LUMO minimum and the HOMO maximum, which we found to be 2.0 eV for N3/ZnO. This value is in reasonably good agreement with the value from the ICPE measurement of 1.7 eV.

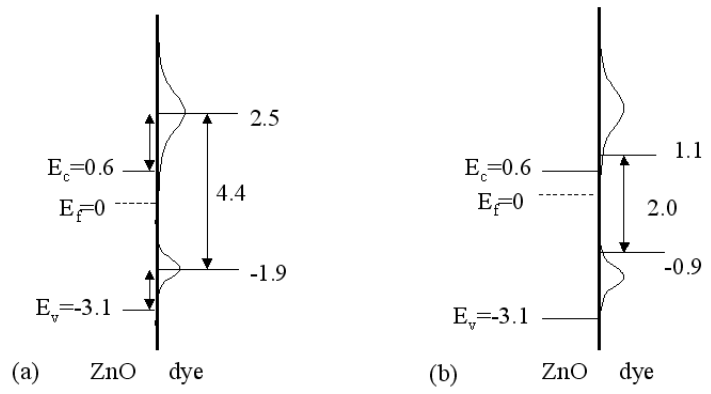

Figure 5.17: Energy level alignment between the (a)center and (b)edges of the HOMO and LUMO and the ZnO VBM and CBM. Energies are given in eV.

5.11 Energy Level Alignment: INA/TiO_2 and INA/ZnO($11\bar{2}0$)

As discussed in Section 4, the motivation for studying isonicotinic acid (INA) adsorbed on TiO_2 and ZnO is to gain insight into the LUMO of N3. INA consists of a pyridine/carboxylic acid complex, which could have similar properties to the pyridine/carboxylic acid complexes of N3, on which the LUMO is thought to be localized.[5, 4] Fig. 5.18(a) shows the UPS and IPS spectra from the clean and INA covered surfaces of rutile TiO_2(110), where the clean surface spectra were shifted upward in energy by 0.1 eV. For this sample, the INA was dosed onto a pivalate covered TiO_2 surface. From the UPS spectrum of INA/TiO_2, it can be observed that INA does not contribute states in the TiO_2 band gap as the N3 does. This is in keeping with the expectation that the parts of N3 on which the HOMO is localized, the Ru and thiocyanate groups, are not present in INA.

The LUMO of INA is observed in the IPS difference spectrum with a peak at 1.0 eV, as shown in Fig. 5.18. A second feature, which is tentatively identified as the LUMO+1, as in the case of dye/TiO_2(110), can also be observed centered at 2.5 eV. A third, broad feature can be observed in the energy range from 3-6 eV. All of these characteristics are similar to the difference spectrum for the N3/TiO_2(110) system, as can be seen in Fig.5.18(b), which compares the IPS difference spectrum for INA/TiO_2(110) and both calculated difference spectra for N3/TiO_2(110). The comparison of these spectra suggest that INA has similar unoccupied electronic structure to N3, as was expected.

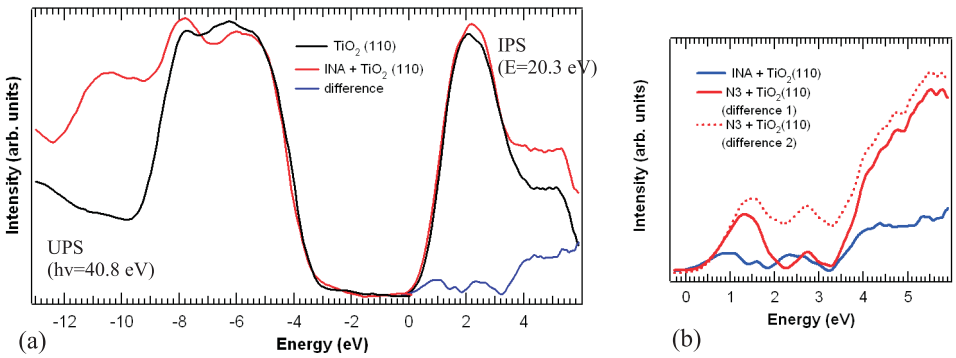

Figure 5.18: (a)UPS and IPS of clean and INA/rutile TiO_2(110) surfaces. (b)IPS difference spectra of N3/TiO_2(110) and INA/TiO_2(110).

The UPS and IPS from clean ZnO, clean ZnO exposed to atmosphere and INA/ZnO are shown in Fig. 5.19(a), where the clean surface spectra were not shifted. For this sample, the ZnO surface was not passivated with pivalic acid before being dosed with INA. It should be noted, however, that the spectra from an INA covered ZnO surface that was passivated before INA deposition were nearly identical. As with INA/TiO_2(110), the INA does not add states in the band gap of ZnO. A key observation concerning the IPS spectra is that the spectrum from INA/ZnO shows increased intensity in the region between 1 and 4 eV compared to the spectra from the clean ZnO surface and that from the atmosphere exposed ZnO surface. To estimate the unoccupied DOS of INA, two IPS difference spectra were calculated, one using the spectrum from the clean surface and the other using the spectrum from the atmosphere exposed surface. The difference spectra are similar in that they both have a broad LUMO with a peak at $\sim$3 eV. Fig. 5.19(b) compares the difference spectra for N3/ZnO and INA/ZnO. Again, it can be seen that the unoccupied electronic structure for N3 and INA are similar. Of the two difference spectra for INA/ZnO, the one calculated with the IPS spectrum from the atmosphere exposed ZnO surface agrees better with the difference spectrum for N3/TiO_2(110), as it is not as broad and has a peak at a lower energy.

Similar to what was done with the TiO_2(110) surface, we have performed UPS and IPS at various stages of the preparation of the INA/ZnO surface to verify that the properties we attribute to INA are not induced at other stages of the surface preparation. Fig. 5.20 shows UPS and IPS spectra from clean ZnO, clean ZnO exposed to

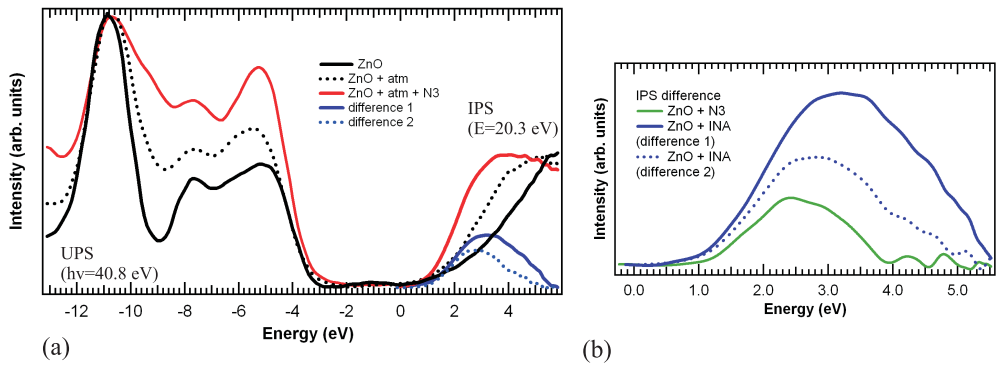

Figure 5.19: (a)UPS and IPS of clean ZnO, atmosphere exposed ZnO, and INA/ZnO surfaces. (b)IPS difference spectrum for N3/ZnO and INA/ZnO.

atmosphere, clean ZnO exposed to acetonitrile and INA/ZnO. As with the investigation of the process steps for preparing the N3/TiO_2(110) surface, we find that none of the process steps result in a shift in the spectra, nor do they result in states in the band gap region. The IPS spectra from the atmosphere and acetonitrile exposed ZnO surfaces differ from that of the clean surface in that they show increased the intensity between 2-4 eV. The IPS spectrum from INA/ZnO surface, however shows a significantly greater increase over these two in the region between 1 eV and 4 eV. We are confident, therefore, in attributing this strong increase in intensity to the unoccupied states of INA.

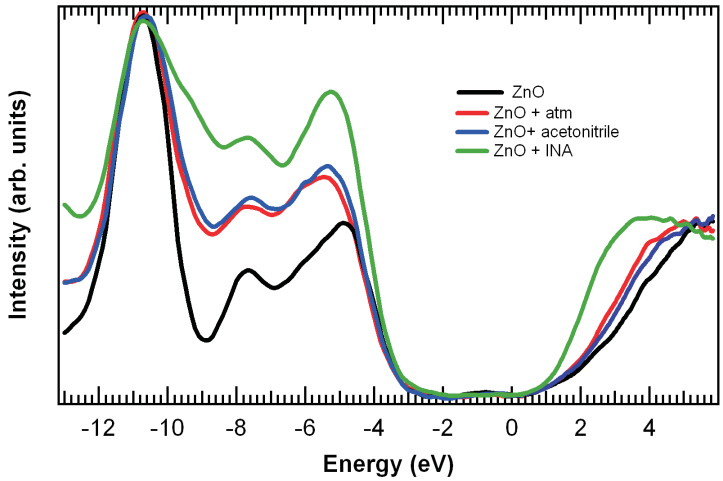

Figure 5.20: UPS and IPS from clean, atmosphere exposed, acetonitrile exposed and INA/ZnO surfaces.

5.12 Conclusions

In this chapter, a complete method of measuring the energy level alignment between molecular adsorbates and oxide substrates has been discussed. By measuring the occupied and unoccupied electronic states directly, we determined the energy level alignment of adsorbate/oxide systems relevant to DSSC's in a more complete and reliable way than has been done before. Results have been presented for the N3/TiO_2(110), N3/TiO_2 anatase nanoparticle and N3/ZnO($11\bar{2}0$). These results show that the energy level alignment is similar for the two N3/TiO_2 systems. The N3 unoccupied DOS for the two N3/TiO_2 systems is similar, as well, though more substantial inhomogeneous broadening may be present for the N3/TiO_2 nanoparticle system. The unoccupied DOS of N3 on ZnO has been shown to differ from that of N3 on TiO_2. This was attributed to the different character of the TiO_2 and ZnO conduction bands, which would be expected to interact differently with the unoccupied states of N3. The different orbital character of the TiO_2 and ZnO conduction bands could also be the reason for the differing amount of substrate-adsorbate charge transfer observed for N3/TiO_2(110) and N3/ZnO.

In comparison with available literature results, discrepancies between the oxide band gaps and the peak-to-peak HOMO-LUMO band gaps we measured were found. These discrepancies were attributed to the role of excitons in the optical measurement of the energy gap, which result in lower values than those measured by the combination of UPS and IPS, which measure a transport gap. We have also measured the electronic structure of a INA, which is representative of a key part of N3, on TiO_2 and ZnO. The comparisons between the occupied and unoccupied electronic structure of INA on TiO_2(110) and ZnO($11\bar{2}0$) with those of N3 on the same substrates show that these two molecules have very different occupied electronic structure and similar unoccupied electronic structure, in keeping with expectations.

Chapter 6

Summary

In this thesis, I have presented results from the measurement of the energy level alignment of metal/oxide/semiconductor (MOS) stacks with high-κ oxides and metal gates, and of organic dye/oxide systems. The metal/oxide/semiconductor systems we measured are relevant to metal-oxide-semiconductor field effect transistors (MOSFET's), and the organic dye/oxide systems we measured are relevant to dye sensitized solar cells (DSSC's). These measurements were made using a combination of inverse photoemission spectroscopy (IPS) and UV photoemission spectroscopy (UPS) in the same vacuum chamber at Rutgers. For the MOS systems, we also performed soft X-ray photoemission spectroscopy (SXPS) measurements in a vacuum chamber at beamline U5 at the National Synchrotron Light Source (NSLS).

The importance of this work is twofold. First, it enables an approach to materials research where the energy level alignment we measured serves as a link between both the device and materials theory communities. We have shown the relevance of the energy level alignments we measured to devices in that they are correlated with key device characteristics such as leakage current across the oxide in MOSFET's and minimum photon energy to produce current in DSSC's. The energy level alignments we measured can also serve as a benchmark for theorists in that they are a good approximation of the ground state energy level alignment. Thus, they give can be used by theorists to determine which methods of calculation are producing realistic results. As new material systems are investigated for use in devices, measurements of the sort we introduce here can be used to guide theorists as they calculate the properties of the new systems to see if they will give increased device performance. In this way, a wider range of materials can be investigated more quickly in the effort to achieve improved device performance

than if new materials were simply tested in devices in a trial and error manner.

The second aspect of the importance of this work is in the physical insight that is gained through spectroscopic measurements. For example, we have shown that chemical reactions at the metal-oxide interfaces of metal-oxide-semiconductor (MOS) stacks have an influence on the band offsets at the metal-oxide interface. For organic dye/oxide systems, we have shown that the unoccupied density of states of N3 dye is different when it is adsorbed on TiO_2 and ZnO substrates. These physical insights along with the energy level alignment measurements can help to give a greater understanding of the physical properties that effect device performance, as well as contribute to the ability to engineer devices in such as way as to improve the performance.

We measured several high-κ oxide/Si systems (HfO_2/Si, $Hf_{0.7}Si_{0.3}O_2$/Si, ZrO_2/Si, Al_2O_3/Si) as well as SiO_2/Si with UPS and IPS to determined the valence band maximum (VBM), conduction band maximum (CBM), and thus, the band gap. The VBM and CBM were extracted from the UPS and IPS spectra, respectively, by a straightforward linear fitting procedure. In order to find the band offsets of these oxides with Si, we performed SXPS measurements on the same material systems at the NSLS, where the samples were prepared under the same conditions used at Rutgers. The intensity of the SXPS spectra in the oxide band gap region, which we attributed to the substrate Si, was used to find the Si VBM. From the measured Si VBM and the accepted value for the Si band gap, the oxide-semiconductor valence band offset (VBO) and conduction band offset (CBO) could be determined.

The importance of this work can also be seen through a comparison between the band offset values we measured for high-κ oxide/Si and SiO_2/Si systems and values from the literature, which can differ by as much as 1 eV. The wide scatter of the literature values is due to the variety of sample growth and preparation procedures employed, as well as the variety of measurement methods used. Due to the completeness of the method we used, where we measure both the occupied and unoccupied states directly, and the simplicity of the band edge determination, it is reasonable to consider our method to be among the most reliable of the methods used to measure band offsets. Thus, our study will help to establish more accurate measured values for high-κ oxide/Si

band offsets.

We also observed strong downward band bending (0.8-0.9 eV) in the p-Si substrates of high-κ oxide/Si samples. Two possible explanations for this band bending are Fermi level pinning, or positively charged defect states in the high-κ and/or SiO_2 interfacial layers. Our investigation of the Fermi level pinning explanation was hindered by a lack of high-κ oxide/n-Si samples in our sample set. The explanation of fixed charge in the oxide layers was pursued by an investigation of the capacitance-voltage (C-V) measurement literature, which did not conclusively support the the explanation. Thus, explanation of the downward band bending in the Si is still an open question.

To measure the VBO and CBO between the metal and oxide layers, we used the measurement of the oxide VBM and CBM, and measured the shift in the oxide states upon metal deposition. Measuring this shift involved depositing thin metal layers (2-3 Å) and performing spectroscopy. We found the metal-oxide VBO and CBO for all combinations of Ru, Al and Ti metals and HfO_2, $Hf_{0.7}Si_{0.3}O_2$/Si, Al_2O_3 and SiO_2 oxides on Si.

We also used the Interface Gap State (IGS) model to predict the metal-oxide CBO values for these systems. This was done by taking values for the pinning parameters and the charge neutrality levels that were reported the literature, and measuring the metal work functions and oxide electron affinities using UPS. We found that the experimental metal-oxide CBO values tended to agree well with the values determined using the IGS model for the Ru/oxide and Ti/oxide systems, but the agreement was worse for the Al/oxide systems.

We correlated the trends in agreement between the experimental and IGS CBO values with the composition of the metal overlayers through a study of the core levels from the metal overlayers. The metal core level spectra showed that the Ru layers were metallic throughout, the Al layers were Al_2O_3 at the Al/oxide interface and metallic in the region farther from the original oxide film, and the Ti layers consisted of a dilute Ti-O_x alloy that became slightly more Ti rich in the region farther from the original oxide film. The correlation between these observations and trends in agreement between the experimental and IGS CBO values led to the conclusion that the IGS model is a

good predictor of the metal-oxide CBO value for metal-oxide systems where there is no additional oxide interfacial layer. Thus, by the spectroscopic approach we used, we gained insight into the interactions at the metal-oxide interface that had an effect on the band offsets.

The study of the core levels from the high-κ oxide and SiO_2 interfacial layers showed the effect of the metal layers on the composition of these oxide layers. For Ru/SiO_2 and $Ru/Al_2O_3/Si$ systems, partial reduction 10% of the SiO_2 and 18% of the Al_2O_3 layers was observed. This level of reduction, coupled with the consistency of the Ru core level lineshape, led to the conclusion that the metal-oxide interfaces in these systems could still be considered chemically abrupt.

The Hf and Si core levels from the HfO_2 and SiO_2 layers, respectively, from the $Ru/HfO_2/Si$ systems we measured showed that the composition of the HfO_2 and SiO_2 layers was not changed by the Ru overlayer. In the $Al/HfO_2/Si$ and $Ti/HfO_2/Si$ systems, however, the metal films had the effect of reducing the SiO_2 interfacial layers, while leaving the composition of the HfO_2 layers unchanged, up to a small degree of reduction ($\sim$1%). Again, the spectroscopic methods we used provided insight into the reactions taking place within the MOS stack which can have an influence on device characteristics.

We also used the combination of IPS and UPS to measure the energy level alignment for organic dye/oxide systems. We measured the energy level alignment for N3 dye and isonicotinic acid (INA) layers on rutile $TiO_2(110)$, anatase TiO_2 nanoparticle and epitaxial $ZnO(11\bar{2}0)$ film substrates. The $N3/TiO_2(110)$, $INA/TiO_2(110)$, $N3/ZnO(11\bar{2}0)$ and $INA/ZnO(11\bar{2}0)$ systems were prepared by passivating clean, well-ordered oxide substrates with pivalic acid to reduce atmospheric and solution contamination during the deposition of the molecular overlayers. This passivation was shown to preserve the morphology of the oxide layers during these exposures by STM imaging.

In order to find the energy level alignment between the adsorbed molecules and the oxide substrate, we measured the UPS and IPS spectra from both the clean and molecule covered oxide surfaces. For all of the N3/oxide systems we measured, the highest occupied molecular orbital (HOMO) feature could be observed in the UPS

spectra from the N3 covered surfaces in the band gap region. For the N3/TiO_2 systems we measured, however, the lowest unoccupied molecular orbital (LUMO) features could only be clearly observed by subtracting the IPS spectrum from the clean surface from that of the N3 covered surface to estimate the N3 density of states (DOS).

The energy level alignment we measured for the N3/TiO_2(110) system showed that the peak of the LUMO was 0.5 eV above the TiO_2 CBM and the peak of the HOMO was 0.9 eV above the TiO_2 VBM. The observation that the peak of the LUMO is several tenths of an eV above the CBM is in keeping with the efficient electron transfer from N3 dye into the TiO_2 conduction band. The energy level alignment between N3 dye and TiO_2 nanoparticles was very similar to that between N3 and TiO_2(110), particularly for the LUMO and the CBM. For both of these systems, the peak-to-peak HOMO-LUMO gap was also very similar ($\sim$3.1 eV).

An interesting difference between the N3/TiO_2(110) and N3/TiO_2 nanoparticle systems was that the TiO_2 bands were found to bend upward in the N3/TiO_2(110) system by 0.6 eV, while those in the N3/TiO_2 nanoparticle system were found to bend upward only by 0.1 eV. The upward band bending in the N3/TiO_2(110) was explained by a positive screening charge in the surface region ($\sim$100 nm) of the TiO_2 that was induced by electron transfer to the N3 molecules due to chemical bonding. The smaller band bending in the TiO_2 nanoparticle substrate was attributed to the small size ($\sim$15 nm) of the nanoparticles, which are not large enough to allow for the full upward band bending to take place.

The IPS spectrum from the N3/ZnO($11\bar{2}0$) showed the interesting result that the intensity due to the N3 molecules was clearly visible, even before the subtraction of the IPS spectrum from the clean ZnO surface. The visibility of the N3 LUMO feature in this spectrum was aided by the featurelessness and low cross section of the ZnO conduction band states. The shape of the N3 HOMO for N3/ZnO was similar to what it was for the N3/TiO_2 systems, while the shape of the N3 LUMO for N3/ZnO was much broader than that found for the N3/TiO_2 systems. A possible explanation for these observations is that the N3 HOMO is localized at the center of the N3 molecule and has little interaction with the substrate, while the LUMO is localized on the part

of the molecule that bonds to the substrate. Thus, the LUMO could be different in the N3/TiO_2 and N3/ZnO systems due to the different orbital character of the TiO_2 conduction band, which is largely composed of Ti $3d$ states, and the ZnO conduction band, which is largely composed of Zn $4s$ and $4p$ states.

The INA molecule has been frequently studied in connection with N3 because it consists of a pyridine/carboxylic acid complex. It is this ligand of N3 that is thought to bond to TiO_2, and on which the LUMO is thought to be localized. By measuring the clean and INA covered $TiO_2(110)$ and ZnO$(11\bar{2}0)$, we observed that INA did not contribute a HOMO in the band gap region of the UPS spectra, and that the LUMO's due to INA had a similar shape compared to the LUMO's of N3 on the same substrates. The first of these results support theoretical result that the N3 HOMO is localized on the Ru atom and thiocyanate ligands of N3, which are absent in INA. The second of these results supports the theoretical result that the N3 LUMO is localized on the pyridine/carboxylic acid complex that bonds to the oxide surface.

Chapter 7

Appendix

7.1 List of Acronyms

MOSFET	metal-oxide-semiconductor field effect transistor
MOS	metal-oxide-semiconductor
DSSC	dye sensitized solar cell
CBM	conduction band minimum
VBM	valence band maximum
CBO	conduction band offset
VBO	valence band offset
DOS	density of states
IPS	inverse photoemission spectroscopy
UPS	UV photoemission spectroscopy
SXPS	soft X-ray photoemission spectroscopy
XPS	X-ray photoemission spectroscopy
EELS	electron energy loss spectroscopy
AES	Auger electron spectroscopy
LEED	low energy electron diffraction
STM	scanning tunneling microscopy
IntPE	internal photoemission
XAS	X-ray absorption spectroscopy
SE	spectroscopic ellipsometry
BEEM	ballistic electron emission microscopy
I-V	current-voltage
C-V	capacitance-voltage
MEIS	medium energy ion scattering
HOMO	highest occupied molecular orbital
LUMO	lowest unoccupied molecular orbital
INA	isonicotinic acid
IPCE	incident photon to conversion
TPB	t-butyl pyridine
TCO	transparent conducting oxide

Table 7.1: List of acronyms used in this thesis.

Bibliography

[1] Internation Roadmap for Semiconductor Technology (2006). *Process Integration, Devices and Structures*, www.itrs.net.

[2] D.P. Woodruff and T.A. Delchar. *Modern Techniques of Surface Science*. Cambridge, 1988.

[3] A. Sasahara, C.L. Pang, and H. Onishi. *J. of Phys. Chem. B*, 110:4751, 2006.

[4] P. Persson and M.J. Lundqvist. *J. of Phys. Chem. B*, 109:11918, 2005.

[5] A. Hagfeldt and M. Gratzel. *Accounts of Chemical Research*, 33:269, 2000.

[6] J. Schnadt, J.N. O'Shea, L. Patthey, L. Kjeldgaard, J. Ahlund, K. Nilson, J. Schiessling, J. Krempasky, M. Shi, O. Karis, C. Glover, H. Siegbahn, N. Martensson, and P.A. Bruhwiler. *J. Chem. Phys.*, 119:12462, 2003.

[7] G.E. Moore. *Electronics*, 38(8), 1965.

[8] G.D. Wilk, R.M. Wallace, and J.M. Anthony. *J. Appl. Phys.*, 89:5243, 2001.

[9] S. Chambers, Y. Liang, Z. Yu, R. Droopad, and J. Ramdani. *J. Vac. Sci. Tech. A*, 19:934, 2001.

[10] C. Fulton, G. Lucovsky, and R. Nemanich. *Appl. Phys. Lett.*, 84:580, 2004.

[11] S. Chambers, T. Droubay, T. Kaspar, and M. Gutowski. *J. Vac. Sci. Tech. B*, 22:2205, 2004.

[12] M. Gribelyuk, A. Callegari, E. Gusev, M. Copel, and D. Buchanan. *J. Appl. Phys.*, 92:1232, 2002.

[13] S. Guha, E. Gusev, H. Okorn-Schmidt, M. Copel, L. Ragnarsson, N. Bojarczuk, and P. Ronsheim. *Appl. Phys. Lett*, 81:2956, 2002.

[14] M. Houssa. *High-κ Gate Dielectrics, p.10.* Institute of Physics, 2004.

[15] L. Kavan, M. Gratzel, S. Gilbert, C. Klemenz, and H. Scheel. *J. Am. Chem. Soc.*, 118:6716, 1996.

[16] S. Miyazaki. *J. Vac. Sci. Tech. B*, 19:2212, 2001.

[17] H. Nohira, W. Tsai, W. Besling, E. Young, J. Petry, T. Conard, W. Vandervorst, S. De Gendt, M. Heyns, J. Maes, and M. Tuominen. *J. of Non-Crystalline Solids*, 303:83, 2002.

[18] V. Afanasev, M. Houssa, A. Stesmans, G. Adriaenssens, and M. Heyns. *J. Non-Cryst. Solids*, 303:69, 2002.

[19] G. Lucovsky, B. Rayner, Y. Zhang, G. Appel, and J. Whitten. *Appl. Surf. Sci.*, 216:215, 2003.

[20] R. Puthenkovilakam and J.P. Chang. *Journal of Applied Physics*, 96:2701, 2004.

[21] S. Sayan, N. Nguyen, J. Ehrstein, J. Cahmbers., M. Visokay, M. Quevedo-Lopez, L. Colombo, D. Yoder, I. Levin, D. Fischer, M. Paunescu, O. Celik, and E. Garfunkel. *Appl. Phys. Lett.*, 87:212905, 2005.

[22] N. Nguyen, S. Sayan, I. Levin, J. Ehrstein, I. Baumvol, C. Driemeier, C. Krug, L. Wielunski, P. Hung, and A. Diebold. *J. Vac. Sci. Tech. A*, 23:1706, 2005.

[23] J. Yang and H. Park. *Appl. Phys. Lett.*, 87:202102, 2005.

[24] L. Edge, D. Schlom, S. Chambers, E. Cicerella, J. Freeouf, B. Hollander, and J. Schubert. *Appl. Phys. Lett.*, 84:726, 2004.

[25] A. Ohta, M. Yamaoka, and S. Miyazaki. *Microelectronic Engineering*, 72:154, 2004.

[26] E. Gusev, C. Cabral, M. Copel, C. D'Emic, and M. Gribelyuk. *Microelectonic Engineering*, 69:145, 2003.

[27] E. Gusev, V. Narayanan, and M. Frank. *IBM J. Res. Dev.*, 50:387, 2006.

[28] Internation Roadmap for Semiconductor Technology (2000). *Process Integration, Devices and Structures*, www.itrs.net.

[29] G. Bersuker, C. Park, J. Barnett, P. Lysaght, P. Kirsch, C. Young, R. Choi, B. Lee, B. Foran, K. van Benthem, S. Pennycook, P. Lehanan, and J. Ryan. *J. Appl. Phys.*, 100:094108, 2006.

[30] Bardeen. *Phys. Rev.*, 71:717, 1947.

[31] A.M. Cowley and S.M. Sze. *J. Appl. Phys.*, 36:3212, 1965.

[32] S. Louie and M. Cohen. *Phys. Rev. B*, 13:2461, 1976.

[33] A. Demkov, L. Fonseca, E. Verret, J. Tomfohr, and O. Sankey. *Phys. Rev. B*, 71:195306, 2005.

[34] O. Sharia, A. Demkov, G. Bersurker, and B.H. Lee. *Phys. Rev. B*, 75:035306, 2007.

[35] W. Mönch. *Phys. Rev. Lett.*, 58:1260, 1986.

[36] C. Hobbs, L. Fonseca, A. Knizhnik, V. Dhandapani, S. Samavedam, W. Taylor, J. Grant, L. Dip, D. Triyoso, R. Hedge, D. Gilmer, R. Garcia, D. Roan, M. Lovejoy, R. Rai, E. Hebert, H. Tseng, S. Anderson, B. White, and P. Tobin. *IEEE Transactions on Electron Devices*, 51:971, 2004.

[37] Y. Yeo, T. King, and C. Hu. *J. of Appl. Physics*, 92:7266, 2002.

[38] M. Depas, B. Vermeire, P. Mertens, R. Van Meirhaeghe, and M. Heyns. *Solid State Electronics*, 38:1465, 1995.

[39] S.M. Sze. *Physics of Semiconductor Devices.* John Wiley and Sons, 1981.

[40] V. Afanasev, M. Houssa, A. Stesmans, and M. Heyns. *J. Appl. Phys.*, 91:3079, 2002.

[41] E. A. Kraut, R. W. Grant, J. R. Waldrop, and S. P. Kowalczyk. *Phys. Rev. Lett.*, 44:1620, 1980.

[42] F. Bell and L. Ley. *Phys. Rev. B*, 37:1053, 1988.

[43] V.V. Afanas'ev, A. Stesmans, F. Chen, X. Shi, and S.A. Campbell. *Appl. Phys. Lett.*, 81:1053, 2002.

[44] M. Mondreanu, P. Hurley, B.J. O'Sullivan, B. O'Looney, J. Senateur, h. Rousell, M. Audier, C. Dubourdieu, I. Boyd, Q. Fang, T. Leedham, S. Rushworth, A. Jones, H. Davies, and C. Jimenez. *Proceedings of SPIE*, 4876:1236, 2003.

[45] M. Gratzel. *Nature*, 414:338, 2001.

[46] A. Roth. *Vacuum Technology, p. 209.* Cambridge, 1988.

[47] A. Roth. *Vacuum Technology, p. 217.* Cambridge, 1988.

[48] A. Roth. *Vacuum Technology, p. 241.* Cambridge, 1988.

[49] D.P. Woodruff and T.A. Delchar. *Modern Techniques of Surface Science, p. 108.* Cambridge, 1988.

[50] D.P. Woodruff and T.A. Delchar. *Modern Techniques of Surface Science, p. 144.* Cambridge, 1988.

[51] P. Johnson and J. Davenport. *Phys. Rev. B*, 31:7521, 1985.

[52] G. Ertl and J. Kuppers. *Low Energy Electrons and Surface Chemistry.* Weinheim, 1985.

[53] P.W. Palmberg. *J. Vac. Sci. Tech.*, 12:379, 1974.

[54] D.P. Woodruff and T.A. Delchar. *Modern Techniques of Surface Science, p. 1000.* Cambridge, 1988.

[55] S. Johnson, P. Hulbert, R. Garrett, and M. Howells. *Review of Scientific Instruments*, 57:1324, 1986.

[56] N. Stoffel and P. Johnson. *Nucl. Instr. and Rev. of Meth. in Phys. Res.*, 234:230, 1985.

[57] J.H. Scofield. *Am. J. Phys.*, 62:129, 1994.

[58] M. Houssa. *High-κ Gate Dielectrics, Ch. 2.* Institute of Physics, 2004.

[59] S. Sayan, S. Aravamudhan, B. Busch, W.H. Shulte, F. Cosandey, G. Wilk, T. Gustafsson, and E. Garfunkel. *J. Vac. Sci. Tech. A*, 20:507, 2002.

[60] M.-T. Ho, Y. Wang, R. Brewer, L. Wielunski, Y. Chabal, N. Moumen, and M. Boleslawski. *Appl. Phys. Lett.*, 87:133103, 2005.

[61] M. Houssa. *High-κ Gate Dielectrics.* Institute of Physics, 2004.

[62] D. Muller, T. Sorsch, S. Moccio, F. Baumann, K. Evan-Lutterodt, and G. Timp. *Nature*, 399:758, 1999.

[63] K. Tse, D. Liu, K. Xiong, and J. Robertson. *Microelectronic Engineering*, 84:2028, 2007.

[64] M. Ulrich, J. Hong, J. Rowe, G. Lucovsky, A. Chan, and T.E. Madey. *J. Vac. Sci. Tech. B*, 21:1777, 2003.

[65] F. Himpsel, G. Hollinger, and R. Pollack. *Phys. Rev. B*, 28:7014, 1983.

[66] H.Y. Yu, M.F. Li, B.J. Cho, C.C. Yeo, M.S. Joo, D.L. Kwong, J.S. Pan, C.H. Ang, J.Z. Zheng, and S. Ramanathan. *Appl. Phys. Lett.*, 81:376, 2002.

[67] S. Sayan, T. Emge, E. Garfunkel, Xinyuan Zhao, L. Wielunski, R.A. Bartynski, D. Vanderbilt, J.S. Suehle, S. Suzer, and M. Banaszak-Holl. *J. of Appl. Phys.*, 96:7485, 2004.

[68] S. Toyoda, J. Okabayashi, H. Kumigashira, M. Oshima, K. Ono, M. Niwa, K. Usuda, and N. Hirashita. *J. Electron Spectrosc. Relat. Phenom.*, 137:141, 2004.

[69] W. Zhu, T.P. Ma, T. Tamagawa, J. Kim, and Y. Di. *IEEE Electron Device Letters*, 23:97, 2002.

[70] N.V. Nguyen, S. Sayan, I. Levin, J.R. Ehrstein, I.J.R. Baumvol, C. Driemeier, C. Krug, L. Wielunski, P.Y. Hung, and A. Diebold. *J. Vac. Sci. Tech. A*, 23:1706, 2005.

[71] C.C. Fulton, G. Lucovsky, and R.J. Nemanich. *Appl. Phys. Lett.*, 84:580, 2004.

[72] G. Lucovsky, J.G. Hong, C.C. Fulton, Y. Zou, R.J. Nemanich, and H. Ade. *J. Vac. Sci. Tech. B*, 22:2132, 2004.

[73] N. Ikarashi and K. Manabe. *J. of Appl. Phys.*, 94:480, 2003.

[74] J. Robertson. *J. Vac. Sci. Tech.*, 18:1785, 2000.

[75] A. Fonseca, L. Demkov and A. Knizhnik. *Physica Status Solidi B*, 239:48, 2003.

[76] C. Van de Walle and R. Martin. *Phys. Rev. B*, 39:1871, 1989.

[77] S. Sayan, N. Nguyen, J. Ehrstein, J. Chambers., M. Visokay, M. Quevedo-Lopez, L. Colombo, D. Yoder, I. Levin, D. Fischer, M. Paunescu, O. Celik, and E. Garfunkel. *Appl. Phys. Lett.*, 87:212905, 2005.

[78] R. Puthenkovilakam and J.P. Chang. *Appl. Phys. Lett.*, 84:1353, 2004.

[79] S. Miyazaki. *J. of Vac. Sci. and Tech. B*, 19:2212, 2001.

[80] C.C. Fulton, G. Lucovsky, and R.J. Nemanich. *J. Appl. Phys.*, 99:63708, 2006.

[81] E. Garfunkel, S. Sayan, R.A. Bartynski, X. Zhao, E.P. Gusev, D. Vanderbilt, M. Croft, and M. Banaszak-Holl. *Phys. Status Solidi B*, 241:2246, 2004.

[82] T. Yamaguchi, H. Satake, N. Fukushima, and A. Toriumi. *International Electron Device Meeting, Technical Digest*, page 19, 2000.

[83] Ching Mo. *Phys. Rev. B*, 57:15219, 1998.

[84] R. Ludeke, M. T. Cuberes, and E. Cartier. *Appl. Phys. Lett.*, 76:2886, 2000.

[85] R.H. French. *J. Am. Ceramic Soc.*, 73:477, 1990.

[86] R. Hoffman, W. Henle, and F. Netzer. *Phys. Rev. B*, 44:3133, 1991.

[87] S. Sayan, E. Garfunkel, and S. Suzer. *Applied Physics Letters*, 80:2135, 2002.

[88] J.W. Keister, J.E. Rowe, J.J. Kolodziej, H. Niimi, and T.E. Madey. *J. Vac. Sci. Technol. B*, 17:1831, 1999.

[89] J. Rashmi, J. Gurganos, Y. Kim, R. Choi, J. Lee, and V. Misra. *IEEE Electron Device Lett.*, 25:0741–3106, 2004.

[90] H. Zhong, H. Lazar, and V. Misra. *IEEE Electron Device Letters*, 23:354, 2002.

[91] H. Kim, P. McIntyre, C. Chui, K. Saraswat, and S. Stemmer. *J. of Appl. Physics*, 96:3467, 2004.

[92] S. Suzer, S. Sayan, M. Banaszak Holl, E. Garfunkel, Z. Hussain, and N. Hamdan. *J. Vac. Sci. Tech. A*, 21:106, 1997.

[93] F. Rochet, Ch. Poncey, G. Dufour, H. Roulet, C. Guillot, and F. Sirotti. *J. Non-Crystalline Solids*, 216:148, 1997.

[94] E. Paparazzo. *Vacuum*, 62:47, 2001.

[95] M.L. Barr. *J. Chem. Phys.*, 82:1801, 1978.

[96] X ray Data Booklet. *Table of electron binding energies*, http://xdb.lbl.gov.

[97] U. Diebold, H. Tau, N. Shinn, and T.E. Madey. *Phys. Rev. B*, 50:14474, 1994.

[98] L.V. Goncharova, M. Dalponte, T. Gustafsson, O. Celik, E. Garfunkel, P.S. Lysacht, and G. Besurker. *J. of Vac. Sci. and Tech.*, 25:261, 2007.

[99] V. Afanas'ev and A. Stesmans. *J. Appl. Phys.*, 102:081301, 2007.

[100] H. Yang, Y. Son, S. Baek, H. Hwang, H. Lim, and H.S. Jung. *Appl. Phys. Lett.*, 86:092107, 2005.

[101] H. Alshareef, H. Wen, H. Luan, K. Choi, H. Harris, Y. Senzaki, P. Majhi, B. Lee, B. Foran, and G. Lian. *Thin Solid Films*, 515:1294, 2006.

[102] M.A. Green, K. Emery, D.L. King, S. Igari, and W. Warta. *Prog. in Photovoltaics: Res. and Appl.*, 12:365, 2004.

[103] M. Gratzel. *Prog. in Photovoltaics: Res. and Appl.*, 8:171, 2000.

[104] M. Nazeeruddin, A. Kay, I. Rodicio, R. Humphry-Baker, E. Muller, P. Liska, N. Vlachopoulos, and M. Gratzel. *J. Am. Chem. Soc.*, 115:6382, 1993.

[105] J. Moser, D. Noukakis, U. Bach, Y. Tachibana, D. Klug, J. Durrant, R. Humphry-Baker, and M. Gratzel. *J. Phys. Chem. B*, 102:3649, 1998.

[106] J.H. Snook, J. Samuelson, Kumar, Y.G. Kim, and J.E. Whitten. *Organic Electronics*, 6:55, 2005.

[107] J.B. Asbury, E. Hao, Y. Wang, H.N. Ghosh, and T. Lian. *J. Phys. Chem. B*, 105:4545, 2001.

[108] S.Y. Huang, G. Schlichthorl, A.J. Nozik, M. Gratzel, and A.J. Frank. *J. of Phys. Chem. B*, 101:2576, 1997.

[109] M. Spath, P.M. Sommeling, J.A.M. van Roosmalen, H.J.P. Smit, N.P.G. van der Burg, D.R. Mahieu, N.J. Bakker, and J.M. Kroon. *Prog. in Photovoltaics: Res. and Appl.*, 11:207, 2003.

[110] K. Kalyanasundaram and M. Gratzel. *Coordination Chemistry Reviews*, 77:347, 1998.

[111] M. Quintana, T. Edvinsson, A. Hagfeldt, and G. Boschloo. *J. Phys. Chem. C*, 111:1035, 2007.

[112] E. Galoppini, J. Rochford, H. Chen, G. Saraf, Y. Lu, A. Hagfeldt, and G. Boschloo. *J. Phys. Chem. B Letters*, 110:16159, 2006.

[113] B.A. Gregg. *Coordination Chemistry Reviews*, 248:1215, 2004.

[114] B.A. Gregg, F. Pichot, S. Ferrere, and C.L. Fields. *J. of Phys. Chem. B*, 105:1422, 2001.

[115] I.G. Hill and A. Kahn. *J. Appl. Phys.*, 84:5583, 1998.

[116] D. Zahn, G. Gavrila, and M. Gorgoi. *Chemical Physics*, 325:99, 2006.

[117] S. Padkhe, J. Sorge, S. Hachtmann, and D. Birnie. *Thin Solid Films*, to be submitted.

[118] C. Gorla, N. Emanetoglu, S. Liang, W. Mayo, Y. Lu, M. Wraback, and H. Shen. *J. Appl. Phys.*, 85:2595, 1999.

[119] C. Wagner, L. Davis, and Riggs. *Surface and Interface Analysis*, 2:53, 1980.

Vita

Eric Bersch

Education

2000–2008	Rutgers University, New Brunswick, NJ Ph.D. in Physics
1994–1995	Rutgers University, New Brunswick, NJ M.S. in Science Teaching
1995–1999	Franklin and Marshall College, Lancaster, PA B.A. in Physics

Positions Held

2003–2008	Research Assistant in Physics Department of Physics & Astronomy - Rutgers University
2000–2003	Teaching Assistant Department of Physics & Astronomy - Rutgers University
1995–2000	Teacher of Physics Pompton Lakes High School - Pompton Lakes, NJ

Publications

1. S. Rangan, **E. Bersch**, E. Garfunkel, R.A. Bartynski, "GeO_x Interface Layer Reduction upon Al Gate Deposition on $HfO_2/GeO_x/Ge$", *Applied Physics Letters*, (2008) **92**, p 172906-8

2. **E. Bersch**, S. Rangan, E. Garfunkel, R.A. Bartynski , "Band Offsets of High-κ Oxide Films with Si", *accepted by Physical Review B*

3. S. Rangan, **E. Bersch**, J.P. Theisen, R.A. Bartynski, "Energy level Alignment of N3/TiO_2(110) and N3/ZnO(11$\bar{2}$0)", *to be submitted*

4. S. Rangan, **E. Bersch**, E. Garfunkel, R.A. Bartynski, "Band Offsets between Ru Gates and High-κ Oxide Films on Si", *in preparation*

5. S. Rangan, **E. Bersch**, E. Garfunkel, R.A. Bartynski, "Band Offsets between Al and Ti Gates and High-κ Oxide Films on Si", *in preparation*

6. **E. Bersch**, S. Rangan, K. Katsiev, M. Batzill, B. Delley, U. Diebold, R.A. Bartynski, "Occupied and Unoccupied Electronic Structure of SnO_2(101)", *in preparation*

7. **E. Bersch**, S.Rangan, S. Dhar, L. Feldman, R.A. Bartynski, "Band Offsets of SiO_2/4H-SiC with Nitrided and Un-nitrided Interfaces", *in preparation*